New Electroanalytical Tools for Exocytosis: From Single Cells Toward Single Vesicles

Samuel T. Barlow

A dissertation

submitted in partial fulfillment of the

requirements for the degree of

Doctor of Philosophy

University of Washington

2021

Reading Committee:

Bo Zhang, Chair

Dan Fu

Ashleigh Theberge

Program Authorized to Offer Degree:

Chemistry

University of Washington

Abstract

New Electroanalytical Tools for Exocytosis: From Single Cells Toward Single Vesicles

Samuel T. Barlow

Chair of the Supervisory Committee:

Professor Bo Zhang

Department of Chemistry

This dissertation focuses on the development and application of new electroanalytical tools for the measurement of neurotransmitter release (e.g. dopamine, norepinephrine, epinephrine) from vesicles. Advancements in biosensor design for more sensitive, higher spatial resolution measurements of exocytosis at neuroendocrine cells and stem-cell derived neurons are detailed. New techniques for the characterization of redox-filled liposomes (here used as an analog for biologically-derived vesicles) are described and new insights into their electrochemical detection discussed. The application of these techniques to the measurement of catecholamine-containing large dense-core vesicles are also presented.

Chapter 1 introduces the relevant background for understanding the present state-of-the-art in exocytosis measurements, focusing on the information obtained from amperometric measurements. Chapter 2 details the development of carbon nanoprobes and their application to

exocytosis from single rat pheochromocytoma (PC12) cells and stem-cell derived human dopaminergic neurons. Chapter 3 discusses the development of a facile gold electrodeposition method for improving the sensitivity of carbon-fiber microelectrodes to catecholamine exocytosis.

Beginning in Chapter 4, we transition toward liposome/vesicle studies. Chapter 4 presents the initial validation of our new nanopore/microelectrode technique for simultaneous measurement of relative size and redox contents of single, redox-filled liposomes. Due to challenges in quantitation with the technique presented in Chapter 4, Chapter 5 details the use of a simpler technique, collision amperometry, to understand how these liposomes accumulate and release molecules.

Table of Contents

List of Tables

List of Schemes

List of Figures

Acknowledgements

I would first like to thank my advisor, Professor Bo Zhang. Though I didn't always recognize it, you are the epitome of the word "advisor." You patiently nudged me in the direction you felt I ought to go and encouraged me to pursue my curiosity. I would also like to thank you for the lessons you taught me through your actions. From you, I learned it is possible to be an excellent scientist without forsaking the things that make life worthwhile – so long as you are willing to answer your emails at 2:00 a.m.

I would also like to thank my committee members, Professor Dan Fu, Professor Ashleigh Theberge, and Professor Paul Phillips. I hope that you appreciate my growth as a scientist. I also acknowledge my former committee member, Professor A.J. Boydston. The care with which you chose your words was inspiring. I am grateful to the department for supporting me throughout my graduate career – I was and am still humbled to have been given the Achievement Rewards for College Scientists (ARCS) Fellowship through the UW Graduate School. Without that initial financial support, I would have never been able to attend graduate school here.

I wish to acknowledge Professor Daniel Chiu, who was my first mentor at UW. At that time, I lacked expertise and discipline, but I have never forgotten your first lessons for me. I have drawn great inspiration from your science.

To my lab-mates: your support, collegiality, and deep appreciation for the fundamentals have been a well of inspiration. To Chris Gunderson, I am deeply grateful for your mentorship and willingness to lend an ear. Your early support helped tune my trajectory. To Rui Hao, thank you for many small gifts of encouragement. To Yunshan Fan, thank you for showing me the meaning of discipline. To Matthew Louie, thank you for your great effort in electrode fabrication;

it helped get that first paper published. To Todd Anderson, thank you for being good company through it all. And many thanks for supporting every new experiment with your micro- and nanofabrication expertise. To Milomir Suvira, thank you for pushing me to be more than content with my work. To Peter Defnet, thank you for participating in many thought experiments that helped push my research to the next step. Your enthusiasm for your work has always motivated me. To Chris McCallister and Ruixuan Wan, thank you for being motivating forces. I deeply enjoyed the opportunity to learn from both of you. To Hongfang Gao, thank you for being one-of-a-kind. Your impact on our lab cannot be measured.

A big thank you to the many colleagues who helped me with vesicle isolations. To Professor Yongsoo Park, thank you so much for your many emails – your support was critical in troubleshooting the vesicle isolation protocol. My colleagues at Fred Hutch, Lindsay Klouser, Sijie Sun, and Daniel Stone, thank you for help with ultracentrifugation. Thank you to Schenk Packing Co., specifically John Lenz, for their generosity in providing bovine kidneys. Thank you to the butchers at Del Fox Custom Meats for your expertise in securing bovine adrenal glands. Thank you to Zack Potter of the Maly Lab for support with protease inhibitors.

To my UW friends and colleagues, thank you for your support. It really does take a village. To Caitlin Cornell, I cannot emphasize enough how conversations with you dramatically altered the trajectory of my research. It would have taken me many months to achieve an understanding of membrane biophysics that you were able to teach me in a few hours. To Benjamin Figueroa, thank you for supporting my research with Raman measurements; además, gracias por ser mi hermanito. To Andrew Francis, thank you for showing me what passion looks like. I aspire to be as accomplished as you. To Isaiah Bolden, thank you for reminding me to count my blessings. To Emily Rabe, thank you for showing me what excellence looks like. The effortless grace that

characterized your work in the community and the lab was a sight to behold. To Harrison Goldwyn, thank you for thoughtful conversation. You gave me the vocabulary to survive graduate school. To Jake Precht, thank you for the music, the support, and the paddleboarding trips. To Dylan Karis, thank you for your friendship. I will miss rock climbing with you. To Jake Busche, thank you for being a loyal friend. To Alex Santiago, thank you for being my first friend at UW. Our coffee tradition sustained me through challenging times.

To my many friends in Chicago, thank you for reminding me that the world is not graduate school. You grounded me through many challenges. Especially to Jason Ong and Dan Ziemniak, thank you for being a weekly source of joy.

To my family, thank you for your unending love and support. To my dad, Todd, thank you for being a listening ear on long car rides back home. The care you took in listening to me talk about my work was good practice, and critical therapy. To my mom, Sandi, thank you for always being there when I needed. You patiently listened when I wanted to quit graduate school, and celebrated every milestone when I chose to stay. To my big sister, Grace, thank you for your belief in my ability and your conviction that I could achieve more. Your Christmas gift to me in the second year has given me a daily reminder that I am capable of great things. To my big brother, David, thank you for being my constant mentor and friend. You reminded me that progress is not linear at all the right times. To my Grandma Helen, thank you for being a calming presence in times of strife, and helping me practice explaining my work.

To my loving fiancé Catherine Kauffmann: without your support, none of this would have been possible. When I asked you to move with me to Seattle 5 years ago, I could not have imagined a better way for things to turn out. First, I thank you for motivating my transformation to a professional – how could I stay at work when you are at home? Second, I thank you for giving

me grace – I would not be the person I am today but for your kindness. Last, thank you for making me whole. I derive great satisfaction from my work, but my love for you is my true passion.

To close, I wish to acknowledge my late grandparents, to whom this work is dedicated. To my Grandpa Jim, I miss your laughter every holiday. I wish you could have seen this. To my Grandma Maggie, I would have liked to open a scotch with you to celebrate this accomplishment. Someday we will be able to reverse or abolish the cognitive decline that drained you of your vigor.

Chapter 1. INTRODUCTION

1.1 AMPEROMETRY FOR ANALYZING SINGLE-CELL EXOCYTOSIS

Amperometry is an electroanalytical method which provides a quantitative means to directly measure exocytosis of electroactive messenger molecules (e.g. dopamine, serotonin) from neurons and secretory cells.[1,2] Following seminal work from the Wightman group demonstrating amperometric detection of catecholamine exocytosis from adrenal chromaffin cells,[3,4] many laboratories have used amperometry to measure exocytosis of large dense-core vesicles (LDCVs) and synaptic vesicles (SVs) containing different chemical messengers, including catecholamines (pheochromocytoma (PC12) cells,[5,6] midbrain dopaminergic neurons,[7,8] sympathetic ganglion neurons,[9] dopaminergic retinal neurons,[10,11] snail neurons,[12] MN9D cells[13]), serotonin (mast cells,[14] leech neurons,[15,16] blood platelets[17]), and peptides (pancreatic ß-cells,[18] pituitary melanotrophs[19]). These measurements have provided valuable information about secretion and the vesicle fusion machinery through amperometry's exquisite sensitivity (a few thousand molecules) and fast temporal resolution (10 μs).

In single-cell amperometry (SCA) a carbon-fiber microelectrode (CFE) poised at a potential sufficient for oxidation of the analyte-of-interest (+700 mV vs. Ag/AgCl for catecholamines) is placed on or near the surface of a secretory cell (**Figure 1.1**). When the cell is stimulated to exocytose (via electrical stimulation[11] or more commonly, chemical stimulation *via* high K^+ concentration,[4,5] Ba^{2+},[20,21] caffeine,[22] or α-latrotoxin[7]) many amperometric "spikes" are observed – upward deflections of current corresponding to the oxidation of quanta of catecholamines released from individual vesicles (**Figure 1.2A**). By carefully analyzing these amperometric spikes, researchers have explored key features of neurotransmitter release like diffusion kinetics, membrane fusion physics, and vesicle physiology.

1.1.1 DISSECTING AMPEROMETRIC SIGNALS

Figure 1.2B shows a typical amperometric signal collected during the exocytosis of LDCVs from a single PC12 cell. As amperometric signals reflect the flux of neurotransmitters (here, catecholamines) to the surface of the CFE, significant information regarding the vesicle fusion event itself can be extracted by analyzing amperometric signal attributes. As this dissertation mostly concerns insights gained from analyzing amperometric signals, here we provide a brief review of how amperometric signal analysis has contributed to the understanding of exocytosis, with special attention paid to LDCV exocytosis from neuroendocrine cells.

1.1.1.1 DIFFUSION KINETICS

The kinetic parameters, I_{max} (maximum current), $t_{1/2}$ (signal duration, full-width at half-maximum), t_{rise} (rise time, 25-75% amplitude), and t_{fall} (fall time, 75-25% amplitude) reflect the diffusion kinetics and duration of catecholamine release during vesicle fusion (**Figure 1.2B**). Amperometry has thus played a key role in understanding how the protein "dense-core"(so named because of how it appears in transmission electron micrograph (TEM) images, an electron-dense spot inside vesicles)[23] composed mostly of acidic soluble glycoproteins called chromogranins[24] modulates neurotransmitter release.

During vesicle fusion, the acidic interior of the vesicle (~pH 5.5)[25,26] is exposed to the extracellular bath (~pH 7.4). As H^+ diffuses down its concentration gradient into the bulk, electroneutrality dictates that H^+ will be replaced by hydrated cations from the bulk. Indeed, early amperometry studies of electroporated, isolated LDCVs from beige mouse mast cells showed this ion exchange plays a critical role in regulating neurotransmitter release, as the estimated diffusion coefficient of serotonin *decreased* as a function of cation valence in the buffer solution (i.e. serotonin diffused out of secretory granules more slowly in $LaCl_3$ vs. NaCl solution).[27,28] The Lindau group later confirmed that ion exchange occurs almost exclusively *via* the "fusion pore" (a nanoscale fluid junction that connects the vesicle lumen to the extracellular bath during exocytosis) rather than *via* transporter channels between the LDCV lumen and the cytosol.[29] Interestingly,

ion exchange initiated by proton diffusion is critical for maintaining the kinetics of catecholamine release, as LDCVs alkalinized by bafilomycin released far fewer catecholamines, more slowly.[30]

There is also a role for osmotic pressure in regulating catecholamine release from LDCV granules. In amperometric recordings of Ba^{2+}-stimulated release of LDCVs from adrenal chromaffin cells bathed in hypertonic saline, the Wightman group observed a "kiss-and-hold" release phenotype;[31] only "free catecholamines" unassociated with the dense core matrix were able to reach the electrode; vesicles fused, but osmotic pressure prevented dense-core matrix swelling and full release of catecholamines.

Now, a complete picture of the dense-core matrix behavior is becoming clear, in part due to recent modeling by Oleinick et al.[32] The dense-core matrix functions as a condensed polyelectrolyte (like a hydrogel). When an LDCV undergoes exocytosis, a nanometric fusion pore junction forms between the LDCV lumen and the extracellular bath. Protons rapidly exit the vesicle (initially pH 5.5), diffusing towards a lower concentration in the bulk (pH 7.4), but due to electroneutrality they must be replaced by hydrated cations from the bulk. The larger-sized hydrated cations cause the polyelectrolyte matrix to swell, creating a feedback loop that liberates catecholamines from their low affinity binding sites on the chromogranin backbone. Expansion is simultaneously favored by the osmotic gradient between the dense core and the extracellular bath (1500 mOsm vs. 300 mOsm),[33] which can explain why dense-core swelling was inhibited in the Wightman group experiments.[31] The hydrogel-like action of the matrix is also bounded by the membrane tension on the vesicle, which is in turn regulated by the size of the fusion pore. Interestingly, this model is fully consistent with a recent report from the Zhou group, which showed that dynamin 1 controlled whether exocytosis proceeded through a subquantal or quantal (i.e. partial vs. total release of catecholamines) release pathway; wild-type chromaffin cells featured fusion pores ≤ 9 nm, while dynamin-1 knockouts featured fusion pores ≥ 9 nm and released 250% more catecholamine per fusion event than wild-type.[34]

1.1.1.2 FUSION PORE DYNAMICS

The kinetic parameters of amperometric signals, as well as a feature called the "pre-spike foot" (PSF), contain information about the behavior of the fusion pore during exocytosis.[35,36] For example, in amperometric recordings of dopaminergic neurons from the rat midbrain, Staal and coworkers observed so-called "flickering fusion," in which single amperometric events exhibited multiple rising and falling phases (2-5 "flickers"). The authors hypothesized that flickering fusion corresponded to a new fusion mode in which the fusion pore dynamically contracted and dilated. Interestingly, flickering fusion events released twice as many dopamine molecules as fusion events with a single rising and falling phase (20,000 vs. 10,000 molecules) and was regulated by protein kinase C activity.[37]

The presence of a PSF indicates the presence of a short-lived, low-conductance fusion pore which limits diffusion of catecholamines to a steady-state. Vesicle volume has an inverse relationship with PSF frequency; reserpine-treated cells (smaller volume due to vesicular monoamine transporter (VMAT) inhibition) exhibited an increased PSF frequency, while L-3,4-dihydroxyphenylalanine (L-DOPA) treatment increased vesicle size and reduced PSF frequency.[38] Later work expanded on this, showing that high osmolarity saline increased PSF frequency as well.[39] Taken together, it appears that the vesicle membrane tension regulates the appearance of PSFs – low membrane tension (through osmolarity or small volume) increases the stability of the nascent fusion pore (increased PSF frequency), while high membrane tension favors rapid fusion pore dilation (reduced PSF frequency).

Proteins also play a role in regulating PSFs. For example, actin plays a critical role in regulating both transport and exocytosis of LDCVs in chromaffin cells, as the actin cytoskeletal network is remodeled during stimulated exocytosis.[40] Inhibition of actin remodeling through cytochalasin D or latrunculin A resulted in amperometric events with longer durations ($t_{1/2}$) and longer-lived PSFs in chromaffin cells, suggesting that actin supports exocytosis mechanically by accelerating fusion pore expansion and expulsion of catecholamines.[41] Other important work by the Jackson group showed that fusion pore behavior is strongly controlled by synaptotagmin, a calcium sensor that participates in triggering vesicle fusion as part

of the SNARE complex.[42] Interestingly, overexpression of synaptotagmin IV (Syt IV) increased the prevalence of PSFs, while overexpression of synaptotagmin I (Syt I) reduced PSF prevalence. Mutation of the Ca^{2+} sensing domains of each of these proteins abolished Syt control of fusion fate.[43]

1.1.1.3 QUANTAL SIZE

The integrated area under an amperometric signal corresponds to the total charge passed (Q) due to catecholamine oxidation (**Figure 1.2B**), which can be related directly to the number of molecules oxidized (i.e. the number of catecholamines released during exocytosis) through Faraday's equation:

$$Q = nFN$$

Where n is the stoichiometric number of electrons per charge transfer event (2 e^- for catecholamines), F is the Faraday constant (96,485 C mol^{-1}), and N is the number of moles of analyte oxidized (hundreds of zeptomole for PC12 exocytosis).

Quantal size of catecholamine LDCVs and SVs can be modified through pharmacological manipulation. Reserpine is a drug which inhibits the vesicular monoamine transporter (VMAT) by competing with catecholamines for binding sites. Treatment of PC12 cells with 100 nM reserpine resulted in reduced catecholamine release (~75% of control) and reduced vesicle volume.[44] Conversely, treatment with 100 µM L-DOPA, a precursor to dopamine in biosynthesis, resulted in 250% increased quantal size and increased vesicle volume.[45]

Quantal size is also regulated by endogenous mechanisms.[46] For example, Elhamdani et al. demonstrated that the average quantal size observed during exocytosis of LDCVs from adrenal chromaffin cells gradually increased with increased extracellular Ca^{2+} concentration[47] (implying that the magnitude of Ca^{2+} nano- and microdomains near Ca^{2+} channels[48-50] play a role in augmenting vesicle fusion and subsequently, the number of released molecules). The observation of a gradual shift in the distribution of quantal size rather than emergence of a bimodal distribution suggested that quantal size was subject to dynamic control, possibly due to Ca^{2+}-mediated fusion pore expansion.[51] Dynamin 1 activity also plays a

key role in regulating quantal size through inhibition of fusion pore expansion, possibly by controlling dense-core matrix expansion. [32,34,52]

In 2010, the Ewing group used a microfluidic separation and lysis strategy[53] to detect the neurotransmitter contents of isolated vesicles.[54] These initial experiments suggested that during stimulated exocytosis, LDCVs from PC12 cells only released ~40% of their total catecholamine payload. Later experiments from the same group applied the technique to dopaminergic synaptic vesicles from the mouse brain – the average synaptic vesicle contained 33,000 dopamine molecules.[55] Critically, these measurements opened the door for quantitative analysis of single vesicles *via* amperometry, which will be discussed in *Section 1.2*.

1.2 SINGLE-VESICLE ELECTROANALYSIS

There has recently been a flurry of activity in the exocytosis community, as amperometry is now being applied directly to isolated vesicles. The Ewing group expanded on their previous results, reporting vesicle impact electrochemical cytometry (VIEC) in 2015. By inserting a CFE into a suspension of isolated LDCVs and applying +0.7 V vs. Ag/AgCl, they observed that the contents of single vesicles can be detected quantitatively *via* collision, rupture, and electrolysis of their contents at the CFE.[56] Shortly thereafter, VIEC was applied directly to cells, using a sharp, flame-etched CFE (100 nm tip diameter) to pierce the cell membrane and measure vesicles intracellularly.[57,58] By comparing SCA and intracellular VIEC (IVIEC) measurements of the same cell, the authors directly observed that LDCVs from PC12 cells release only ~60% of their total contents during stimulated exocytosis, further confirming the existence of so-called "partial exocytosis."[59] Since then, SCA/IVIEC comparisons have been used to understand the effects of zinc,[60] lidocaine,[61] psychostimulants,[62] and repetitive stimulation[63] on both neurotransmitter release and total vesicle contents. The technique has also been combined with nanoscale imaging methods to understand neurotransmitter storage in LDCVs.[64]

1.2.1 MECHANISMS FOR SINGLE VESICLE AND SINGLE LIPOSOME DETECTION

Despite significant progress, the understanding of vesicle detection *via* VIEC remains imprecise (**Figure 1.3**). It is known that the vesicle membrane must rupture to permit detection of vesicle contents, as the lipid bilayer membrane that segregates the vesicle contents from the extravesicular solution is too thick (~5 nm) to permit electron tunneling unless other electroactive dopants or defects are added.[65-68] Clearly, the applied voltage on the electrode surface plays a critical role in promoting vesicle rupture, as rupture event frequency and release kinetics increased with applied potential.[69] The Ewing group also showed that vesicle rupture is more favorable at elevated temperature[70] or when excited-state fluorophores are embedded in the vesicle membrane.[71] In addition, the stochastic movement of vesicle surface proteins appears to play a role in vesicle detection, as LDCVs from adrenal chromaffin cells had lower rupture frequencies than protein-free liposomes.[69]

Complementing these single vesicle studies, researchers have also explored detection of single liposomes. Liposomes are lab-synthesized analogs for biological vesicles and cells, possessing only a lipid bilayer which segregates the internal from the external solution. Their simplicity makes them useful for the study of membrane dynamics.[72,73] In addition, liposomes are useful as biocompatible drug vehicles,[74] making it desirable to develop single liposome quantification methods.

Liposomes are apparently permeabilized *via* different mechanisms, depending on solution context and/or electrode material. In 2014, Cheng and Compton published a quantitative study of commercially available, ascorbic acid-loaded liposomes; they detected liposomes through their collision and rupture at a carbon-fiber microelectrode, permitting direct quantification of the liposomal ascorbic acid concentration. However, their hypothesized "full-collapse fusion" mechanism in which liposomes collide, spread, and rupture was controversial.[75] Later work by the Bard group implied that ferrocyanide-loaded liposomes could only be detected at Pt microelectrodes in the presence of some membrane destabilizing agent, like the surfactant Triton-X-100 (TX-100);[76] interestingly, the critical [TX-100] for liposome detection agreed well with a previous study on cell permeabilization in the presence of TX-100,[77] suggesting that TX-100

enhances liposome electrochemical detection by permeating liposomes or making them more liable to permeate upon collision with an electrode. More recently, the Bard group showed that increasing temperature or the addition of other redox mediators in solution can enhance liposome permeability during collision.[78] Crucially, some have reported disagreement between the expected vs. measured electrochemical signals from single liposomes, indicating a poor understanding of how liposomes are loaded with molecules and/or release them.[69,79]

1.3 DISSERTATION OUTLINE

In the intervening three decades since Wightman published the first single-cell amperometry measurements, hundreds of papers have been published on amperometric monitoring of exocytosis. Most of these papers have focused on LDCV exocytosis from neuroendocrine cells (vesicles loaded with 10^4-10^7 molecules, depending on the cell preparation). Though these studies have been immensely valuable in understanding the conserved exocytosis machinery and vesicle fusion, they cannot fill critical knowledge gaps in synaptic vesicle-based communication in the brain.

In this dissertation, I aimed to bridge the gap between existing techniques for measuring LDCV exocytosis and new tools for measuring synaptic vesicle exocytosis. To address the various challenges associated with measuring synaptic vesicle exocytosis *in vitro*, I developed a protocol for fabricating nanometric carbon electrodes which were size-tunable from 50 nm to 1 µm in diameter (Chapter 2). We successfully demonstrated that these carbon nanoprobes (CNPs) can differentiate between single release sites on the surface of a PC12 cell. We then established a novel model for synaptic vesicle exocytosis, precursor cell-derived human dopaminergic neuronal cells (HDNCs), to assess the performance of CNPs for addressing single presynaptic release sites. We found the measurements were incredibly challenging due to the challenges of diffusional broadening,[80] in which signal-to-noise ratio (SNR) decreases significantly as the distance between the release site and sensor increases.

While carbon is a useful electrode material for biological recordings (due to its resistance to biofouling), noble metal electrode materials like gold and platinum have better electron transfer kinetics. We reasoned that a facile electrode modification procedure, in which noble metals could be deposited on existing electrode scaffolds, may partly ameliorate the SNR challenges we encountered during synaptic vesicle exocytosis recordings by enhancing electron-transfer kinetics (**Chapter 2**). So, we developed a 1-step procedure for electrodepositing gold nanoparticles on the surface of carbon-fiber microelectrodes (CFEs). Gold nanoparticle modification dramatically increased electrochemical surface area and electron transfer kinetics for dopamine oxidation. Surprisingly, we found that these Au-CFEs detected significantly more catecholamine per exocytotic event than conventional CFEs (**Chapter 3**).

In the latter half of this dissertation, we turned our attention to single vesicle analysis. Electrochemical methods for single vesicle analysis are likely critical for a quantitative understanding of synaptic vesicle physiology in healthy and diseased states. However, present methods lack throughput (in VIEC, vesicle rupture varies on the timescale of seconds to minutes) and lack mechanistic detail. We were keenly interested in developing a method in which the size and contents of single vesicles could be addressed simultaneously, permitting direct concentration measurements. To achieve this, we sized redox-loaded liposomes using a nanopore and detected their redox contents using an ultramicroelectrode (**Chapter 4**). To our surprise, however, we could only achieve simultaneous signal recordings by driving liposomes out of the nanopore at high pressure. Further investigation revealed that liposomes ruptured *during* passage through the nanopore, likely due to high shear-stress mediated by fast fluid flow and nanopore geometry. Our method permitted simultaneous size and content measurements of thousands of vesicles in minutes.

In the work presented in **Chapter 4**, we observed that liposomes were only loaded with only ~50 mM $K_4Fe(CN)_6$, when we attempted to load with 700 mM $K_4Fe(CN)_6$ during synthesis (consistent with other works).[69,79] To address both the lack of mechanistic insight into VIEC / liposome detection during collision amperometry and understanding of how liposomes are loaded with molecules, we performed a study of liposome loading and release in response to different osmotic pressures (**Chapter 5**). Critically,

we observed that the internal concentration of redox molecules is strongly regulated by osmotic pressure (observed with amperometry and Raman spectroscopy), consistent with a recent study of osmotic pressure using giant unilamellar vesicles (GUVs).[81]

1.4 FIGURES

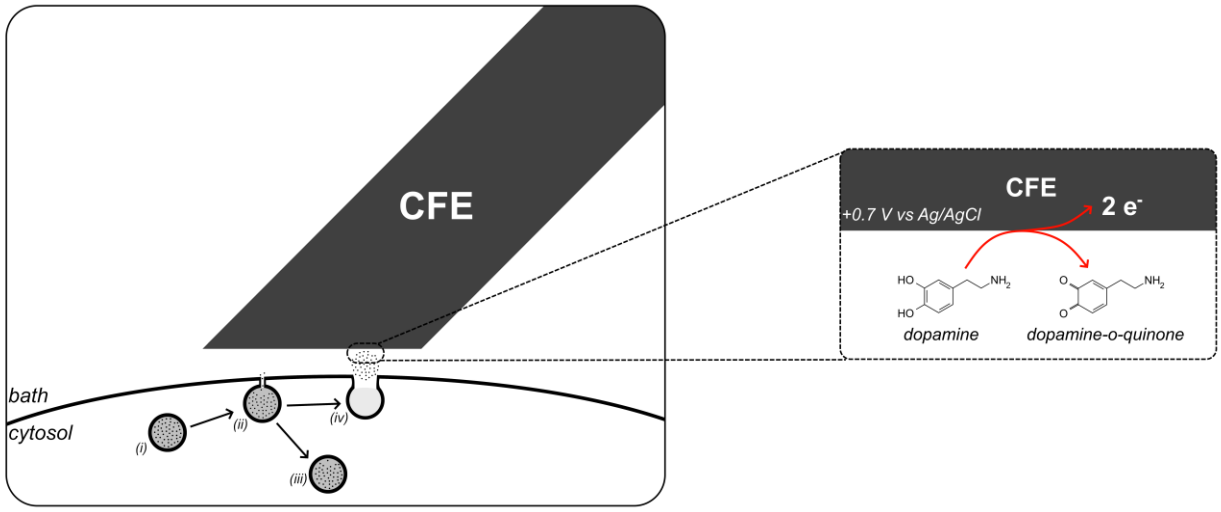

Figure 1.1. Single-Cell Amperometry. A simplified view of exocytosis recordings using single-cell amperometry. A 5 µm carbon-fiber microelectrode (CFE) approaches a cell surface (not drawn to scale). *(i)* Initially, a large dense-core vesicle (LDCV, *dense-core matrix pictured in grey*) containing catecholamines (here, dopamine, *black dots*) is primed for exocytosis in the cell cytosol. *(ii)* Upon cell stimulation, Ca^{2+}-triggered exocytosis occurs. The LDCV fuses with the outer cell membrane; however, the "fusion pore" connecting the LDCV lumen to the extracellular bath is initially in a low conductance state, limiting diffusion of dopamine to the electrode surface. From here, *(iii)* the LDCV may be recycled directly, preventing further diffusion of catecholamine (i.e. kiss-and-run exocytosis); or *(iv)* the LDCV will undergo full fusion, collapsing into the cell membrane and releasing its entire dopamine payload. The LDCV will later be recycled by clathrin-mediated endocytosis (not pictured here). *Inset:* zoomed-in view of amperometric detection. Dopamine molecules encounter the CFE surface (poised at +0.7 V vs Ag/AgCl) and are oxidized to dopamine-o-quinone, surrendering two electrons to the electrochemical circuit. Oxidation of many such dopamine molecules results in a measurable oxidation current (see **Figure 1.2**).

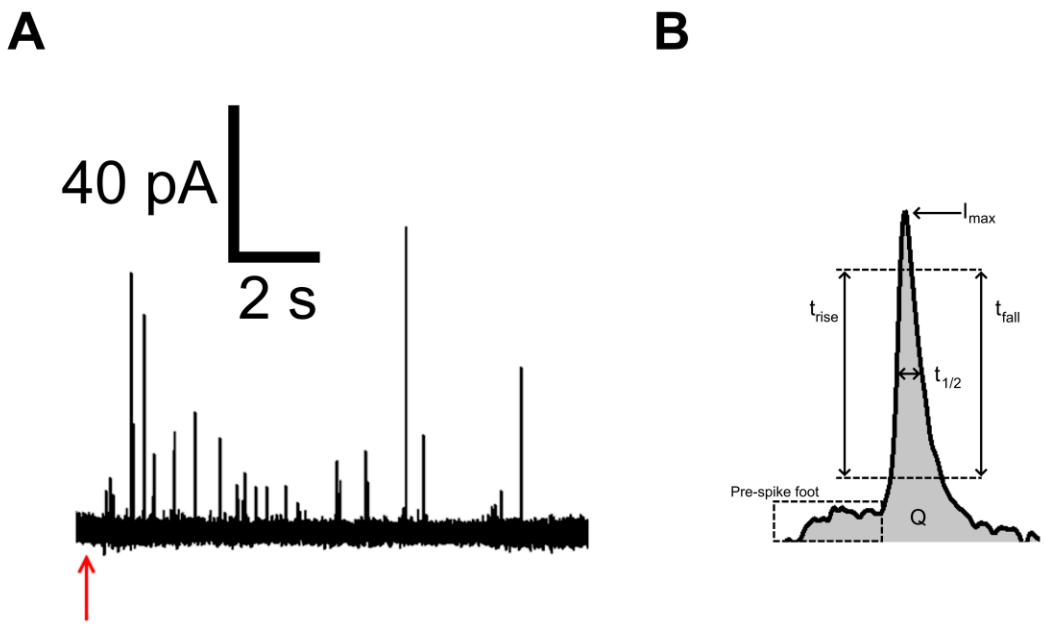

Figure 1.2. Analyzing Amperometric Signals. *A)* An example amperometric trace collected during stimulated exocytosis of LDCVs from a single rat pheochromocytoma (PC12) cell. The PC12 cell was stimulated to exocytose using a 20 p.s.i., 5 s pulse of 100 mM K^+, indicated by the red arrow. Immediately following stimulation, many amperometric signals are observed, corresponding to the oxidation of catecholamines released from single vesicle fusion events. *B)* Analysis of a single amperometric signal. Many amperometric signals (~10-25%) have a "pre-spike foot," indicating a low-conductance fusion pore wherein catecholamine diffusion is limited by the fusion pore diameter. The maximum current, I_{max}, indicates the maximum flux of molecules to the electrode surface; I_{max} contains information about both diffusion kinetics and fusion pore diameter. The duration of the signal, $t_{1/2}$, is the full-width at half-maximum amplitude. $t_{1/2}$ reflects the duration of neurotransmitter release. t_{rise} and t_{fall} are the duration from 25-75% and 75-25% maximum amplitude, respectively; they reflect the kinetics of fusion pore opening and closure/release, respectively. *Q* is the area under the amperometric signal, reflecting the total charge passed during the signal. *Q* is related to the total number of molecules oxidized through Faraday's equation, $Q = nFN$, where *n* is the stoichiometric number of electrons transferred (2 e^- for catecholamines), *F* is Faraday's constant (96485 C mol^{-1}) and *N* is the number of moles.

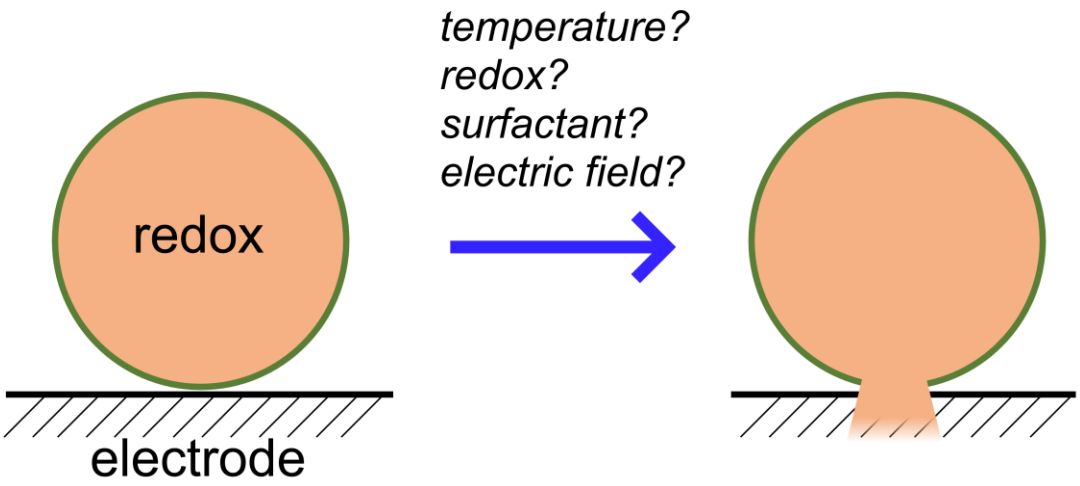

Figure 1.3. How are single vesicles/liposomes detected with amperometry? Vesicle/liposome contents cannot be quantified directly with amperometry unless the thin lipid bilayer (~5 nm) that separates the internal contents from the external solution opens. However, several methods have been proposed for liposome/vesicle permeabilization during collision amperometry (see Section 1.2.1), including electroporation,[69,70,79] excited-state fluorophores embedded in the lipid bilayer,[71] temperature,[70,78] redox mediators in solution,[78] or surfactant.[76,78]

1.5 REFERENCES

(1) Bucher, E. S. & Wightman, R. M. “Electrochemical Analysis of Neurotransmitters.” *Annu. Rev. Anal. Chem.*, **2015**, *8*, 239–261.

(2) Mosharov, E. V. & Sulzer, D. “Analysis of exocytotic events recorded by amperometry.” *Nature Methods*, **2008**, *2*, 651–658.

(3) Leszczyszyn, D. J.; Jankowski, J. A.; Viveross, H.; Diliberto, E. J.; Nears, J. A.; Wightman, R. M. “Nicotinic Receptor-Mediated Catecholamine Secretion from Individual Chromaffin Cells.” *J. Biol. Chem.*, **1990**, *265*, 14736–14737.

(4) Wightman, R. M.; Jankowski, J. A.; Kennedy, R. T.; Kawagoe, K. T.; Leszczyszyn, D. J.; Near, J. A.; Diliberto, E. J., Viveros, O. H. “Temporally resolved catecholamine spikes correspond to single vesicle release from individual chromaffin cells.” *Proc. Natl. Acad. Sci.*, **1991**, *88*, 10754–10758.

(5) Chen, T. K.; Luo, G.; Ewing, A. G. “Amperometric monitoring of stimulated catecholamine release from rat pheochromocytoma (PC12) cells at the zeptomole level.” *Anal. Chem.*, **1994**, *66*, 3031–3035.

(6) Zerby, S. E. & Ewing, A. G. “Electrochemical monitoring of individual exocytotic events from the varicosities of differentiated PC12 cells.” *Brain Res.*, **1996**, *712*, 1–10.

(7) Pothos, E. N.; Davila, V.; Sulzer, D. “Presynaptic Recording of Quanta from Midbrain Dopamine Neurons and Modulation of the Quantal Size.” *J. Neurosci.*, **1998**, *18*, 4106–4118.

(8) Jaffe, E. H.; Marty, A.; Schulte, A; Chow, R. H. “Extrasynaptic Vesicular Transmitter Release from the Somata of Substantia Nigra Neurons in Rat Midbrain Slices.” *J. Neurosci.*, **1998**, *18*, 3548–3553.

(9) Zhou, Z., & Misler, S. “Amperometric detection of stimulus-induced quantal release of catecholamines from cultured superior cervical ganglion neurons.” *Proc. Natl. Acad. Sci.*, **1995**, *92*, 6938–6942.

(10) Hochstetler, S. E.; Puopolo, M.; Gustincich, S.; Raviola, E.; Wightman, R. M. “Real-Time Amperometric Measurements of Zeptomole Quantities of Dopamine Released from Neurons.” *Anal. Chem.*, **2000**, *72*, 489–496.

(11) Puopolo, M.; Hochstetler, S. E.; Gustincich, S.; Wightman, R. M.; Raviola, E. “Extrasynaptic Release of Dopamine in a Retinal Neuron: Activity Dependence and Transmitter Modulation.” *Neuron*, **2001**, *30*, 211–225.

(12) Chen, G. & Ewing, A. G. “Multiple classes of catecholamine vesicles observed during exocytosis from the Planorbis cell body.” *Brain Res.*, **1995**, *701*, 167–174.

(13) Dong, Y.; Heien, M. L.; Maxson, M. M.; Ewing, A. G. “Amperometric measurements of catecholamine release from single vesicles in MN9D cells.” *J. Neurochem.*, **2008**, *107*, 1589–1595.

(14) Alverez de Toledo, G.; Fernandez-Chacon, R.; Fernandez, J. M. “Release of secretory products during transient vesicle fusion.” *Nature*, **1993**, *363*, 554–558.

(15) Bruns, D. & Jahn, R. “Real-time measurement of transmitter release from single synaptic vesicles.” *Nature*, **1995**, *377*, 185–187.

(16) Bruns, D.; Riedel, D.; Klingauf, J.; Jahn, R. “Quantal release of serotonin.” *Neuron*, **2000**, *28*, 205–220.

(17) Ge, S.; White, J. G.; Haynes, C. L. “Quantal Release of Serotonin from Platelets.” *Anal. Chem.*, **2009**, *81*, 2935–2943.

(18) Huang, L.; Shen, H.; Atkinson, M. A.; Kennedy, R. T. “Detection of exocytosis at individual pancreatic ß cells by amperometry at a chemically modified microelectrode.” *Proc. Natl. Acad. Sci.*, **1995**, *92*, 9608–9612.

(19) Paras, C. D., & Kennedy, R. T. “Electrochemical Detection of Exocytosis at Single Rat Melanotrophs.” *Anal. Chem.*, **1995**, *67*, 3633–3637.

(20) Borges, R.; Travis, E. R.; Hochstetler, S. E.; Wightman, R. M. “Effects of External Osmotic Pressure on Vesicular Secretion from Bovine Adrenal Medullary Cells.” *J. Biol. Chem.* **1997**, *272*, 8325–8331.

(21) Amatore, C.; Arbault, S.; Bouret, Y.; Guille, M.; Lemaitre, F.; Verchier, Y. “Invariance of Exocytotic Events Detected by Amperometry as a Function of the Carbon Fiber Microelectrode Diameter.” *Anal. Chem.*, **2009**, *81*, 3087–3093.

(22) Finnegan, J. M. & Wightman, R. M. “Correlation of Real-time Catecholamine Release and Cytosolic Ca2+ at Single Bovine Chromaffin Cells.” *J. Biol. Chem.*, **1995**, *270*, 5353–5359.

(23) Camilli, P. & Jahn, R. “Pathways to regulated exocytosis in neurons.” *Annu. Rev. Physiol.*, **1990**, *52*, 625–645.

(24) Domínguez, N.; Estévez-Herrera, J.; Pardo, M. R.; Pereda, D.; Machado, J. D.; Borges, R. “The functional role of chromogranins in exocytosis.” *J. Mol. Neurosci.*, **2012**, *48*, 317–322.

(25) Yoo, S. H. & Albanesi, J. P. “Ca2+-induced conformational change and aggregation of chromogranin A.” *J. Biol. Chem.*, **1990**, *265*, 14414–14421.

(26) Miesenbock, G.; De Angelis, D. A.; Rothman, J. E. “Visualizing secretion and synaptic transmission with pH-sensitive green fluorescent proteins.” *Nature*, **1998**, *394*, 192–195.

(27) Marszalek, P. E.; Farrell, B.; Verdugo, P.; Fernandez, J. M. “Kinetics of release of serotonin from isolated secretory granules I. Amperometric detection of serotonin from electroporated granules.” *Biophys. J.*, **1997**, *73*, 1160–1168.

(28) Marszalek, P. E.; Farrell, B.; Verdugo, P.; Fernandez, J. M. “Kinetics of release of serotonin from isolated secretory granules II. Ion exchange determines, the diffusivity of serotonin.” *Biophys. J.*, **1997**, *73*, 1169–1183.

(29) Gong, L. W.; de Toledo, G. A.; Lindau, M. “Exocytotic catecholamine release is not associated with cation flux through channels in the vesicle membrane but Na+ influx through the fusion pore.” *Nat. Cell Biol.*, **2007**, *9*, 915–922.

(30) Camacho, M.; Machado, J. D.; Montesinos, M. S.; Criado, M.; Borges, R. “Intragranular pH rapidly modulates exocytosis in adrenal chromaffin cells.” *J. Neurochem.*, **2006**, *96*, 324–334.

(31) Troyer, K. P. & Wightman, R. M. “Temporal separation of vesicle release from vesicle fusion during exocytosis.” *J. Biol. Chem.*, **2002**, *277*, 29101–29107.

(32) Oleinick, A.; Hu, R.; Ren, B.; Tian, Z.-Q.; Svir, I.; Amatore, C. “Theoretical Model of Neurotransmitter Release during In Vivo Vesicular Exocytosis Based on a Grainy Biphasic Nano-Structuration of Chromogranins within Dense Core Matrixes.” *J. Electrochem. Soc.*, **2016**, *163*, H3014–H3024.

(33) Wightman, R. M.; Domínguez, N.; Borges, R. “How intravesicular composition affects exocytosis.” *Pflug. Arch. Eur. J. Phys.*, **2018**, *470*, 135–141.

(34) Wu, Q.; Zhang, Q.; Liu, B.; Li, Y.; Wu, X.; Kuo, S.; Zheng, L.; Wang, C.; Zhu, F.; Zhou, Z. "Dynamin 1 restrains vesicular release to a subquantal mode in mammalian adrenal chromaffin cells." *J. Neurosci.*, **2019**, *39*, 199–211.

(35) Jackson, M. B. "In search of the fusion pore of exocytosis." *Biophys. Chem.*, **2007**, *126*, 201–208.

(36) Chang, C. W.; Chiang, C. W.; Jackson, M. B. "Fusion pores and their control of neurotransmitter and hormone release." *J. Gen. Physiol.*, **2017**, *149*, 301–322.

(37) Staal, R. G. W.; Mosharov, E. V.; Sulzer, D. "Dopamine neurons release transmitter via a flickering fusion pore." *Nat. Neurosci.*, **2004**, *7*, 341–346.

(38) Sombers, L. A.; Hanchar, H. J.; Colliver, T. L.; Wittenberg, N.; Cans, A.; Arbault, S.; Amatore, C.; Ewing, A. G. "The Effects of Vesicular Volume on Secretion through the Fusion Pore in Exocytotic Release from PC12 Cells." *J. Neurosci.*, **2004**, *24*, 303–309.

(39) Sombers, L. A.; Wittenberg, N. J.; Maxson, M. M.; Adams, K. L.; Ewing, A. G. "High osmolarity and L-DOPA augment release via the fusion pore in PC12 cells." *ChemPhysChem*, 2**007**, *8*, 2471–2477.

(40) Trifaro, J.-M.; Gasman, S.; Gutierrez, L. M. "Cytoskeletal control of vesicle transport and exocytosis in chromaffin cells." *Acta Physiol.*, **2008**, *192*, 165–172.

(41) Berberian, K.; Torres, A. J.; Fang, Q.; Kisler, K.; Lindau, M. "F-Actin and Myosin II Accelerate Catecholamine Release from Chromaffin Granules." *J. Neurosci.*, **2009**, *29*, 863–870.

(42) Wang, C.; Grishanin, R.; Earles, C. A.; Chang, P. Y.; Martin, T. F. J.; Chapman, E. R.; Jackson, M. B. “Synaptotagmin Modulation of Fusion Pore Kinetics in Regulated Exocytosis of Dense-Core Vesicles.” *Science*, **2001**, *294*, 1111–1116.

(43) Wang, C. T.; Lu, J. C.; Bai, J.; Chang, P. Y.; Martin, T. F. J.; Chapman, E. R.; Jackson, M. B. “Different domains of synaptotagmin control the choice between kiss-and-run and full fusion.” *Nature*, **2003**, *424*, 943–947.

(44) Colliver, T. L.; Pyott, S. J.; Achalabun, M.; Ewing, A. G. “VMAT-Mediated Changes in Quantal Size and Vesicular Volume.” *J. Neurosci.*, **2000**, *20*, 5276–5282.

(45) Pothos, E.; Desmond, M.; Sulzer, D. “L-3,4-Dihydroxyphenylalanine Increases the Quantal Size of Exocytotic Dopamine Release In Vitro.” *J. Neurochem.*, **1996**, *66*, 629-636.

(46) Sulzer, D. & Pothos, E. N. “Regulation of quantal size by presynaptic mechanisms.” *Rev. Neurosci.*, **2000**, *11*, 159–212.

(47) Elhamdani, A.; Palfrey, H. C.; Artalejo, C. R. “Quantal size is dependent on stimulation frequency and calcium entry in calf chromaffin cells.” *Neuron*, **2001**, *31*, 819–830.

(48) Neher, E. “Vesicle pools and Ca2+ microdomains: New tools for understanding their roles in neurotransmitter release.” *Neuron*, **1998**, *20*, 389–399.

(49) Becherer, U.; Moser, T.; Stühmer, W.; Oheim, M. “Calcium regulates exocytosis at the level of single vesicles.” *Nat. Neurosci.*, **2003**, *6*, 846–853.

(50) Graydon, C. W.; Cho, S.; Li, G. L.; Kachar, B.; von Gersdorff, H. “Sharp Ca 2+ Nanodomains beneath the ribbon promote highly synchronous multivesicular release at hair cell synapses.” *J. Neurosci.*, **2011**, *31*, 16637–16650.

(51) Scepek, S.; Coorssen, J. R.; Lindau, M. “Fusion pore expansion in horse eosinophils is modulated by Ca^{2+} and protein kinase C via distinct mechanisms.” *EMBO J*, **1998**, *17*, 4340–4345.

(52) Trouillon, R. & Ewing, A. G. “Amperometric measurements at cells support a role for dynamin in the dilation of the fusion pore during exocytosis.” *ChemPhysChem*, **2013**, *14*, 2295–2301.

(53) Omiatek, D. M.; Santillo, M. F.; Heien, M. L.; Ewing, A. G. “Hybrid capillary-microfluidic device for the separation, lysis, and electrochemical detection of vesicles.” *Anal. Chem.*, **2009**, *81*, 2294–2302.

(54) Omiatek, D. M.; Dong, Y.; Heien, M. L.; Ewing, A. G. “Only a fraction of quantal content is released during exocytosis as revealed by electrochemical cytometry of secretory vesicles.” *ACS Chem. Neurosci.*, **2010**, *1*, 234–245.

(55) Omiatek, D. M.; Bressler, A. J.; Cans, A. S.; Andrews, A. M.; Heien, M. L.; Ewing, A. G. “The real catecholamine content of secretory vesicles in the CNS revealed by electrochemical cytometry.” *Sci. Rep.*, **2013**, *3*:1447.

(56) Dunevall, J.; Fathali, H.; Najafinobar, N.; Lovric, J.; Wigström, J.; Cans, A. S.; Ewing, A. G. “Characterizing the Catecholamine Content of Single Mammalian Vesicles by Collision-Adsorption Events at an Electrode.” *J. Am. Chem. Soc.*, **2015**, *137*, 4344–4346.

(57) Li, X.; Majdi, S.; Dunevall, J.; Fathali, H.; Ewing, A. G. “Quantitative Measurements of Transmitters in Vesicles One at a Time in Single Cell Cytoplasm with Nano-tip Electrodes.” *Angew. Chem. Int. Ed.*, **2015**, *54*, 11978–11982.

(58) Li, X.; Ren, L.; Dunevall, J.; Ye, D.; White, H. S.; Edwards, M. A.; Ewing, A. G. “Nanopore Opening at Flat and Nanotip Conical Electrodes during Vesicle Impact Electrochemical Cytometry.” *ACS Nano*, **2018**, *12*, 3010–3019.

(59) Ren, L.; Mellander, L. J.; Keighron, J.; Cans, A.-S.; Kurczy, M. E.; Svir, I.; Oleinick, A.; Amatore, C.; Ewing, A. G. “The evidence for open and closed exocytosis as the primary release mechanism.” *Quart. Rev. Biophys.*, **2016**, *49*, e12.

(60) Ren, L.; Pour, M. D.; Majdi, S.; Li, X.; Malmberg, P.; Ewing, A. G. “Zinc Regulates Chemical-Transmitter Storage in Nanometer Vesicles and Exocytosis Dynamics as Measured by Amperometry.” *Angew. Chem. Int. Ed.*, **2017**, *56*, 4970–4975.

(61) Ye, D.; Gu, C.; Ewing, A. G. “Using Single-Cell Amperometry and Intracellular Vesicle Impact Electrochemical Cytometry to Shed Light on the Biphasic Effects of Lidocaine on Exocytosis.” *ACS Chem. Neurosci.*, **2018**, *9*, 2941–2947.

(62) Zhu, W.; Gu, C.; Dunevall, J.; Ren, L.; Zhou, X.; Ewing, A. G. “Combined Amperometry and Electrochemical Cytometry Reveal Differential Effects of Cocaine and Methylphenidate on Exocytosis and the Fraction of Chemical Release.” *Angew. Chem. Int. Ed.*, **2019**, *58*, 4238–4242.

(63) Gu, C.; Larsson, A.; Ewing, A. G. “Plasticity in exocytosis revealed through the effects of repetitive stimuli affect the content of nanometer vesicles and the fraction of transmitter released.” *Proc. Natl. Acad. Sci.*, **2019**, *116*, 21409–21415.

(64) Lovrić, J.; Dunevall, J.; Larsson, A.; Ren, L.; Andersson, S.; Meibom, A.; Malmberg, P.; Kurczy, M. E.; Ewing, A. G. “Nano Secondary Ion Mass Spectrometry Imaging of Dopamine Distribution Across Nanometer Vesicles.” *ACS Nano*, **2017**, *11*, 3446–3455.

(65) Plant, A. L.; Gueguetchkeri, M.; Yap, W. “Supported phospholipid/alkanethiol biomimetic membranes: insulating properties.” *Biophys. J.*, **1994**, *67*, 1126–1133.

(66) Wilburn, J. P.; Wright, D. W.; Cliffel, D. E. “Imaging of voltage-gated alamethicin pores in a reconstituted bilayer lipid membrane via scanning electrochemical microscopy.” *Analyst*, **2006**, *131*, 311–316.

(67) Campos, R. & Kataky, R. “Electron transport in supported and tethered lipid bilayers modified with bioelectroactive molecules.” *J. Phys. Chem. B*, **2012**, *116*, 3909–3917.

(68) Schmallegger, M.; Barbon, A.; Bortolus, M.; Chemelli, A.; Bilkis, I.; Gescheidt, G.; Weiner, L. “Systematic Quantification of Electron Transfer in a Bare Phospholipid Membrane Using Nitroxide-Labeled Stearic Acids: Distance Dependence, Kinetics, and Activation Parameters.” *Langmuir*, **2020**, *36*, 10429–10437.

(69) Lovrić, J.; Najafinobar, N.; Dunevall, J.; Majdi, S.; Svir, I.; Oleinick, A.; Amatore, C.; Ewing, A. G. “On the mechanism of electrochemical vesicle cytometry: chromaffin cell vesicles and liposomes.” *Faraday Discussions*, **2016**, *193*, 65–79.

(70) Li, X.; Dunevall, J.; Ren, L.; Ewing, A. G. “Mechanistic Aspects of Vesicle Opening during Analysis with Vesicle Impact Electrochemical Cytometry.” *Anal. Chem.*, **2017**, *89*, 9416–9423.

(71) Najafinobar, N.; Lovrić, J.; Majdi, S.; Dunevall, J.; Cans, A. S.; Ewing, A. G. “Excited Fluorophores Enhance the Opening of Vesicles at Electrode Surfaces in Vesicle Electrochemical Cytometry.” *Angew. Chem. Int. Ed.*, **2016**, *55*, 15081–15085.

(72) Sezgin, E.; Kaiser, H. J.; Baumgart, T.; Schwille, P.; Simons, K.; Levental, I. "Elucidating membrane structure and protein behavior using giant plasma membrane vesicles." *Nat. Prot.*, **2012**, *7*, 1042–1051.

(73) Witkowska, A. & Jahn, R. "Rapid SNARE-Mediated Fusion of Liposomes and Chromaffin Granules with Giant Unilamellar Vesicles." *Biophys. J.*, **2017**, *113*, 1251–1259.

(74) Torchilin, V. P. "Recent advances with liposomes as pharmaceutical carriers." *Nat. Rev. Drug Disc.*, **2005**, *4*, 145–160.

(75) Cheng, W. & Compton, R. G. "Investigation of single-drug-encapsulating liposomes using the nano-impact method." *Angew. Chem. Int. Ed.*, **2014**, *53*, 13928–13930.

(76) Lebègue, E.; Anderson, C. M.; Dick, J. E.; Webb, L. J.; Bard, A. J. "Electrochemical Detection of Single Phospholipid Vesicle Collisions at a Pt Ultramicroelectrode." *Langmuir*, **2015**, *31*, 11734–11739.

(77) Koley, D. & Bard, A. J. "Triton X-100 concentration effects on membrane permeability of a single HeLa cell by scanning electrochemical microscopy (SECM)." *Proc. Natl. Acad. Sci.*, **2010**, *107*, 16783–16787.

(78) Lebègue, E.; Barrière, F.; Bard, A. J. "Lipid Membrane Permeability of Synthetic Redox DMPC Liposomes Investigated by Single Electrochemical Collisions." *Anal. Chem.*, **2020**, *92*, 2401–2408.

(79) Pan, R.; Hu, K.; Jiang, D.; Samuni, U.; Mirkin, M. V. "Electrochemical Resistive-Pulse Sensing." *J. Am. Chem. Soc.*, **2020**, *141*, 19555–19559.

(80) Schroeder, T. J.; Jankowski, J. A.; Kawagoe, K. T.; Wightman, R. M.; Lefrou, C.; Amatore, C. “Analysis of Diffusional Broadening of Vesicular Packets of Catecholamines Released from Biological Cells during Exocytosis.” *Anal. Chem.*, **1992**, *64*, 3077–3083.

(81) Chabanon, M.; Ho, J. C. S.; Liedberg, B.; Parikh, A. N.; Rangamani, P. “Pulsatile Lipid Vesicles under Osmotic Stress.” *Biophys. J.*, **2017**, *112*, 1682–1691.

Chapter 2. CARBON NANOPROBES FOR LOW-NOISE, HIGH SPATIAL RESOLUTION MEASUREMENT OF CATECHOLAMINE RELEASE FROM DOPAMINERGIC NEURONS

2.1 INTRODUCTION

Amperometry is an electrochemical detection method that has proven invaluable for a quantitative understanding of chemical secretion in the brain (exocytosis), through its low limits of detection (a few thousand molecules) and fast temporal resolution (10 μs).[1-3] In single-cell amperometry, an ultramicroelectrode (typically carbon-fiber microelectrode, CFE) poised at an appropriate potential for neurotransmitter oxidation is approached to the surface of a secretory cell (e.g. neuroendocrine cells, neurons). Upon stimulation of exocytosis, secretory organelles called vesicles (e.g. large dense-core vesicles (LDCVs), synaptic vesicles (SVs)) are triggered to fuse with the outer cell membrane, releasing their cargo to the extracellular space, where they can be detected electrochemically.[4-6]

Amperometric signals contain a wealth of information, as they faithfully report the time course of neurotransmitter flux from individual vesicles. For example, the presence of a "pre-spike foot" (PSF) on an amperometric signal reflects the presence of a small fusion pore which physically restricts neurotransmitter diffusion out of the vesicle, often prior to full-collapse fusion and full release.[7,8] Careful studies of PSF characteristics have revealed that proteins (e.g. synaptotagmin I and IV,[9,10] actin[11]) and lipid bilayer membrane tension[12,13] play a role in supporting the formation of these initial fusion pores. Conversely, measurements at dopaminergic neurons in the rat midbrain revealed a "flickering fusion pore" in which neurotransmitter flux to the CFE changed rapidly, probably due to dynamic contractions and dilations of the SV fusion pore.[14] Amperometric events which displayed flickering fusion behavior released two-fold more dopamine than "simple" fusion events. Interestingly, the behavior could be controlled by

modulating protein kinase C activity pharmacologically, suggesting that flickering fusion may play a physiologically relevant role in regulating dopamine availability in the brain.

Nearly three decades have elapsed since the first demonstration of single-cell amperometry recordings,[15] but most studies have focused on LDCV exocytosis from neuroendocrine cells. This is because LDCVs are 200-400 nm in diameter and release 10^4-10^7 molecules in milliseconds, making them a straightforward analytical target. Relatively few studies exist, however, of SV exocytosis from neurons[16] – this is because SVs are only 40-50 nm in diameter and release a few thousand molecules in hundreds of microseconds.[17] With one notable exception (to the best of our knowledge),[18] no studies report direct measurement of single SV release sites (active zones).

Though it is widely known that postsynaptic mechanisms of facilitation and depression influence computation in the brain, it is less widely appreciated that presynaptic mechanisms modulate brain activity as well.[19-21] For example, it was recently revealed that synaptotagmin 7 is the "facilitation" sensor in central synapses, responsible for augmenting postsynaptic responses during elevated activity;[22] in another study, careful modeling of postsynaptic responses captured dynamic fusion behavior for single SVs,[23] similar to "flickering fusion" in dopaminergic SVs observed by the Sulzer group.[14] Clearly, a direct method for observing SV neurotransmitter release would improve the understanding of these processes.

We were therefore interested in developing high spatial resolution electrochemical probes for the measurement of catecholamine release single active sites on neurons. We developed a bench-top method for fabricating carbon nanoprobes (CNPs); CNPs could be fabricated with high success rate (~85%) in ~2 minutes. Depending on the orifice diameter of the quartz pipette used, CNPs ranging from 50-500 nm in diameter were fabricated, per electrochemical characterization with cyclic voltammetry. We qualitatively demonstrated that CNPs can resolve spatial heterogeneity of exocytosis release sites across the surface of a single PC12 cell. Finally, we established a novel neuronal model, precursor-derived human dopaminergic neuronal cells (HDNCs), and measured stimulated SV exocytosis of dopamine using CFEs and CNPs. Though we were successful in measuring SV exocytosis using CFEs, it was a challenge to identify and

record from candidate release sites with the CNPs. We suspect that this challenge is mainly due to diffusional broadening,[24] in which signal-to-noise ratio (SNR) of amperometric signals decreases dramatically as a consequence of release site-electrode spacing. Finite element simulations in COMSOL demonstrated that coulometric efficiency (i.e. ability to faithfully quantify neurotransmitter release) decreases dramatically as a function of distance from release site, especially for smaller probes. We close with an outlook for this work.

2.2 EXPERIMENTAL

2.2.1 Chemicals and Materials

Sodium chloride (NaCl), potassium chloride (KCl), magnesium chloride hexahydrate ($MgCl_2 \cdot 6H_2O$), calcium chloride ($CaCl_2$), HEPES (4-(2-hydroxyethyl)-1-piperazineethanesulfonic acid), glucose, ferrocenemethanol (FcMeOH), and L-3,4-dihydroxyphenylalanine (L-DOPA) were purchased from Sigma. All reagents used were reagent grade or better.

2.2.2 Rat Pheochromocytoma (PC12) Cell Culture

Stock PC12 cells were generously provided by Prof. Andrew Ewing (University of Gothenburg) and maintained as described previously.[14] Briefly, PC12 cells were grown on mouse collagen IV-coated culture dishes (VWR Scientific) in supplemented RPMI-1640 medium. Cells were maintained in a 7% CO_2, 37°C atmosphere and subcultured approximately every 7-9 days or when confluency was reached. Cells were used for experiments between days 5 and 12 of subculturing.

2.2.3 Culture of Normal Human Dopaminergic Neuronal Cells (HDNCs)

Stock normal human dopaminergic neuronal precursor cells, media, and supplements were obtained from Applied Biological Materials Inc. (abm, Canada). Cells were cultured as specified by manufacturer. Briefly, cells were seeded into culture flasks coated with human fibronectin. The culture media used for propagation was the Prigrow IV formulation (abm). Precursor cells were cultured and propagated into multiple culture flasks. At 50% confluence, the culture media was exchanged with a differentiation medium, which was the base culture medium supplemented with 2 mM L-glutamine, 1 mM dBcAMP

(Dibutyryl cyclic adenosine monophosphate), tetracycline (1 µg/mL), and Recombinant Human Glial-Derived Neurotrophic Factor (GDNF, 2 ng/mL). To support differentiation, neurons were supplemented with fresh differentiation media every day for 6 days, and after that every 2-3 days. Human dopaminergic neuronal cells (HDNCs) could be maintained for up to two weeks after differentiation without appreciable changes in cell health.

2.2.4 Fabrication of Electrodes: Carbon-Fiber Microelectrodes (CFEs)

CFEs were prepared by aspirating a carbon-fiber (5 µm) into a borosilicate glass capillary (1.2 mm O.D., 0.9 mm I.D., Sutter) that was pulled to a fine tip using a micropipette puller (Sutter). The microelectrode was cut and sealed in epoxy (Epoxy Technologies), followed by curing for 2 hours at 80°C and 2 hours at 150°C. CFEs were then polished at a 45° angle on a homebuilt micropipette beveler. CFEs were backfilled with 3 M KCl to establish electrical contact. CFEs were characterized by cyclic voltammetry by immersing them in 1 mM FcMeOH, 100 mM KCl and scanning the potential from -0.4 V to +0.6 V at a scan rate of 100 mV s^{-1} vs. Ag/AgCl reference electrode. Only CFEs with good electron transfer kinetics were used for experiments.

2.2.5 Fabrication of Electrodes: Carbon Nanoprobes (CNPs)

Similar to a previous report,[25] carbon nanoprobes (CNPs) were prepared as follows: Briefly, a quartz tube (1 mm O.D., 0.5 mm I.D., National Quartz) was pulled on a laser puller (P-2000, Sutter) to fabricate two identical micropipettes with fine tips. Then, the quartz pipette was connected directly to a CH_4 gas cylinder via Tygon tubing and pressurized with 40-45 p.s.i. CH_4 gas. The pipette was carefully inserted into another quartz tube (1.0 mm O.D., 0.7 mm I.D., Sutter), through which a low pressure (1-1.2 p.s.i.) of Ar gas was flowing. This quartz tube with Ar gas created an inert atmosphere that protected the CH_4-loaded pipette tip from oxidation/bending during pyrolysis. Then, the assembly was subjected to 2 minutes of direct heating *via* a butane torch (Amazon). This resulted in the pyrolysis of CH_4 into a solid, pyrolyzed carbon plug that closed the pipette tip. Electrical contact to the newly formed CNP was established via backfilling with 3 M KCl. CNPs were characterized via cyclic voltammetry by immersing

them in 1 mM FcMeOH, 100 mM KCl, and scanning the potential from -0.4 V to +0.6 V at a scan rate of 50 mV s^{-1} vs. Ag/AgCl reference electrode. CNP diameter was estimated from the magnitude of the steady-state current (i_{ss}). Only CNPs with good electron transfer kinetics were used for experiments.

2.2.6 Single Cell Amperometry

PC12 cells were bathed in pre-warmed 37 °C isotonic saline (150 mM NaCl, 5 mM KCl, 1.2 mM $MgCl_2 \cdot 6H_2O$, 2 mM $CaCl_2$, 5 mM glucose, and 10 mM HEPES, pH 7.4) for all experiments. Exocytosis from PC12 cells was measured by gently lowering CFEs or CNPs onto a cell-of-interest using a hydraulic micropositioner (MHW-3, Narishige). For CFEs, E_{app} = +0.7 V vs Ag/AgCl.

Cells were stimulated to exocytose using a 20 p.s.i., 5 s pulse (FemtoJet; Eppendorf) of physiological saline with 100 mM K^+ (iso-osmotically substituted with NaCl). Stimulation pipettes were cut to a diameter of about 10 µm and positioned 30-50 µm from a cell. Each cell was stimulated once. Experiments were maintained at 37 ± 1 °C (Warner Instruments). For L-DOPA experiments, cells were pre-incubated with 100 µM L-DOPA in isotonic saline for one hour.

For HDNCs, signals could not be observed under control conditions. As described in previous reports,[14,26] we pre-incubated neurons with 100 µM L-DOPA in isotonic saline for one hour prior to experiments. To record dopamine exocytosis from HDNCs, we positioned CFEs or CNPs at regions where we observed many neurites overlapping, as the number of active release sites was higher in these regions according to previous studies at rat dopaminergic neurons. We stimulated exocytosis using a 20 p.s.i., 5 s pulse (FemtoJet) of physiological saline with 100 mM K^+ (iso-osmotically substituted with NaCl). We recorded without moving the electrode for 2 minutes after each stimulation before moving to a new candidate release site.

2.2.7 Data Acquisition and Analysis

Electrodes were held at E_{app} vs. Ag/AgCl using a commercial patch-clamp current amplifier (Axopatch 200B; Axon Instruments). For PC12 cell experiments, the current was filtered at 2 kHz using an internal low-pass Bessel filter and sampled at 100 kHz using a Digidata 1322 digitizer (Axon

Instruments). For HDNC experiments, the current was low-pass filtered at 10 kHz, due to the microsecond timescale of synaptic vesicle release events (but see **Table S2.2**). Exocytotic spikes and their characteristics, including the spike characteristics i_{max} (peak amplitude, pA), $t_{1/2}$ (full-width of peak at half-maximum, ms), t_{rise} (10-90% max peak height, ms), t_{fall} (90-10% max peak heigh, ms), and Q (integrated charge, fC) were identified using pClamp v10.6 software (Axon Instruments). Spikes were identified if the i_{max} exceeded 5 × S.D. of the noise. All identified spikes were inspected, and unfit spikes were manually discarded (such as double or superimposed spikes).

Statistical significance was assessed using the Mann-Whitney-Wilcoxon Rank-Sum U-Test (Mann-Whitney). The Kolmogorov-Smirnov test (KS-test) was used to assess the differences in distributions. Statistics are reported as the mean ± S.E.M.

2.2.8 Finite Element Analysis in COMSOL

To model the effect of increasing electrode-release site distance on amperometric signals, we simulated the transport of catecholamines out of a 50 nm diameter synaptic vesicle in the middle of membrane fusion in COMSOL Multiphysics 5.2a (**Figure S2.6**). The length of the pore was 10 nm (the thickness of two lipid bilayers) and the radius of the fusion pore was set to 2.2 nm.[27] We set the internal concentration of the vesicle to 16,000 molecules (the average $N_{molecules}$ released from HDNCs after L-DOPA treatment, **Figure S2.2**) and the internal diffusion coefficient to be identical to the diffusion coefficient in the bulk (1×10^{-6} cm^2/s), as the contribution of the intravesicular matrix to neurotransmitter release in synaptic vesicle exocytosis is currently unclear. Diffusion of catecholamine was simulated using the Transport of Diluted Species (tds) interface, which models diffusion of a finite species using Fick's laws of diffusion.

To simulate the current-time course of release events, we created an electrode surface that converted species flux (mol/s) to current by multiplying by Faraday's constant (96485 C/mol) and the stoichiometric number of electrons transferred per catecholamine molecule ($n = 2$ e^-). We varied the size

of the electrode surface and the distance between the electrode and the release site to simulate the effects of probe size and diffusional broadening, respectively.

2.3 Results and Discussion

2.3.1 Fabrication and Characterization of Carbon Nanoprobes

To develop high spatial resolution carbon nanoprobes (CNPs), we adapted a fabrication protocol initially published by Takahashi and coworkers (**Scheme 2.1**).[25] First, a quartz pipette loaded with a high pressure of CH_4 gas (40 p.s.i.) was inserted into a quartz tube. By flowing a low pressure of Ar gas (1.0-1.2 p.s.i.) through the quartz tube, we ensured an inert atmosphere for heating such that the quartz pipette tip did not oxidize or bend due to direct application of the butane torch.

Next, the quartz pipette-tubing assembly was directly heated with a butane torch. CH_4 gas molecules were pyrolyzed into solid carbon, depositing a sooty film about the inner wall of the pipette. In the pipette tip region, the pyrolyzed carbon bridges across the pipette orifice to form a solid carbon plug, forming a CNP which can be used for electrochemical recording. **Figure 2.1** shows a scanning electron microscope (SEM) image of a typical exocytosis sensor (5 µm carbon-fiber microelectrode (CFE) beveled at 45° angle) vs. a ~0.3 µm CNP.

We characterized CNP diameter using cyclic voltammetry in 1 mM FcMeOH. By quantifying the steady-state limiting current (i_{ss}), once can estimate the radius of the ultramicroelectrode assuming the electrode geometry to be a disk,

$$i_{ss} = 4anFDC^*$$

Where a is the UME radius, n is the stoichiometric number of electrons transferred (1 e^- for FcMeOH), F is Faraday's constant (96,485 C mol^{-1}), D is the diffusion coefficient of FcMeOH (7×10^{-6} cm^2 s^{-1}), and C^* is the bulk concentration of FcMeOH (1 mM).[28] **Figure 2.2A** shows example cyclic voltammograms for CNPs fabricated under three different pipette conditions. As the geometry of the CNP is strongly influenced

by the geometry of the original quartz pipette, we reasoned that we could tune the diameter of CNPs by altering the fabrication parameters for the quartz pipette scaffolds. Consistent with expectation, finer pipettes (fabricated by tuning the "Heat" setting on the laser puller to higher values, **Figure 2.2B**) resulted in smaller diameter CNPs, from d ~ 500 nm at Heat = 550 to d ~ 260 nm at Heat = 650.

2.3.2 Carbon Nanoprobes Resolve Spatial Heterogeneity of Exocytosis at PC12 Cells

We demonstrated electrochemically that CNP fabrication can be well-controlled; we were able to reproducibly fabricate CNPs ranging in diameter from 50– 500 nm, with some as large as 1 μm (though we observed that CNPs are not always disk-shaped, data not shown). However, cyclic voltammograms reflect steady-state electrochemistry where the bulk concentration of a redox mediator is constant – in actuality, we desired to use CNPs to address catecholamine release from neurons, a transient process in which catecholamines must be captured for oxidation by a sensor.

To test the efficacy of CNPs for capturing exocytosis dynamics, we first used them to measure stimulated catecholamine exocytosis from PC12 cells (**Figure 2.3**). Previous measurements have demonstrated empirically with nanoelectrodes[29] or microelectrode arrays[30-32] that neuroendocrine cells (e.g. chromaffin, PC12 cells) exhibit heterogeneous exocytosis activity, i.e. LDCVs are not released uniformly about the cell. Indeed, exocytosis-competent sites are localized to heterogeneously distributed cholesterol-dependent membrane rafts, as PC12 cells depleted of cholesterol by cyclodextrin had a strong negative effect on the rate of exocytotic events, without changing the characteristics of individual events.[33]

Consistent with previous reports, we observed heterogeneity in exocytotic release sites across the surface of a single PC12 cell. **Figure 2.3A-E** shows a CNP recording stimulated exocytosis from a single PC12 cell at different positions (east, west, north, south, center, optical micrographs) with the corresponding amperometric trace collected from that position. The PC12 cell was stimulated every 2 minutes to allow the cell to recover from depolarization. **Figure 2.3F-J** shows the same CNP as in **Figure 2.3A-E** applied to a single PC12 cell treated with 100 μM L-DOPA. L-DOPA treatment increases catecholamine content of LDCVs by 250%.[34] As expected, we observed larger signals after L-DOPA treatment, but similar release

heterogeneity. The "pre-spike foot" (PSF) on the amperometric signal in the inset is a characteristic feature of some amperometric signals, denoting a stable but small fusion pore that physically restricts catecholamine diffusion to a steady state prior to full collapse of the vesicle into the cell membrane and complete release of catecholamines.[9-13]

2.3.3 Measuring Synaptic Vesicle Exocytosis from HDNCs: CFEs and CNPs

Having demonstrated qualitatively that CNPs are useful for studying exocytosis of LDCVs in PC12 cells, we turned to the study of synaptic vesicle (SV) exocytosis from dopaminergic neurons. LDCVs are 200-400 nm in diameter and release 10^4-10^7 catecholamine molecules (depending on cell preparation) on the millisecond timescale.[4] Conversely, SVs are 40-50 nm and release between thousands and tens of thousands of molecules in microseconds.[14,21,35]

We established a novel neuronal cell line, precursor cell-derived human dopaminergic neuronal cells (HDNCs) to develop SV exocytosis measurements. We found that HDNCs could be differentiated into dopaminergic neurons after 14 days *in vitro*, using a cocktail of differentiation factors (see *Section 2.2.3*). Differentiated neurons could be maintained for up to 21 days without appreciable changes in morphology if cultures were supplemented with fresh differentiation media every 2 days. However, as HDNCs formed a dense monolayer network with one another through their neurite projections, special care was taken when exchanging media for supplementing cultures or amperometric recordings – in one instance, media was added too quickly, which caused HDNCs to "round up" and detach from the substrate!

Under control conditions (isotonic saline, no prior treatment), HDNC recordings were exceptionally difficult. Previous amperometric measurements of SV exocytosis from rat midbrain neurons suggested that good candidate recording sites tended to occur at the overlap of several neurites (see **Figure 2.4**).[26] Indeed, we were sometimes able to observe K^+-stimulated exocytosis from these regions, but under control conditions the success rate was very low (10 events from 4/26 recording sites, **Table S2.1**). We found we were much more successful when we augmented the SV dopamine content *via* pre-treatment of

HDNCs with 100 µM L-DOPA prior to amperometric recordings (80 events from 7/20 recording sites, **Table S2.1**). Example amperometric events are collected from HDNCs are shown in **Figure 2.4C**.

The number of molecules ($N_{molecules}$) released during each amperometric event can be extracted from the integrated charge, Q, passed during the event through Faraday's equation: $Q = nFN$, where n is the stoichiometric number of electrons transferred per molecule oxidized (2 e^- for dopamine), F is Faraday's constant (96485 C mol^{-1}), and N is the number of moles oxidized. Interestingly, the calculated $N_{molecules}$ released during SV exocytosis from HDNCs agreed well with previous reports,[14,26,33] with 6,800 ± 1,700 molecules (n=10 events from 4 sites) released under control conditions and 16,700 ±1,700 molecules (n=80 events from 7 sites) released under L-DOPA pre-treatment (**Figure S2.2**). Consistent with Ca^{2+}-triggered SV exocytosis, no amperometric events were observed in the absence of Ca^{2+} (0 events from 20 sites, **Figure S2.5**). For detailed peak statistics, see **Figure S2.1 and Table S2.1**.

When we applied our CNPs to HDNCs, however, we were apparently less successful (**Figure 2.5**). **Figure 2.5A,C** shows a 500 nm CNP interfacing with a presumed HDNC presynaptic site and the corresponding amperometric trace. While the events look reasonable in their time course and shape, these recordings were notoriously difficult, due to the fragility and size of the CNPs. In addition, without a guide method (e.g. green fluorescent protein labeling of active sites), it was exceptionally difficult to identify candidate release sites. Events could only be observed after HDNCs were treated with L-DOPA, and of the observed events, the $N_{molecules}$ detected was significantly lower than what we had observed using CFEs (**Figure 2.5B,D** and **Figure S2.3**), implying that either SV efflux was not fully captured by CNPs (i.e. loss of analyte) or CNPs observed different SV release modes (i.e. kiss-and-run).[6] Notably, analysis of the interspike interval, Δt (the time between two events),[36] showed no significant difference between the Δt distributions collected using CFEs or CNPs (**Figure S2.4**), suggesting that CNPs were indeed observing the same process as CFEs (i.e. SV exocytosis).

2.3.4 Finite Element Analysis of Diffusional Broadening

We suspected CNPs detected far fewer $N_{molecules}$ than CFEs due to loss of analyte through diffusional broadening.[24] To confirm this suspicion, we simulated the efflux of catecholamines out of a synaptic vesicle using COMSOL Multiphysics 5.2a. **Figure 2.6A** shows a scheme of the simulation environment (for the actual environment, see **Figure S2.6**), with two variable parameters: the electrode radius, *r*, and the electrode-release site distance, *d*. At *t* = 0, 16,000 catecholamine molecules reside inside the synaptic vesicle (diameter = 50 nm), with the [catecholamine] = 0 everywhere else. When the simulation begins, catecholamines diffuse across the fusion pore and the electrode-release site gap to the electrode surface, where they are electrolyzed to generate a current. **Figure 2.6B** shows the consequence of changing the electrode-release site distance on observed current spikes for a 5 μm CFE – as the electrode-release site distance increases, the signal shape broadens in time and decreases in amplitude, which may lead to inaccurate quantification. However, at all distances tested (max *d* = 1 μm), the 5 μm CFE is capable of quantitative detection. When we repeated the simulation with a 500 nm CNP (**Figure 2.6D**), we observed the rate of current amplitude decrease with *d* was much more rapid, implying that fewer catecholamines were detected.

To be more quantitative, we integrated the area under each *i-t* curve to obtain the charge, *Q* in fC. By comparing *Q* at each distance with the initial *Q* (*d* = 100 nm), we extracted the coulometric efficiency (i.e. how quantitative the measurement is at different distances, with 1.0 being quantitative). As one can see in **Figure 2.6C**, the 5 μm CFE is steady near ~100% coulometric efficiency at all *d* tested, while all other probes exhibit a sharp decrease in coulometric efficiency with distance. For example, a 500 nm diameter CNP only detects ~30% of a release event at *d* = 1 μm. Interestingly, this is equivalent to ~4,800 molecules, consistent with our observed CNP measurement.

2.3 CONCLUSION

In conclusion, we developed a bench-top method for fabricating carbon nanoprobes (CNPs) ranging from 50-500 nm in diameter. CNPs could be fabricated in ~2 minutes and with an ~85% success rate.

CNPs demonstrate good electron-transfer kinetics and are useful for resolving the spatial heterogeneity of exocytosis release sites on the surface of neuroendocrine cells, e.g. PC12 cells.

We aimed to use these high spatial resolution probes to address single presynaptic active zones. We established a novel neuronal cell line, precursor-derived human dopaminergic neuronal cells (HDNCs). Measurements with 5 μm carbon-fiber microelectrodes (CFEs) suggested that HDNCs release synaptic vesicles (SVs) filled with dopamine. Under control conditions, SVs released only 6,800 molecules, but we collected very few events (n = 10). Pre-treating HDNCs with L-DOPA, a precursor for dopamine biosynthesis, resulted in a 250% increase in SV quantal size, releasing 16,700 molecules per SV. Consistent with Ca^{2+}-triggered exocytosis, we observed no SV release events when we measured HDNCs in Ca^{2+}-free media.

Somewhat expectedly, application of CNPs to HDNCs was fraught with challenges. The smaller probe size combined with the challenge of identifying candidate release sites made measurements under control conditions impossible. Pre-treatment of HDNCs with L-DOPA made measurements more successful, but the number of molecules detected per SV release event were far below expectation. While this may indicate that CNPs were able to get closer to release sites (due to their small size) and observe more subtle SV release activity, it is more likely that CNPs failed to accurately quantify SV release events due to the phenomenon of diffusional broadening. We provide computational evidence *via* finite element simulation that agrees well with this assessment.

Despite these challenges, it remains plausible that CNPs could be useful for quantifying SV exocytosis through their low noise and high spatial resolution. CNPs may benefit from increased sensitivity, but a key intervention for future experiments would be a label method for active release sites to guide the operator.

2.5 Schemes and Figures

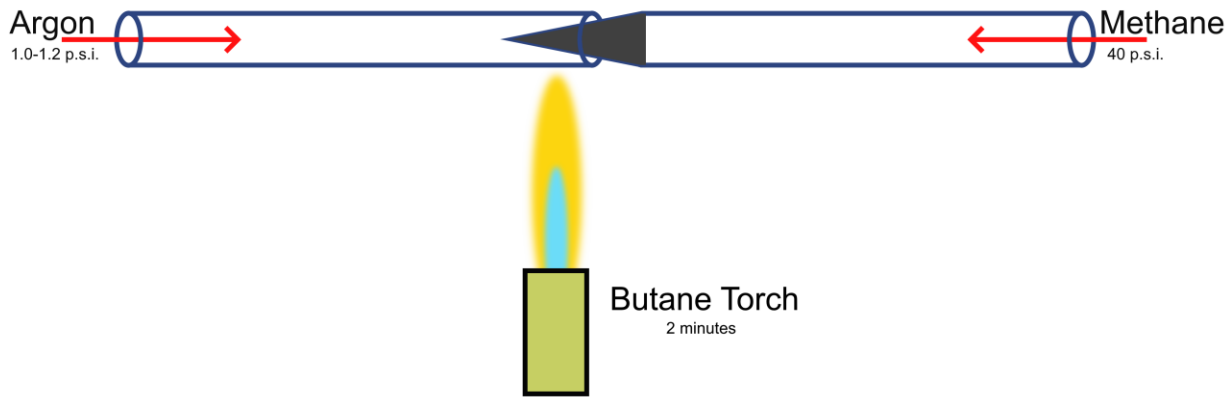

Scheme 2.1. Bench-top fabrication of carbon nanoprobes (CNPs). A quartz pipette (pressurized with 40 p.s.i. CH_4 gas) is inserted into a quartz capillary with an inert atmosphere (Ar gas, 1.0-1.2 p.s.i.). By applying a butane torch to the tip region for ~2 minutes, CH_4 is pyrolyzed, creating a solid carbon plug that fills the pipette tip. Creating an electrical connection to the carbon plug results in a carbon nanoprobe that can be used for electrochemistry.

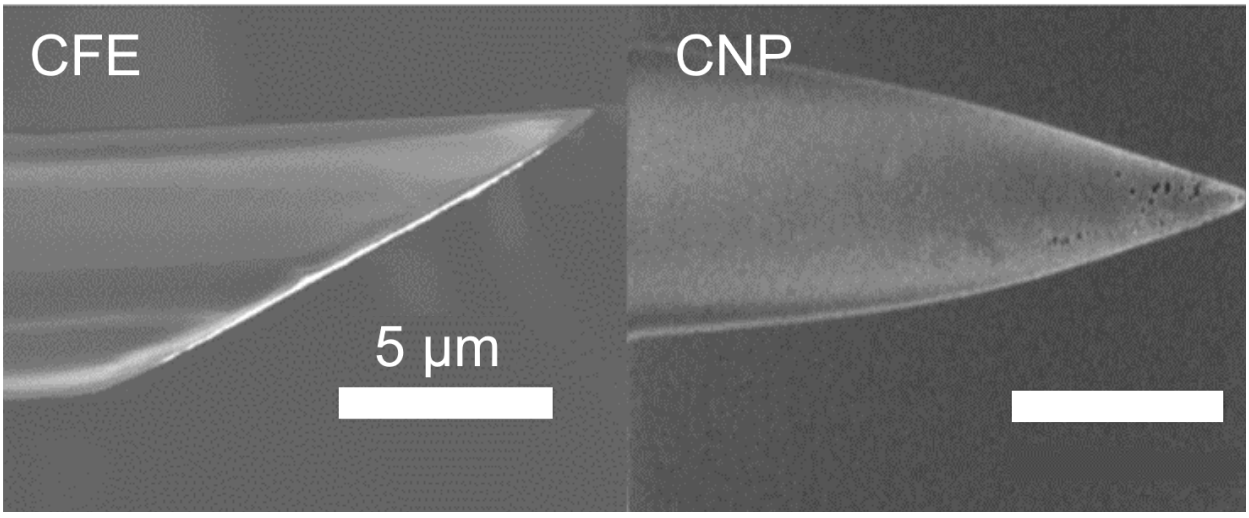

Figure 2.1. SEM images of electrodes. Comparison of carbon-fiber microelectrode (CFE) vs. a carbon nanoprobe (CNP). Scale bar 5 µm. We suspect the black entities near the tip of the CNP are due to the deposition of pyrolytic carbon on the outer wall of the pipette.

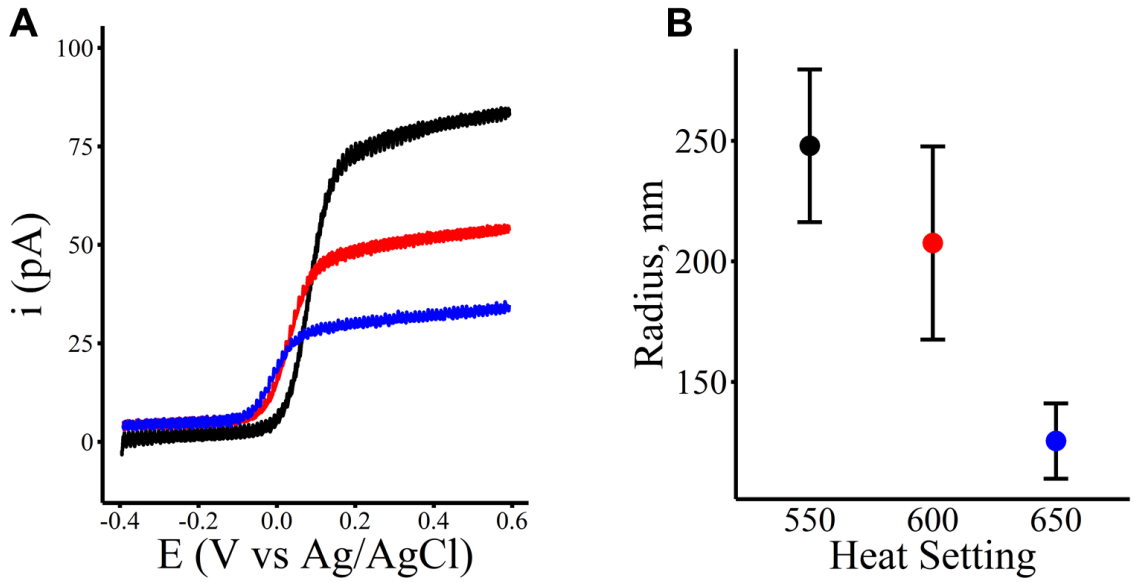

Figure 2.2. Pipettes used for CNP fabrication control CNP size. *A)* Cyclic voltammetry (CV) of three selected CNPs in 1 mM FcMeOH, 100 mM KCl. CNP potential scanned from -0.4 to 0.6 V vs. Ag/AgCl at 20 mV s^{-1}. Colors correspond to pipette pulling conditions, see *B*. *B)* Laser-pulled pipettes pulled under different conditions (Heat = 550, 600, 650) were used to fabricate CNPs. Using the steady-state limited current (i_{ss}), the radius of the CNP was calculated. Error bars are standard deviation (n=3).

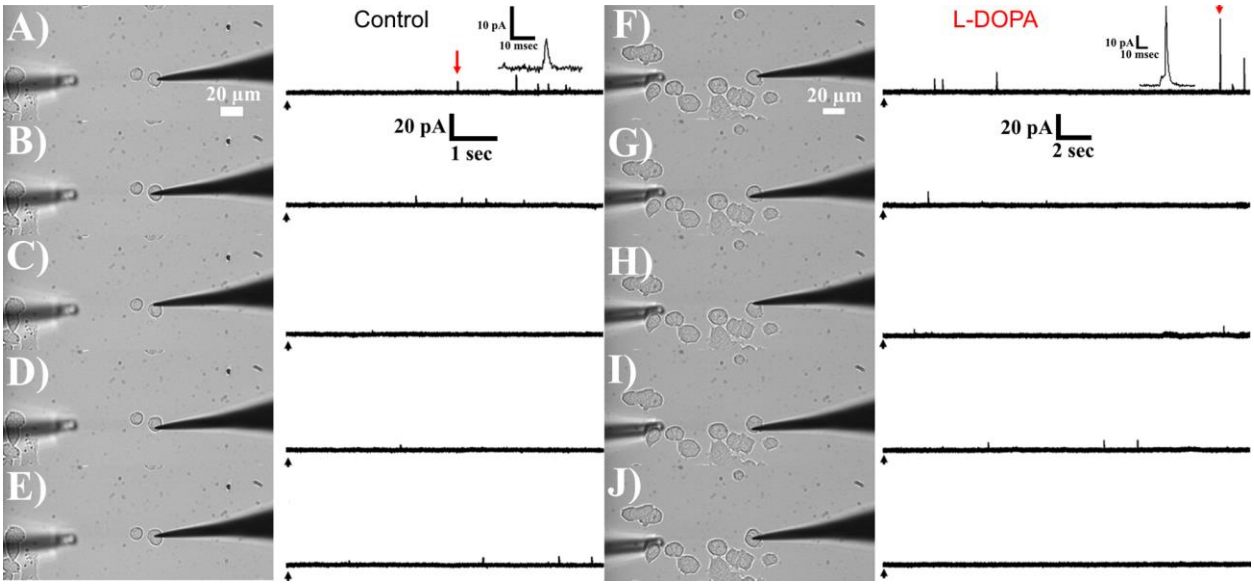

Figure 2.3. Resolving spatial heterogeneity of exocytosis release sites with CNPs. *A-E)* Measurements from different regions of a PC12 cell cultured under control conditions. A CNP was placed at different regions of the cell surface (east, west, north, south, center) and the cell was stimulated to exocytose with 100 mM K^+ injection (black arrows). The corresponding amperometric traces for each region are displayed. Inset, a selected amperometric signal (red arrow). *F-J)* Measurements from different regions of a PC12 cell treated with 100 µM L-DOPA for 1 hour prior to measurement. L-DOPA is a precursor to dopamine and augments vesicular dopamine concentration, resulting in larger exocytosis events. A CNP was placed at different regions of the cell surface (east, west, north, south, center) and the cell was stimulated to exocytose with 100 mM K^+ injection (black arrows). Inset, a selected amperometric signal (red arrow). Note the "pre-spike foot," which is indicative of a common low conductance state of the nascent fusion pore in which catecholamine release is restricted.

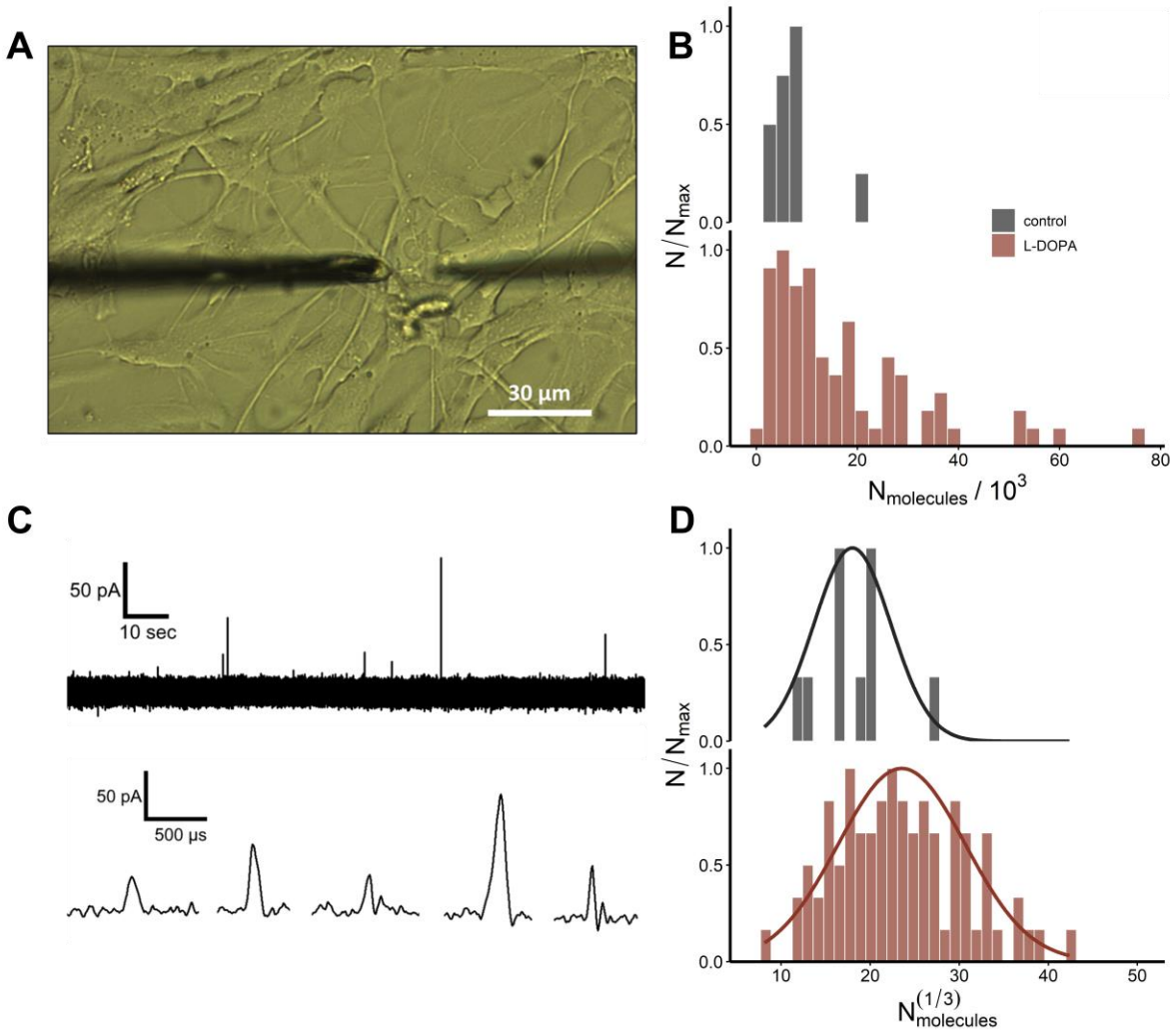

Figure 2.4. Measuring catecholamine release from single synaptic vesicles in HDNCs with 5 µm CFEs. *A)* Optical microscope image of cell amperometry at HDNCs. At left, a 5 µm CFE is gently placed at the convergence of several neurites, where synaptic vesicle release is most probable. At right, a stimulation pipette loaded with 100 mM K^+ is positioned for delivery of a 20 p.s.i., 5 s pulse in order to depolarize neurons and stimulate exocytosis. *C)* An example amperometric trace collected from HDNCs. Several current transients can be seen over the course of ~1 min. Selected current transients are shown on an expanded timescale below. Three of them exhibit a single rising and falling phase (simple), while two of them have multiple rising and falling phases (complex) consistent with "flickering fusion." *B)* Histogram of $N_{molecules}$ per event recorded under control conditions and L-DOPA conditions (augmented vesicle content). Events are more readily detected after quantal size is increased by L-DOPA treatment. *D)* Cube-root transformation of events shown in *B.* Cube-root transformation is well fit by a Gaussian, consistent with previous reports.[15] See **Table S2.1** and **Figure S2.1**, **Figure S2.2** for more detailed statistics.

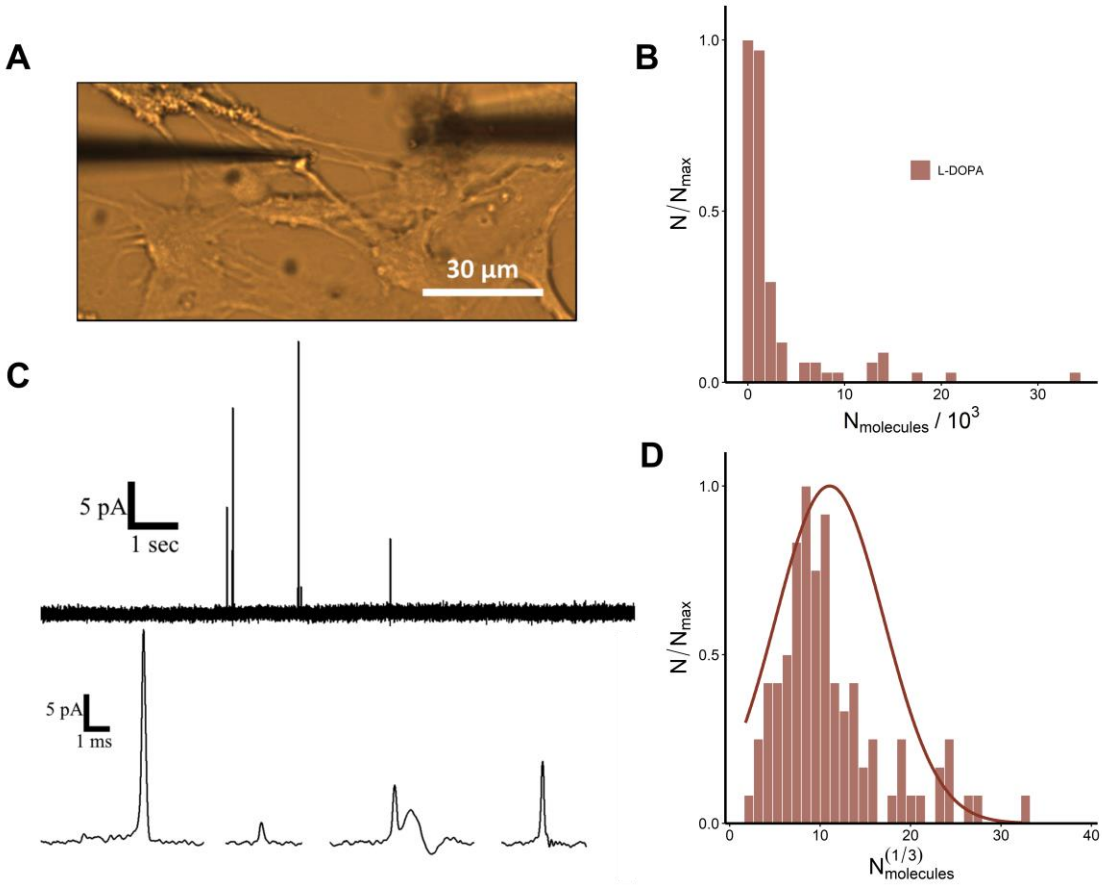

Figure 2.5. Measuring catecholamine release from single synaptic vesicles in HDNCs with 500 nm CNPs. *A)* Optical microscope image of cell amperometry at HDNCs. At left, a 500 nm CNP is gently placed at a presumed presynaptic nodule near the convergence of several neurites. At right, a stimulation pipette loaded with 100 mM K^+ is positioned for delivery of a 20 p.s.i., 5 s pulse in order to depolarize neurons and stimulate exocytosis. *C)* An example amperometric trace collected from HDNCs. Several current transients can be seen over the course of ~1 min. Selected current transients are shown on an expanded timescale below. Three of them exhibit a single rising and falling phase (simple), while one has multiple rising and falling phases (complex) consistent with "flickering fusion." *B)* Histogram of $N_{molecules}$ per event recorded under L-DOPA conditions (augmented vesicle content). No events were observed under control conditions with CNPs. *D)* Cube-root transformation of events shown in *B.* The cube-root transformation shown here is not very well fit by a Gaussian, perhaps reflecting the need for more events. See **Table S2.2** and **Figure S2.3** for more detailed statistics.

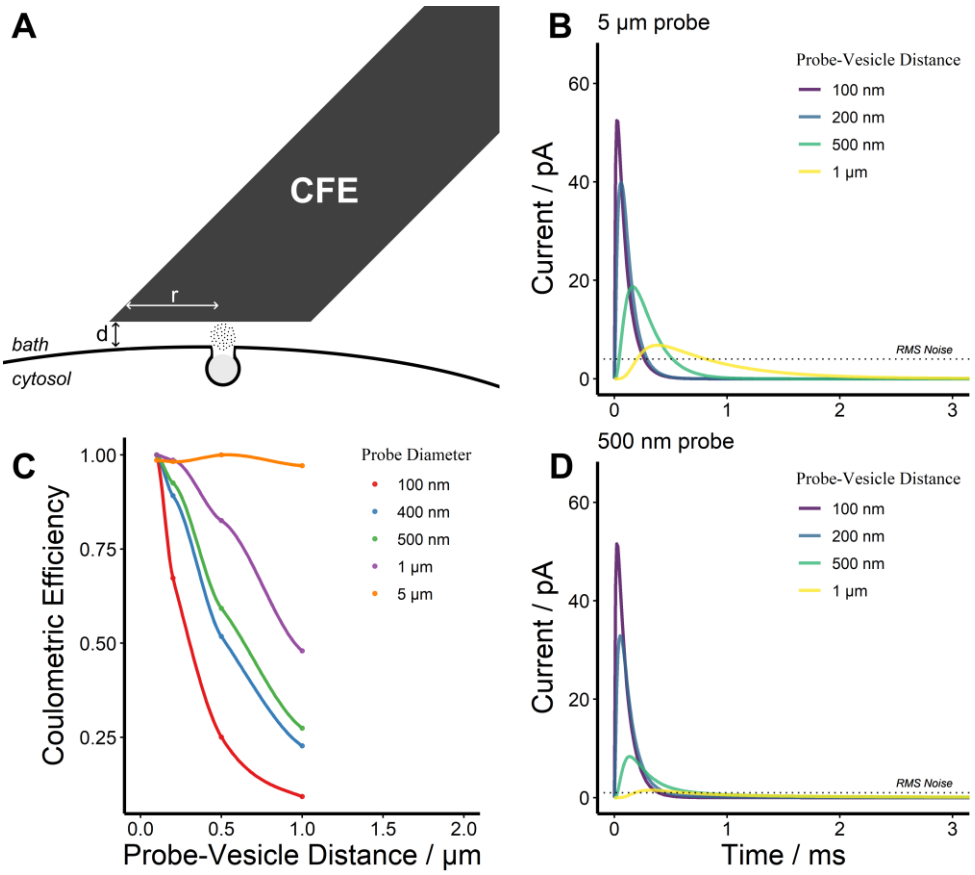

Figure 2.6. The effects of diffusional broadening on HDNC amperometry with different probe sizes – COMSOL. A) Cartoon of simulation environment, not drawn to scale. d is the spacing between the electrode surface and the release site, r is the radius of the electrode surface. For the actual simulation environment, see Figure S2.6. B) Diffusional broadening effect at different probe-release site distances, d, for a 5 µm probe (CFE). The detection threshold (RMS noise) is indicated by the dotted line. C) The coulometric efficiency for different probe sizes as a function of probe-release site distance, d. For all probes other than 5 µm CFE, significant loss of catecholamine signal occurs by 500 nm separation distance. D) The same simulation as in B, but the probe is a 500 nm CNP. Dotted line indicates RMS noise detection threshold.

Condition	N_{events}	N_{sites}^{+} / N_{sites}^{total}	I_{max} (pA)	$t_{1/2}$ (µs)	t_{rise} (µs)	t_{fall} (µs)	$N_{molecules}$ (10^3)	Interspike interval (s)
control	10	4 / 26	24.7 ± 4.8	60 ± 10	40 ± 10	80 ± 20	6.8 ± 1.7	10.3 ± 4.7
100 µM L-DOPA	80	7 / 20	26.9 ± 2.4	80 ± 10	80 ± 10	100 ± 10	16.7 ± 1.7	4.6 ± 1.1
Ca^{2+}-free	-	0 / 20	-	-	-	-	-	-

Table S2.1. Characteristics of amperometric events collected from HDNCs with 5 µm CFE. Amperometric events were collected from HDNCs using a 5 µm CFE poised at +700 mV vs. Ag/AgCl reference. Events were recorded under three different conditions: control (no supplements added to neuronal media), 100 µM L-DOPA (see *Section 2.2.6*), and Ca^{2+}-free (10 mM EGTA, a calcium chelator, added to isotonic saline and Ca^{2+} removed). In all cases, HDNCs were stimulated to exocytose *via* a 20 p.s.i., 5 s pulse of 100 mM K^{+} solution (see *Section 2.2.6*). Events were analyzed for the maximum amplitude (I_{max}), duration ($t_{1/2}$), rise time (t_{rise}), and fall time (t_{fall}), $N_{molecules}$, and interspike interval (time between consecutive peaks). The number of events collected at each condition are given as N_{events}. We also provide a metric for successful neuronal recordings – recording sites where we observed at least 1 event – as N_{sites}^{+} / N_{sites}^{total}. In the bottom row, we show that no events were recorded in the Ca^{2+}-free condition (**Figure S2.5**).

Probe Type	N_{events}	N_{sites}^{+} / N_{sites}^{total}	I_{max} (pA)	$t_{1/2}$ (µs)	t_{rise} (µs)	t_{fall} (µs)	$N_{molecules}$ (10^3)	Interspike interval (s)
5 µm CFE	80	7 / 20	26.9 ± 2.4	80 ± 10	80 ± 10	100 ± 10	16.7 ± 1.7	4.6 ± 1.1
500 nm CNP	95	9 / 20	2.38 ± 0.35	310 ± 30	190 ± 10	100 ± 10	2.8 ± 0.5	6.4 ± 1.6

Table S2.2. Characteristics of amperometric events collected from HDNCs with CFE or CNP. Amperometric events were collected from HDNCs using a 5 µm CFE or 500 nm CNP poised at +700 mV vs. Ag/AgCl reference. For all measurements, HDNCs were pre-incubated with 100 µM L-DOPA (see *Section 2.2.6*). HDNCs were stimulated to exocytose *via* a 20 p.s.i., 5 s pulse of 100 mM K^+ solution (see *Section 2.2.6*). Events were analyzed for the maximum amplitude (I_{max}), duration ($t_{1/2}$), rise time (t_{rise}), and fall time (t_{fall}), $N_{molecules}$, and interspike interval (time between consecutive peaks). The number of events collected at each condition are given as N_{events}. We also provide a metric for successful neuronal recordings – recording sites where we observed at least 1 event – as N_{sites}^{+} / N_{sites}^{total}. The dramatic difference in event timescale (e.g. $t_{1/2}$, t_{rise}, t_{fall}) observed between CFE and CNP recordings reflects the different low-pass filtering used in each set of experiments. CFE events were recorded with a 10 kHz internal low-pass Bessel filter, while CNP events were recorded with a 2 kHz internal low-pass Bessel filter, to make it easier to identify HDNC events (lower noise with lower filtering frequency). While this discrepancy between recordings results in temporal broadening,[37] the integrated area under each peak is comparable.[38]

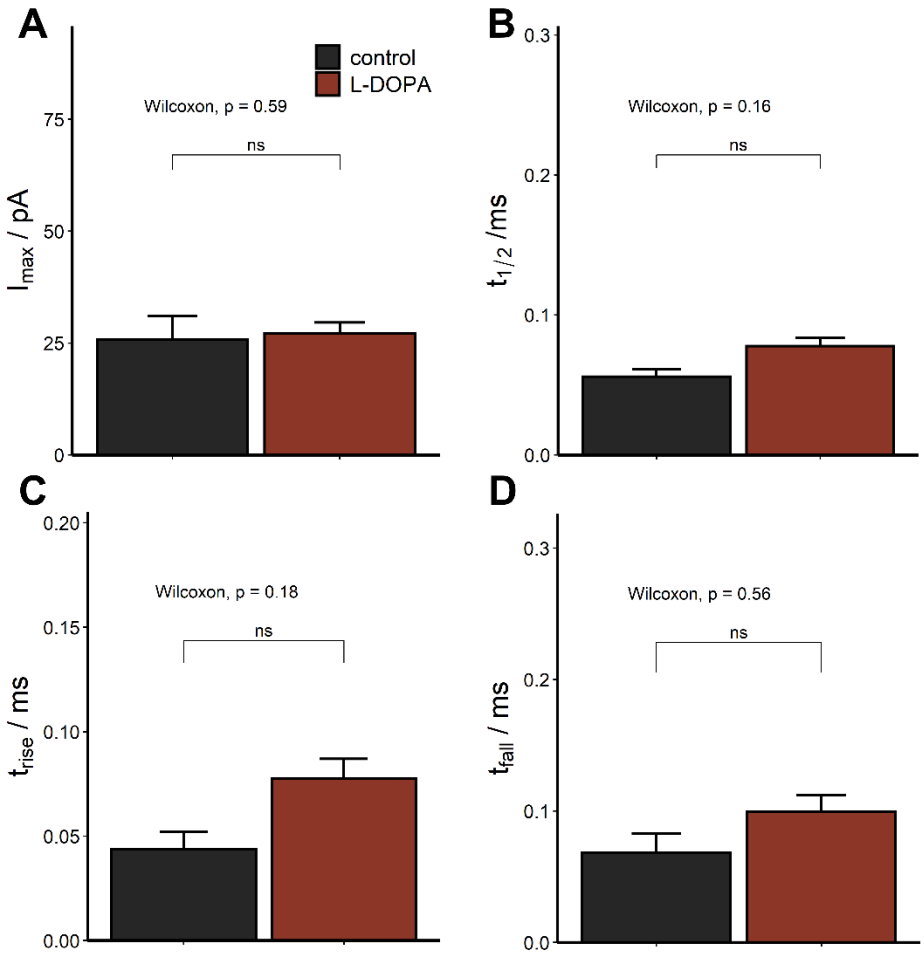

Figure S2.1. Peak characteristics of HDNC events collected with 5 µm CFE under different culture conditions. HDNCs were measured under control (black) or 100 µM L-DOPA (red) using a 5 µm CFE. Events were collected after stimulation of neurons with 100 mM K^+. Bar plots showing: *A)* I_{max}; *B)* $t_{1/2}$; *C)* t_{rise}; *D)* t_{fall}. Statistical significance was assessed using Mann-Whitney Wilcoxon (Wilcoxon) test.

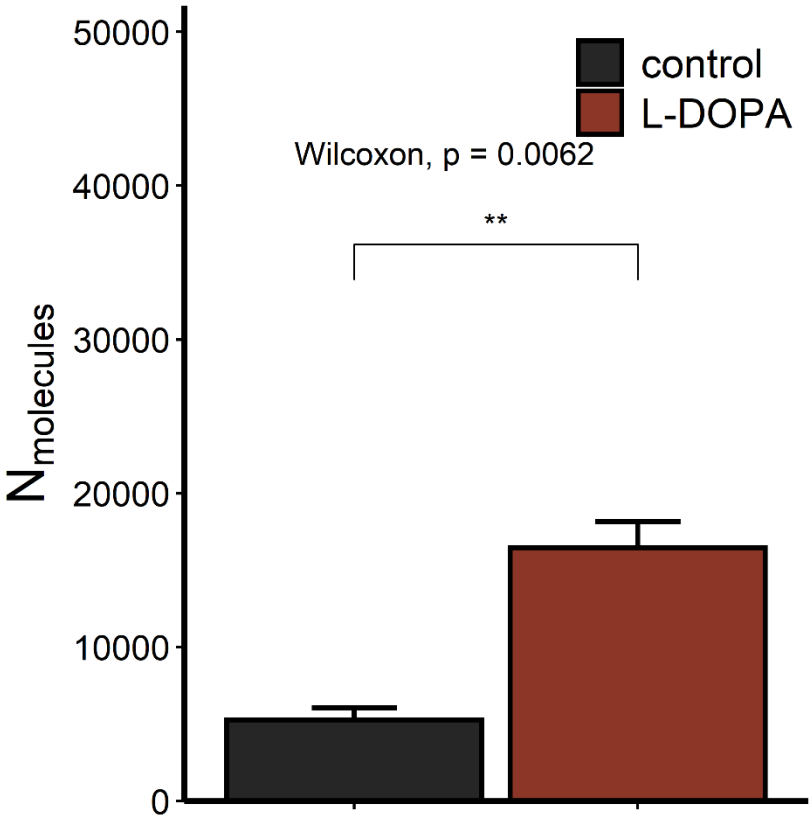

Figure S2.2. Measured $N_{molecules}$ released from HDNC events collected with 5 µm CFE under different culture conditions. HDNCs were measured under control (black) or 100 µM L-DOPA (red) using a 5 µm CFE. Events were collected after stimulation of neurons with 100 mM K^+. Shown is a bar plot of $N_{molecules}$ released under each condition. The average $N_{molecules}$ per event changed from 6,800 ± 1,700 molecules under control conditions (N_{events} = 10), to 16,700 ± 1,700 molecules after pre-incubation with 100 µM L-DOPA for 1 hour (N_{events} = 80). This is consistent with a 250% increase in quantal size reported in the literature.[34] Statistical significance was assessed using Mann-Whitney Wilcoxon (Wilcoxon) test.

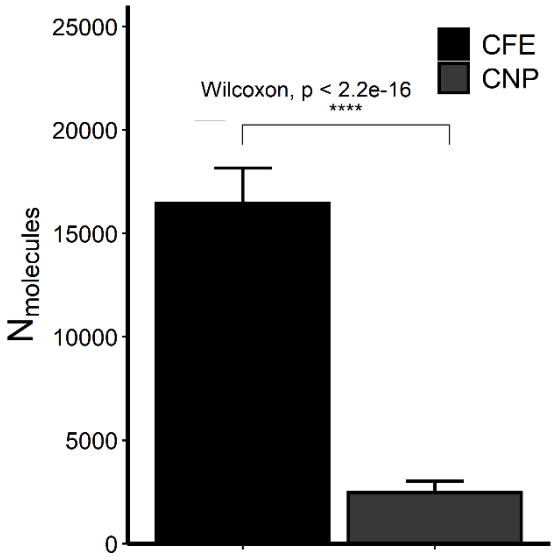

Figure S2.3. Measured $N_{molecules}$ released from HDNC events collected with 5 µm CFE or 500 nm CNP after L-DOPA treatment. HDNCs were measured with a 5 µm CFE (black) or a 500 nm CNP (grey) after pre-incubation with 100 µM L-DOPA for 1 hour. Events were collected after stimulation of neurons with 100 mM K^+. Shown is a bar plot of $N_{molecules}$ per event for each probe type. The average $N_{molecules}$ per event collected with CFE was 16,700 ± 1,700 molecules (N_{events} = 80). Average $N_{molecules}$ per event collected with CNP was 2,800 ± 500 molecules (N_{events} = 95). This dramatic difference in $N_{molecules}$ ($p < 2.2 \times 10^{-16}$) as a function of probe may reflect sub-quantitative detection or very short, small events that CFEs fail to detect due to differences in limit of detection (LOD).

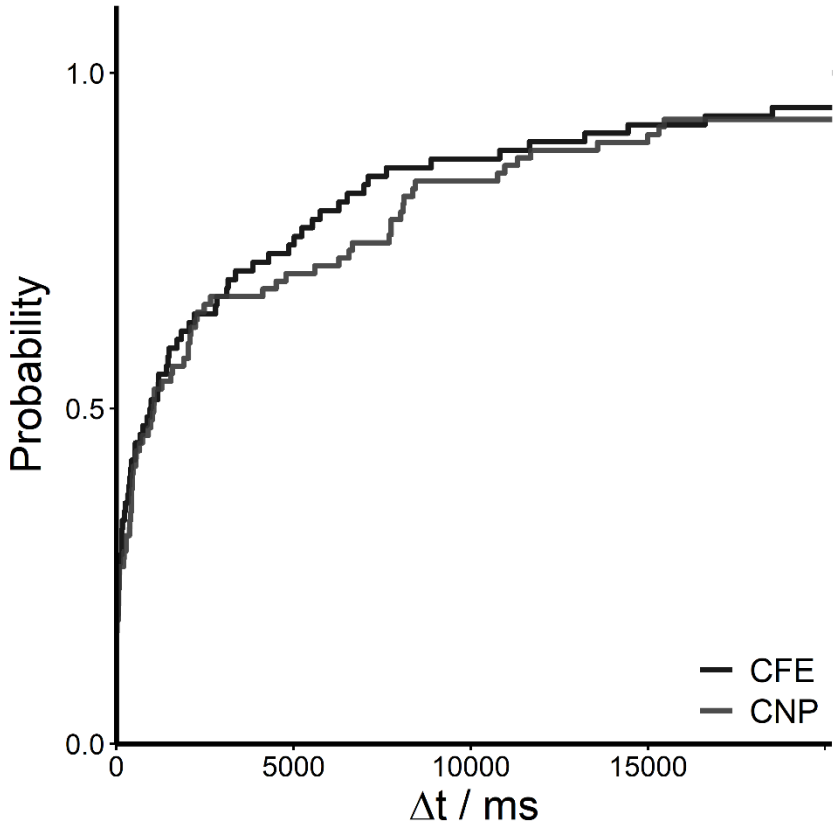

Figure S2.4. CFEs and CNPs record similar release profiles from HDNCs. The interspike interval (Δt, ms) between consecutive events in an amperometric trace can be used to assess differences in exocytosis between experiments. Here, we compare the cumulative probability distribution of interspike intervals between CFE and CNP recordings. There was no statistically significant difference (Kolmogorov-Smirnov Test, Mann-Whitney Wilcoxon test) between the distributions, implying that CFEs and CNPs are probably recording the same phenomenon.

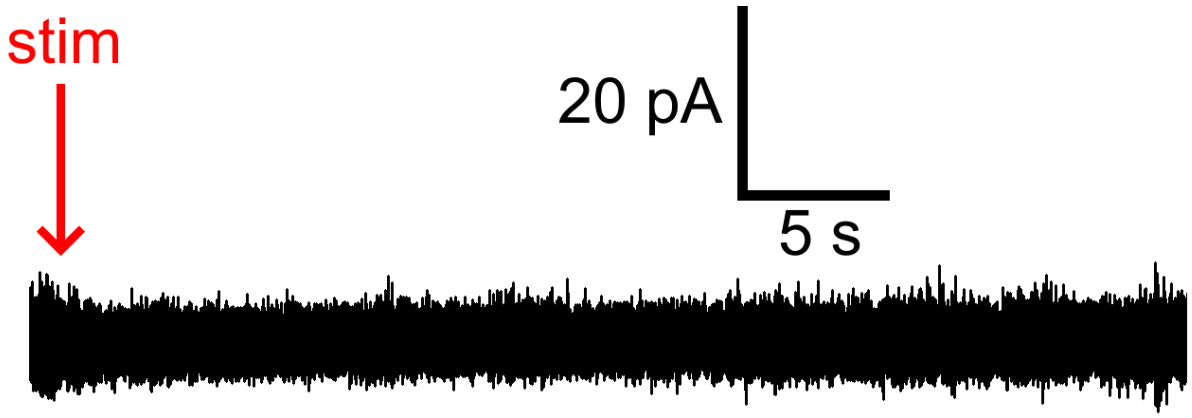

Figure S2.5. No events were observed in Ca^{2+}-free media. Shown is an example amperometric trace in Ca^{2+}-free media. Consistent with SNARE-triggered vesicle fusion, no amperometric events were observed at HDNCs with 5 µm CFE in the absence of Ca^{2+} (in the isotonic saline recording buffer, $[Ca^{2+}]$ = 0 mM and [EGTA] = 10 mM to chelate any trace Ca^{2+} ions). The red arrow (stim) indicates when a 100 mM K^+ stimulation buffer (with $[Ca^{2+}]$ = 0 mM and [EGTA] = 10 mM) was injected using a 20 p.s.i., 5 s pulse. This is sufficient to depolarize the membrane and open voltage-gated Ca^{2+} channels, but in the absence of Ca^{2+}, synaptic vesicle fusion and amperometric events corresponding to the oxidation of released catecholamines are abolished.

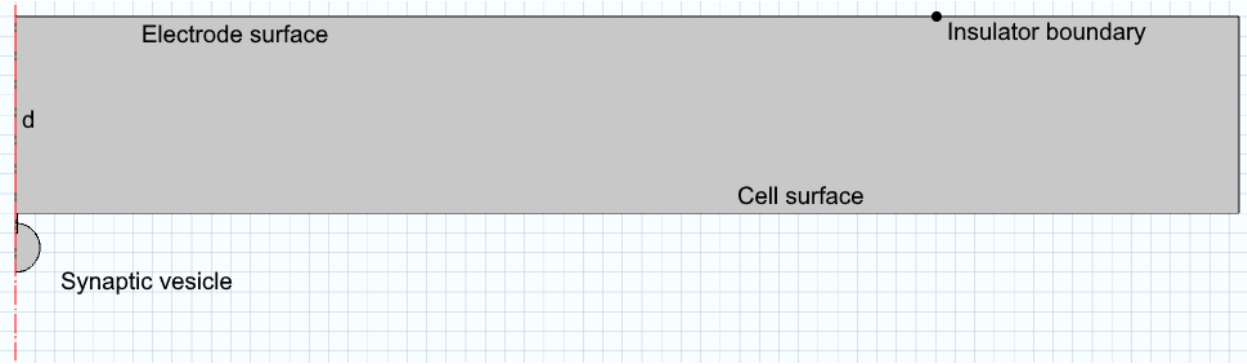

Figure S2.6. COMSOL simulation geometry – Diffusional Broadening. A concentration (C_{int}) of catecholamine is initially in the synaptic vesicle at t = 0. The diffusion coefficient of catecholamine is the same everywhere ($D = 1 \times 10^{-6}$ cm^2 s^{-1}). When the simulation is initiated, catecholamines diffuse (time-dependent) out of the 25 nm radius synaptic vesicle across the 10 nm long, 2.2 nm radius fusion pore, traversing the electrode-release site distance, d (here, d = 200 nm) to the electrode surface (here, electrode radius r = 2.5 µm, corresponding to a CFE). The flux of catecholamines (mol/s) are consumed at the electrode surface, generating a current proportional to the $flux * F * n$ (see main text). The cell surface and insulator boundary are no flux surfaces that do not interact with diffusing catecholamines.

By varying d and the r, we quantitatively described the negative effects of diffusional broadening and probe size on capturing synaptic vesicle efflux.

2.6 REFERENCES

(1) Robinson, D. L.; Hermans, A.; Seipel, A. T.; Wightman, R. M. "Monitoring Rapid Chemical Communication in the Brain." *Chem. Rev.*, **2008**, *108*, 2554–2584.

(2) Mosharov, E. V. & Sulzer, D. "Analysis of exocytotic events recorded by amperometry." *Nat. Methods*, **2008**, *2*, 651–658.

(3) Bucher, E. S. & Wightman, R. M. "Electrochemical Analysis of Neurotransmitters." *Annu. Rev. Anal. Chem.*, **2015**, *8*, 239–261.

(4) Burgoyne, R. D. & Morgan, A. "Secretory granule exocytosis." *Physiol. Rev.*, **2003**, *83*, 581-632.

(5) Südhof, T. C. "The synaptic vesicle cycle." *Annu. Rev. Neurosci.*, **2004**, *27*, 509–547.

(6) Alabi, A. A. & Tsien, R. W. "Perspectives on Kiss-and-Run: Role in Exocytosis , Endocytosis , and Neurotransmission." *Annu. Rev. Physiol.*, **2013**, *75*, 393–422.

(7) Jackson, M. B. "In search of the fusion pore of exocytosis." *Biophys. Chem.*, **2007**, *126*, 201–208.

(8) Oleinick, A., Lematire, F., Collignon, M. G., Svir, I., & Amatore, C. "Vesicular release of neurotransmitters: converting amperometric measurements into size , dynamics and energetics of initial fusion pores." *Farad. Discuss.*, **2013**, *164*, 33–55.

(9) Wang, C.; Grishanin, R.; Earles, C. A.; Chang, P. Y.; Martin, T. F. J.; Chapman, E. R.; Jackson, M. B. "Synaptotagmin Modulation of Fusion Pore Kinetics in Regulated Exocytosis of Dense-Core Vesicles." *Science*, **2001**, *294*, 1111–1116.

(10) Wang, C. T.; Lu, J. C.; Bai, J.; Chang, P. Y.; Martin, T. F. J.; Chapman, E. R.; Jackson, M. B. "Different domains of synaptotagmin control the choice between kiss-and-run and full fusion." *Nature*, **2003**, *424*, 943–947.

(11) Berberian, K.; Torres, A. J.; Fang, Q.; Kisler, K.; Lindau, M. "F-Actin and Myosin II Accelerate Catecholamine Release from Chromaffin Granules." *J. Neurosci.*, **2009**, *29*, 863–870.

(12) Sombers, L. A. et al. "The Effects of Vesicular Volume on Secretion through the Fusion Pore in Exocytotic Release from PC12 Cells." *J. Neurosci.*, **2004**, *24*, 303–309.

(13) Sombers, L. A.; Wittenberg, N. J.; Maxson, M. M.; Adams, K. L.; Ewing, A. G. "High osmolarity and L-DOPA augment release via the fusion pore in PC12 cells." *ChemPhysChem*, **2004**, *8*, 2471–2477.

(14) Staal, R. G. W.; Mosharov, E. V.; & Sulzer, D. "Dopamine neurons release transmitter via a flickering fusion pore." *Nat. Neurosci.*, **2004**, *7*, 341–346.

(15) Wightman, R. M. et al. "Temporally resolved catecholamine spikes correspond to single vesicle release from individual chromaffin cells." *Proc. Natl. Acad. Sci.*, **1991**, *88*, 10754–10758.

(16) Phan, N. T. N.; Li, X.; Ewing, A. G. “Measuring synaptic vesicles using cellular electrochemistry and nanoscale molecular imaging.” *Nat. Rev. Chem.*, **2017**, *1*, 1–18.

(17) Chang, C. W.; Chiang, C. W.; Jackson, M. B. “Fusion pores and their control of neurotransmitter and hormone release.” *J. Gen. Physiol.*, **2017**, *149*, 301–322.

(18) Li, Y. T., et al. “Real-time Monitoring of Discrete Synaptic Release Events and Excitatory Potentials within Self-reconstructed Neuromuscular Junctions.” *Angew. Chem. Int. Ed.*, **2015**, *54*, 9313–9318.

(19) Sulzer, D. & Pothos, E. N. “Regulation of quantal size by presynaptic mechanisms.” *Rev. Neurosci.*, **2000**, *11*, 159–212.

(20) Edwards, R. H. “The Neurotransmitter Cycle and Quantal Size.” *Neuron*, **2007**, *55*, 835–858.

(21) Sulzer, D.; Cragg, S. J.; Rice, M. E. “Striatal dopamine neurotransmission: regulation of release and uptake.” *Basal Ganglia*, **2016**, *6*, 123–148.

(22) Jackman, S. L.; Turecek, J.; Belinsky, J. E.; Regehr, W. G. “The calcium sensor synaptotagmin 7 is required for synaptic facilitation.” *Nature*, **2016**, *529*, 88–91.

(23) Chapochnikov, N. M. et al. “Uniquantal release through a dynamic fusion pore is a candidate mechanism of hair cell exocytosis.” *Neuron*, **2014**, *83*, 1389–1403.

(24) Schroeder, T. J.; Jankowski, J. A.; Kawagoe, K. T.; Wightman, R. M.; Lefrou, C.; Amatore, C. “Analysis of Diffusional Broadening of Vesicular Packets of Catecholamines Released from Biological Cells during Exocytosis.” *Anal. Chem.*, **1992**, *64*, 3077–3083.

(25) Takahashi, Y. et al. “Multifunctional nanoprobes for nanoscale chemical imaging and localized chemical delivery at surfaces and interfaces.” *Angew. Chem. Int. Ed.*, **2011**, *50*, 9638–9642.

(26) Pothos, E. N.; Davila, V.; Sulzer, D. “Presynaptic Recording of Quanta from Midbrain Dopamine Neurons and Modulation of the Quantal Size.” *J. Neurosci.*, **1998**, *18*, 4106–4118.

(27) Jackson, M. B. “Minimum membrane bending energies of fusion pores.” *J. Memb. Biol.*, **2009**, *231*, 101–115.

(28) Bard, A. J.; Faulkner, L. R. *Electrochemical Methods: Fundamentals and Applications*; John Wiley & Sons, 2000.

(29) Wu, W. Z.; Huang, W. H.; Wang, W.; Wang, Z. L.; Cheng, J. K.; Xu, T.; Zhang, R. Y.; Chen, Y.; Liu, J. “Monitoring dopamine release from single living vesicles with nanoelectrodes.” *J. Am. Chem. Soc.*, **2005**, *127*, 8914–8915.

(30) Zhang, B.; Adams, K. L.; Luber, S. J.; Eves, D. J.; Heien, M. L.; Ewing, A. G. “Spatially and Temporally Resolved Single-Cell Exocytosis Utilizing Individually Addressable Carbon Microelectrode Arrays.” *Anal. Chem.*, **2008**, *80*, 1394–1400.

(31) Zhang, B.; Heien, M. L. A. V.; Santillo, M. F.; Mellander, L.; Ewing, A. G. “Temporal Resolution in Electrochemical Imaging on Single PC12 Cells Using Amperometry and Voltammetry at Microelectrode Arrays.” *Anal. Chem.*, **2011**, *83*, 571–577.

(32) Gosso, S.; Turturici, M.; Franchino, C.; Colombo, E.; Pasquarelli, A.; Carbone, E.; Carabelli, V. “Heterogeneous distribution of exocytotic microdomains in adrenal chromaffin cells resolved by high-density diamond ultra-microelectrode arrays.” *J. Physiol.*, **2014**, *592*, 3215–3230.

(33) Lang, T.; Bruns, D.; Wenzel, D.; Riedel, D.; Holroyd, P.; Thiele, C.; Jahn, R. “SNAREs are concentrated in cholesterol-dependent clusters that define docking and fusion sites for exocytosis.” *EMBO J.*, **2001**, *20*, 2202–2213.

(34) Pothos, E.; Desmond, M.; Sulzer, D. “L-3,4-Dihydroxyphenylalanine Increases the Quantal Size of Exocytotic Dopamine Release In Vitro.” *J. Neurochem.*, **1996**, *66*, 629–636.

(35) Omiatek, D. M.; Bressler, A. J.; Cans, A. S.; Andrews, A. M.; Heien, M. L.; Ewing, A. G. “The real catecholamine content of secretory vesicles in the CNS revealed by electrochemical cytometry.” *Scientific Reports*, **2013**, *3*:1447.

(36) Bruns, D.; Riedel, D.; Klingauf, J.; Jahn, R. “Quantal release of serotonin.” *Neuron*, **2000**, *28*, 205–220.

(37) Robinson, D. A.; Edwards, M. A.; Ren, H.; White, H. S. “Effects of Instrumental Filters on Electrochemical Measurement of Single-Nanoparticle Collision Dynamics.” *ChemElectroChem*, **2018**, *5*, 3059–3067.

(38) Hochstetler, S. E.; Puopolo, M.; Gustincich, S.; Raviola, E.; Wightman, R. M. “Real-Time Amperometric Measurements of Zeptomole Quantities of Dopamine Released from Neurons.” *Anal. Chem.*, **2000**, *72*, 489–496.

Chapter 3. ELECTRODEPOSITED GOLD ON CARBON-FIBER MICROELECTRODES FOR ENHANCING AMPEROMETRIC DETECTION OF DOPAMINE RELEASE FROM PHEOCHROMOCYTOMA CELLS

The work presented in this chapter has been published in the following paper:

1) Barlow, S. T.; Louie, M.; Hao, R.; Defnet, P. A.; Zhang, B. "Electrodeposited Gold on Carbon-Fiber Microelectrodes for Enhancing Amperometric Detection of Dopamine Release from Pheochromocytoma Cells." Analytical Chemistry, ***2018****, 90, 10049–10055.*

3.1 INTRODUCTION

Electrochemical methods for the sensitive and ultrafast detection of exocytosis are centrally important to a quantitative understanding of chemical communication in the brain.[1] The primary advantages of electrochemical measurements, such as amperometry, lie in their fast temporal resolution (submillisecond) and low limits of detection (e.g., a few thousand molecules).[2,3] Amperometry with carbon-fiber microelectrodes (CFEs) has been applied for the past few decades to the detection of exocytosis from a variety of cell types, allowing quantification of neurotransmitter release from the small synaptic vesicles (~50 nm diameter) of ventral midbrain neurons[4,5] as well as from the large dense-core vesicles (~130 nm radius in chromaffin cells,[6] ~100 nm radius in pheochromocytoma (PC12) cells[7]) of neuroendocrine cells.[8,9] Nanometer-scale carbon electrodes have also been used to measure neurotransmitter efflux from a neuromuscular junction[10] and for intracellular measurements of vesicle content.[11]

While amperometric techniques have contributed significantly to our understanding of the biophysics of neurotransmitter release, such as the relationship between neurotransmitter content and vesicle size,[12,13] how membrane dynamics constrain the rate of neurotransmitter release,[14,15] and different vesicle fusion modes,[16,17] several challenges remain in exocytosis research. First, diffusional broadening dramatically reduces signal-to-noise ratio (SNR),[18] which has a strong negative effect on measurements of

synaptic vesicles (due to their small quantal size)[4,5] or array experiments, where several electrodes monitor a single cell or a group of cells.[19,20] Second, CFE sensitivity has been increasingly scrutinized in the fast-scan cyclic voltammetry (FSCV) community,[21,22] where low limits-of-detection are critical for accurate measurements of the concentration of dopamine and other analytes. Faster electron-transfer kinetics are desirable to increase SNR in these *in vivo* measurements as well as for *in vitro* measurements at neurons. Third, and more importantly, any electrode fabrication or modification that addresses the first two issues would need to be applicable to nanometric probes to have a broader impact given recent developments in single-cell research.[10,11] For these reasons, we were interested in developing a facile electrode modification that improves electron-transfer (which could concomitantly increase SNR via faster catecholamine oxidation) and be applied to existing frameworks for exocytosis detection.

The neurochemistry community has explored different electrode materials[23-25] and modification schemes on CFEs using various nanomaterials, such as carbon nanotubes.[26-28] graphene,[29,30] carbon nanohorns,[31] and metal nanoparticles.[32] It is well recognized that gold (Au) has improved sensing capabilities compared to CFEs, likely because of the higher availability of oxide groups relative to carbon,[33] which are thought to facilitate the oxidation of catecholamines. Despite this, only a few examples exist in the literature of Au microelectrodes for catecholamine detection.[33,34] Notably, our group previously demonstrated that modification of CFEs with Au nanoparticles could improve temporal characteristics of catecholamine detection,[32] but the fabrication process was not tractable for other electrode scaffolds.

In this study, we endeavored to develop a fast, sensitive electrochemical sensor for measuring catecholamine release. We found that electrodeposition of gold onto CFE surfaces could be well-controlled, generating a reproducible layer of gold nanoparticles that significantly changed the electron transfer for dopamine. We then applied Au-CFEs to the measurement of catecholamine release from rat PC12 cells, a well-established model neuronal cell line.[35] We observed a significant increase in the average amount of catecholamine released and the phenomenon appears to be material-dependent. To test the generalizability of the probe, we augmented the catecholamine content of PC12 cells using L-DOPA, a

precursor to dopamine, and found that Au-CFEs detected a similar relative change in neurotransmitter release. A mechanism for this behavior is explored and implications in exocytosis research discussed.

3.2 EXPERIMENTAL

3.2.1 Chemicals and Materials

Sodium chloride (NaCl), potassium chloride (KCl), magnesium chloride hexahydrate ($MgCl_2 \cdot 6H_2O$), calcium chloride ($CaCl_2$), HEPES (4-(2-hydroxyethyl)-1-piperazineethanesulfonic acid), glucose, dopamine hydrochloride, phosphate-buffered saline (PBS, 10×), and L-3,4-dihydroxyphenylalanine (L-DOPA) were purchased from Sigma. $HAuCl_4$ was purchased as a 1% $AuCl_3$ solution from Salt Lake Metals. All reagents used were reagent grade or better.

3.2.2 Cell Culture

Stock PC12 cells were generously provided by Prof. Andrew Ewing (University of Gothenburg) and maintained as described previously.[14] Briefly, PC12 cells were grown on mouse collagen IV-coated culture dishes (VWR Scientific) in supplemented RPMI-1640 medium. Cells were maintained in a 7% CO_2, 37°C atmosphere and subcultured approximately every 7-9 days or when confluency was reached. Cells were used for experiments between days 5 and 12 of subculturing.

3.2.3 Carbon-Fiber Microelectrode Preparation

CFEs were prepared by aspirating a carbon-fiber (5 µm) into a borosilicate glass capillary (1.2 mm O.D., 0.9 mm I.D., Sutter) that was pulled to a fine tip using a micropipette puller (Sutter). The microelectrode was cut and sealed in epoxy (Epoxy Technologies), followed by curing for 2 hours at 80°C and 2 hours at 150°C. CFEs were then polished at a 45° angle on a homebuilt micropipette beveler. CFEs were backfilled with 3 M KCl to establish electrical contact.

3.2.4 Electrodeposition and Characterization

CFEs were characterized with cyclic voltammetry (CV) (-0.4 to +0.6 V, 100 mV/s, vs Ag/AgCl) in 0.1 mM dopamine solution (1x PBS, pH 7.4). Only electrodes with good electron-transfer kinetics and

stable *i*-V curves were used subsequently. For electrodeposition, CFEs were immersed in freshly sonicated 10 mM $HAuCl_4$, 0.5 M H_2SO_4 and subjected to the waveform specified in **Figure 1A** for 1500 cycles. Briefly, $E_{deposit}$ (vs Ag/AgCl) was held for 0.1 s before stepping to E_{rest} = +0.2 V for 0.1 s to allow $AuCl_4^-$ ions to diffuse back to the electrode surface. Au-CFEs were characterized by CV in 0.5 M H_2SO_4 (-0.2 to +1.2 V, 100 mV/s, vs Ag/AgCl). Only Au-CFEs with a gold oxide reduction peak were characterized again in 0.1 mM dopamine and used for experiments.

3.2.5 Single-Cell Amperometry

PC12 cells were bathed in pre-warmed 37 °C isotonic saline (150 mM NaCl, 5 mM KCl, 1.2 mM $MgCl_2 \cdot 6H_2O$, 2 mM $CaCl_2$, 5 mM glucose, and 10 mM HEPES, pH 7.4) for all experiments. Exocytosis from PC12 cells was measured by gently lowering CFEs or Au-CFEs onto a cell-of-interest using a hydraulic micropositioner (MHW-3, Narishige). For CFEs, E_{app} = +0.7 V vs Ag/AgCl, while for Au-CFEs, E_{app} was stepped in 50 mV increments to assess the baseline current – we often observed a large increase in the baseline current prior to +0.7 V vs Ag/AgCl which we attributed to oxidation of Au in the presence of chloride.[23] To avoid any change in the electrode surface, only potentials at which the baseline current was stable were used (E_{app}= +0.4-0.7 V).

Cells were stimulated to exocytose using a 20 p.s.i., 5 s pulse (FemtoJet; Eppendorf) of physiological saline with 100 mM K^+ (iso-osmotically substituted with NaCl) as described previously.[Error! Bookmark not defined.] Stimulation pipettes were cut to a diameter of about 10 µm and positioned 30-50 µm from a cell. Each cell was stimulated once. Experiments were maintained at 37 ± 1 °C (Warner Instruments). For L-DOPA experiments, cells were pre-incubated with 100 µM L-DOPA in isotonic saline for one hour.

3.2.6 Data Acquisition and Analysis

Electrodes were held at E_{app} vs. Ag/AgCl using a commercial patch-clamp current amplifier (Axopatch 200B; Axon Instruments). The current was filtered at 2 kHz using an internal low-pass Bessel filter and sampled at 100 kHz using a Digidata 1322 digitizer (Axon Instruments). Exocytotic spikes and their characteristics, including the spike characteristics i_{max} (peak amplitude, pA), $t_{1/2}$ (full-width of peak at

half-maximum, ms), t_{rise} (10-90% max peak height, ms), t_{fall} (90-10% max peak heigh, ms), and Q (integrated charge, fC) were identified using pClamp v10.6 software (Axon Instruments). Spikes were identified if the i_{max} exceeded 5 × S.D. of the noise. All identified spikes were inspected, and unfit spikes were manually discarded (such as double or superimposed spikes).

Statistics were calculated by taking the mean of the median value from each cell measured.[11] Statistical significance was assessed using the Mann-Whitney-Wilcoxon Rank-Sum U-Test (Mann-Whitney). The Kolmogorov-Smirnov test (KS-test) was used to assess the differences in distributions. Statistics are reported as the mean ± S.E.M.

3.3 Results and Discussion

3.3.1 Electrodeposition of Au onto CFEs

CFEs were prepared and beveled to 45° to provide a smooth surface onto which Au was deposited using pulsed electrodeposition. Pulsed electrodeposition of metals has previously been shown to greatly enhance control over the morphology and quality of the electrochemically deposited metal layer.[36] Compared with electrodeposition under a constant DC potential, pulsed deposition allows generation of more homogeneously distributed nucleation sites on the surface of the electrode. These nucleation sites also grow more evenly, as the metal salt near the electrode surface is consumed during the deposition period and replenished during the resting period.

Figure 3.1A shows the electrodeposition process. By alternating the potential between E_{rest} = +0.2 V and $E_{deposit}$ = -0.4 V at 100 ms intervals for 1500 cycles (total time $E_{deposit}$ = 150 s), we found that we could achieve a reproducible metal layer consisting of many individual Au nanoparticles on beveled CFEs. **Figure 3.1B** shows an SEM image of a Au-modified CFE (Au-CFE) fabricated at $E_{deposit}$ = -0.4V (for higher magnification, see **Figure S3.1**); many Au nanoclusters have grown on the CFE after deposition, increasing the surface area. The density and morphology of the deposited Au nanocluster layer depend on the $E_{deposit}$ as the rate of Au reduction onto the surface increases at more cathodic potentials. This resulted in surface

layers ranging from a few scattered Au nanoclusters ($E_{deposit}$ = -0.3 V) to overgrowth with Au nanoclusters ($E_{deposit}$ = -0.6 V) (data not shown).

3.3.2 Electrochemical Characterization

We assessed the electrochemical performance of our Au-CFEs by recording cyclic voltammograms (CVs) in 0.1 mM dopamine solution (*Experimental*). **Figure 3.2A** shows representative CVs (for additional examples, see **Figure S3.2A-D**), where Au-CFEs fabricated at different $E_{deposit}$ are compared to an unmodified CFE. The most striking consequence of the Au-modification is a shift in the position of the oxidation wave of dopamine, which can be quantified by examining the $E_{1/2}$. $E_{1/2}$ is the value of the potential at 50% the steady-state current, i_{ss}. In conventional two-electrode systems, $E_{1/2}$ is closely related to the formal potential, $E°$, of the redox reaction, while in bipolar electrochemical cells, such as the electrolyte-filled CFE used in this work, $E_{1/2}$ is closely related to the difference of the two formal potentials of the redox reactions in and outside of the bipolar CFE.[37]

The shifts in the $E_{1/2}$ are summarized in **Figure 3.2C**. To our surprise, the $E_{1/2}$ was always observed to shift negatively after Au deposition, even in the -0.3 V case where the gold layer was restricted to a few clusters of nanoparticles scattered across the surface of the CFE. To understand this, we compared the oxidation of dopamine on a solid Au UME with a directly-connected CFE and observed a negative shift in the oxidation wave of dopamine ~40 mV (data not shown). Thus, we posit that dopamine is likely oxidized preferentially on the gold surfaces, shifting the oxidation wave cathodically even at low surface densities. Though dopamine oxidation has an $E°' = +0.11$ V vs. SCE,[38] one may notice that the $E_{1/2}$ for our unmodified CFEs averages ~ +0.16 V (**Figure 3.2C**, for exact $E_{1/2}$ values, see **Table S3.1**). This is due to the bipolar nature of our CFEs; our group has previously shown that electrolyte back-filled CFEs function as closed bipolar electrodes where an oxidation reaction on the outer pole (dopamine oxidation) must be coupled to a reduction reaction on the inner pole, which in this case is likely to be O_2 reduction.[39] The bipolar nature of our electrodes also had the effect of slowing the rate of the Au deposition and altering the peak position of the gold oxide reduction peaks in subsequent scans in H_2SO_4 (**Figure 3.2B**).

We observed qualitatively that that Au-modification resulted in a faster rise time to i_{ss} in dopamine solution (**Figure 3.2A**). This was directly quantified following the procedures proposed by Mirkin and Bard by finding the $\Delta E_{1/4} = E_{1/4} - E_{1/2}$ and $\Delta E_{3/4} = E_{3/4} - E_{1/2}$ values, where $E_{1/4}$ and $E_{3/4}$ are the potentials at ¼ and ¾ of the steady-state limiting current $i_{ss,}$ respectively.[40] **Table 3.1** shows the shift in the magnitude of the $\Delta E_{1/4}$ and $\Delta E_{3/4}$. At almost all $E_{deposit}$ potentials, $\Delta E_{1/4}$ and $\Delta E_{3/4}$ changed significantly compared to CFEs ($p<0.05$, paired Mann-Whitney). Dopamine is an inner-sphere redox molecule, meaning its oxidation is limited by adsorption to an available electron-transfer site (surface oxide groups).[38] Given the higher availability of oxides on Au[33] and the many possible angles of approach afforded by nanoclusters, we suspect adsorption/desorption is accelerated at Au-CFEs, leading to faster electron transfer and smaller observed $\Delta E_{1/4}$ and $\Delta E_{3/4}$.

The presence and quantity of Au was determined by recording CVs in 0.5 M H_2SO_4 at 100 mV/s (**Figure 3.2B**, for additional CVs, see **Figure S3.3A-D**). The charge under the gold oxide reduction peak was integrated and converted to electrochemical surface area (ECSA) via the value 390 μC cm^{-2}, which has been suggested as a factor to convert the total charge of gold oxide reduction to surface area.[41] The roughness factor, ρ, could then be calculated by dividing the ECSA by the geometric area of the electrode (27.7 μm^2 for a 5 μm CFE beveled at 45°). Varying the $E_{deposit}$ potential changed the amount of Au deposited, thereby controlling the surface roughness of the resulting electrode (**Figure 3.2D**). **Table 3.1** shows the exact values obtained for the ECSA and ρ. Examining **Figure 3.2B**, one will notice a small reduction process occurring after the main gold oxide reduction peak (most prominently, $E_{deposit}$ = -0.6 V). Given that the process became both more pronounced and common for more negative deposition potentials and our reference electrode for deposition was Ag/AgCl, we expect that this is related to deposition of Ag^+ from solution onto the electrode surface.

3.3.3 Au-CFEs Are More Sensitive to Catecholamine Release from PC12 Cells

Having characterized the electrochemical performance of Au-CFEs, we applied them to PC12 cells to assess their quality for the measurement of catecholamine release. In **Figure 3.3**, one can see a few

example amperometric traces recorded from electrodes of various $E_{deposit}$ potentials (for additional amperometric traces, see **Figure S3.4**). **Table 3.2** shows that the peak current, i_{max}, has increased significantly for $E_{deposit}$ = -0.4 V Au-CFEs. However, we expected to see a concomitant decrease in some of the temporal characteristics of the peaks detected, consistent with our previous study;[32] rather, we observed that the average $t_{1/2}$, t_{rise}, and t_{fall} characteristics were similar between control and all Au-CFEs.

Integration of the peak charge, Q, allows quantification of the number of molecules released ($N_{molecules}$) via Faraday's law, $Q = nFN$, where F = 96485 C mol^{-1} is the Faraday's constant, N is Avogadro's number and n = 2 is the number of electrons transferred per dopamine molecule. The $N_{molecules}$ detected reached a maximum of 103,400 ± 5,800 molecules with Au-CFEs fabricated at $E_{deposit}$ = -0.4 V, which was significantly different ($p<0.0001$, Mann-Whitney) than that detected on control CFEs (61,800 ± 4,100 molecules). Our control value is a bit lower when compared to the literature,**Error! Bookmark not defined.** but we f ound it to be very reproducible. We expect this disparity may be explained by subtle differences in cell culture conditions. **Figure 3.4A** shows the cumulative distribution of $N_{molecules}$ collected from each electrode sample, which allows use of the KS-test to determine whether two samples came from the same population. Interestingly, $E_{deposit}$ = -0.3 V showed no significant difference from control CFEs, suggesting that a few scattered Au nanoparticles on the CFE surface is enough to change dopamine CV in bulk solution but cannot alter exocytosis detection from a cell. However, $E_{deposit}$ = -0.4, -0.5, -0.6 V were all significantly different from control CFEs ($p<0.0001$, KS-test) suggesting that a thin layer of Au that fully covers the electrode surface fundamentally alters the detection. **Figure 3.4B** shows the frequency-normalized distribution of $N_{molecules}$ and **Figure 3.4C** shows the frequency-normalized distribution of $N_{molecules}^{1/3}$, which may be fit by a Gaussian, consistent with the literature.[35]

For $E_{deposit}$ = -0.4 V probes, we achieved consistently improved detection of exocytosis, though this effect was not shared by all probes. Despite their similar cumulative distributions, the average i_{max} and $N_{molecules}$ for $E_{deposit}$ = -0.5, -0.6 V were not significantly different from control, in contrast to E = -0.4V (**Table 3.2**). The quality of the gold layer likely suffers at more negative deposition potentials, where overgrowth of the electrode surface is common due to the development of voids within the gold layer.

3.3.4 Mechanism for Improved Performance of Au-CFEs

Given the considerable improvement in signal-to-noise on the $E_{deposit}$ = -0.4 V probes, we explored a few possible mechanisms for the behavior. To determine whether the behavior was facilitated by a better electrode material alone (e.g. noble metal), we repeated the experiment with Pt-modified CFEs on an independent cell culture (amperometric traces, **Figure S3.5**). Pt has similar electron-transfer properties to Au, but we found no significant difference between the distributions of $N_{molecules}$ of bare CFEs and Pt-CFEs (KS-test; **Figure S3.6**, statistics, **Table S3.2**).

Next, we considered the possibility that the Au-CFEs either detected fewer events (biasing statistics towards higher values) or altered detection through an interaction with the cell. However, examining the total number of events per cell and the interspike interval (interval between events), we found no significant differences between Au-CFEs and bare CFEs (**Figure S3.7**, **S3.8**), except for $E_{deposit}$ = -0.4 V which detected fewer events on average than control ($p < 0.05$) in untreated cells.

Finally, we considered that our increased detection on Au-CFEs could be due to the detection of intracellular vesicles by cell penetration and vesicle impact electrochemical cytometry (VIEC). VIEC has been shown to result in increased catecholamine detection due to more complete oxidation of the vesicle contents,[6,7,11] which suggests that most vesicles release only a fraction of their neurotransmitter content.[17] Detection via VIEC does not require stimulation of the cell; therefore, we performed cell experiments with each probe in Ca^{2+}-free solution (**Figure S3.9**). No events were detected on any probe (n = 3 probes, 10-12 cells each condition). Thus, the detection results very likely to be from stimulated exocytosis alone, without any biasing from intracellular vesicle detection.

The presence of Au (rather than Pt) apparently plays a significant role in the improvements to catecholamine detection without altering exocytosis detection in other ways. The high availability of surface oxides on Au compared to bare CFEs[33] likely increases coulometric efficiency when detecting exocytosis. A previous study showed that Au-coated electrodes detected greater catecholamine release from chromaffin cells when compared to ITO electrodes,[42] consistent with our results. Au-CFEs may also penetrate the extracellular matrix (ECM) of proteoglycans surrounding the cell, allowing more complete

detection of released neurotransmitter. Previously, the Ewing group showed partial digestion of the ECM yielded greater catecholamine detection,[43] though the relative increase was less than observed here.

3.3.5 Au-CFEs Demonstrate Similar Sensitivity When Measuring Augmented Vesicle Content

We have shown that Au-CFEs have characteristics that make them attractive for the detection of catecholamine release. To assess the generalizability of the probe, we introduced a perturbation to the PC12 cell measurement by pre-incubating the cells with 100 µM L-DOPA, which augments the catecholamine content of the vesicles.[13] Since $E_{deposit}$ = -0.4 V probes had the best sensitivity to released catecholamine in previous experiments, we used this probe for comparison. Interestingly, we detected a similar increase in the average $N_{molecules}$ when using the Au-CFE. The $N_{molecules}$ distributions and sample amperometric traces may be seen in **Figure 3.5**. The difference between the cumulative distributions of $N_{molecules}$ was significant (KS-test, $p<0.0001$), consistent with our previous experiments. The spike parameters are tabulated in **Table S3.3**, where one can see that the change in i_{max} is also conserved. There were no significant differences in the average number of events observed per cell or the interspike interval when comparing Au-CFEs to control CFEs (**Figure S3.7**), supporting our conclusion that Au-CFEs are not altering exocytosis or detecting fewer events.

3.4 CONCLUSIONS

In summary, we developed CFEs with a thin layer of electrochemically-deposited Au nanoparticles that allowed more sensitive measurement of released catecholamine from PC12 cells. Au-CFEs demonstrated improved electron-transfer kinetics and catalyzed the oxidation of dopamine at more negative potentials. The morphology and roughness of the deposited gold-layer could be controlled by varying the $E_{deposit}$ potential; we found that the presence of gold, even without full surface coverage, was sufficient to shift the $E_{1/2}$ and improve electron transfer for dopamine oxidation. Our results suggest that the high surface area and morphology of the Au-CFEs improved detection of catecholamine. The methodology employed here may find applications in improving electrode array sensitivity, nanoelectrode surface area and

sensitivity, or even FSCV applications to improve electron-transfer kinetics or anchor new chemical-sensing modalities.

3.5 TABLES, SCHEMES, AND FIGURES

Edeposit (V)	*n*	ECSA (μm2)	*ρ*	$\Delta E_{1/2}$ (mV)	$\Delta E_{1/4}$ (mV)	$\Delta E_{3/4}$ (mV)
Bare CFE	14	-	-	-	277 ± 11a	219 ± 9a
-0.3	10	55.0 ± 14.1	1.98 ± 0.51	-80 ± 18	193 ± 10**	155 ± 14**
-0.4	14	94.4 ± 14.8	3.41 ± 0.53	-74 ± 15	207 ± 6**	132 ± 17**
-0.5	12	101.1 ± 23.0	3.65 ± 0.83	-105 ± 19	175 ± 14**	147 ± 20*
-0.6	10	133.0 ± 28.9	4.80 ± 1.04	-79 ± 27	170 ± 12**	144 ± 12

Table 3.1. Electrode characteristics determined by CV analysis. ECSA and ρ are from CVs in H_2SO_4 solution and $\Delta E_{1/2}$, $\Delta E_{1/4}$, $\Delta E_{3/4}$ are from CVs in dopamine solution. Significance of kinetic enhancement was assessed using Paired Mann-Whitney test. **p<0.01, *p<0.05. [a]Bare CFE kinetic data corresponds to unmodified electrodes from the -0.4 V group.

Probe	Events	i_{max} (pA)	$t_{1/2}$ (ms)	t_{rise} (ms)	t_{fall} (ms)	$N_{molecules}$ (10^3)
CFE	957	14.0 ± 1.5	0.88 ± 0.06	1.39 ± 0.57	1.22 ± 0.10	61.8 ± 4.1
Au (-0.3V)	575	16.0 ± 1.9	0.85 ± 0.08	0.81 ± 0.07	1.16 ± 0.14	64.0 ± 4.2
Au (-0.4V)	516	22.6 ± 1.8†	1.05 ± 0.10	0.87 ± 0.07	1.36 ± 0.10	103.4 ± 5.8‡
Au (-0.5V)	406	14.1 ± 1.3	1.25 ± 0.14	0.84 ± 0.09	1.54 ± 0.23	77.2 ± 12.5
Au (-0.6V)	536	17.5 ± 1.5	0.99 ± 0.07	0.93 ± 0.06	1.44 ± 0.15	92 ± 9.9*

Table 3.2. Spike characteristics under different probe conditions. Exocytosis events were measured for a variety of characteristics using probes fabricated under different conditions. p values were determined using Mann-Whitney Rank-Sum U-Test. Each probe was compared with bare CFE to determine significance. *=p<0.05, **=p<0.01, †=p<0.001, ‡=p<0.0001.

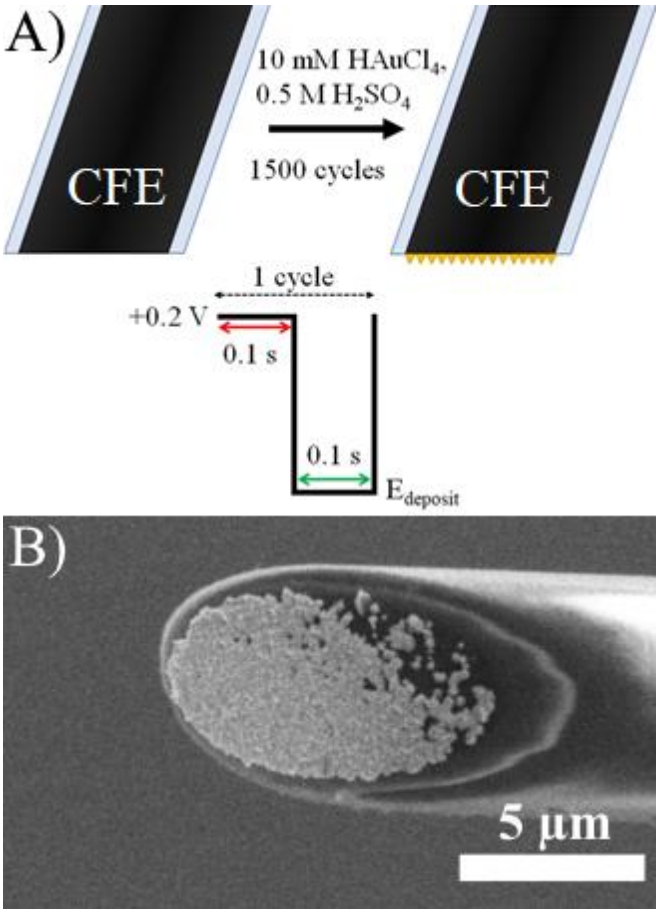

Figure 3.1. Fabrication of Au-CFEs. A) Fabrication scheme for Au-CFEs using pulsed electrodeposition. B) SEM image of an Au-CFE fabricated at $E_{deposit}$ = -0.4 V. Higher magnification, **Figure S3.1**.

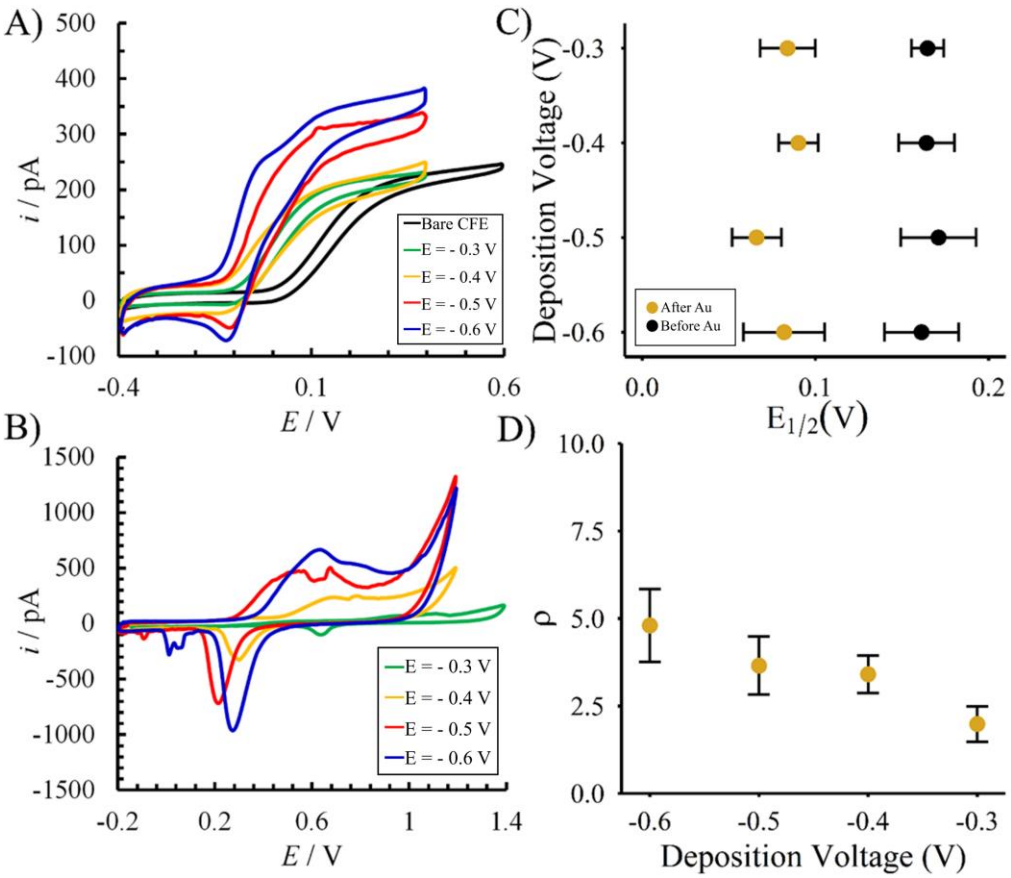

Figure 3.2. Electrochemical characterization of Au-CFEs. A) Representative CVs in 0.1 mM dopamine of Au-CFEs fabricated at different $E_{deposit}$ potentials. As more Au is deposited, the i_{ss} increases. B) CVs in 0.5 M H_2SO_4 of the same electrodes as in A. As more Au is deposited, the gold oxide reduction peak becomes larger. C) $E_{1/2}$ shifts for dopamine oxidation as a function of deposition voltage. D) Surface roughness (ρ) as a function of deposition voltage.

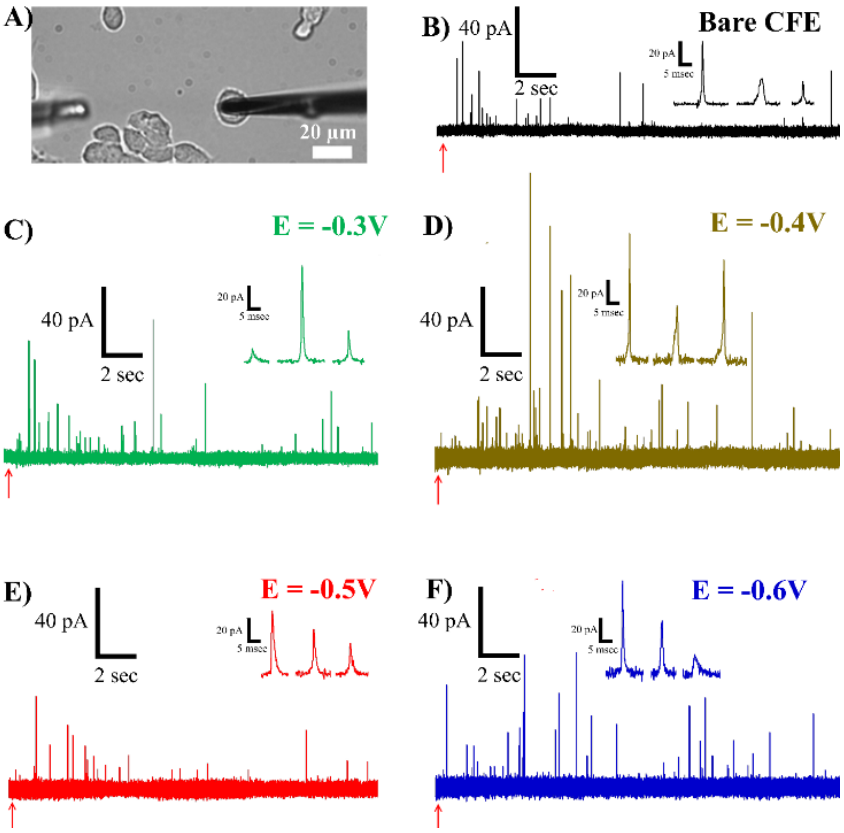

Figure 3.3. Single-cell amperometry at PC12 cells. A) Optical microscope picture of the experiment. The CFE (right) is lowered onto a PC12 cell and stimulated to release using the stimulation pipette (left, out of focus). Scale bar is 20 µm. B-F) Example amperometric response using different probes. Stimulation with 100 mM K^+ is indicated with the red arrows. Inset shows three peaks from each trace.

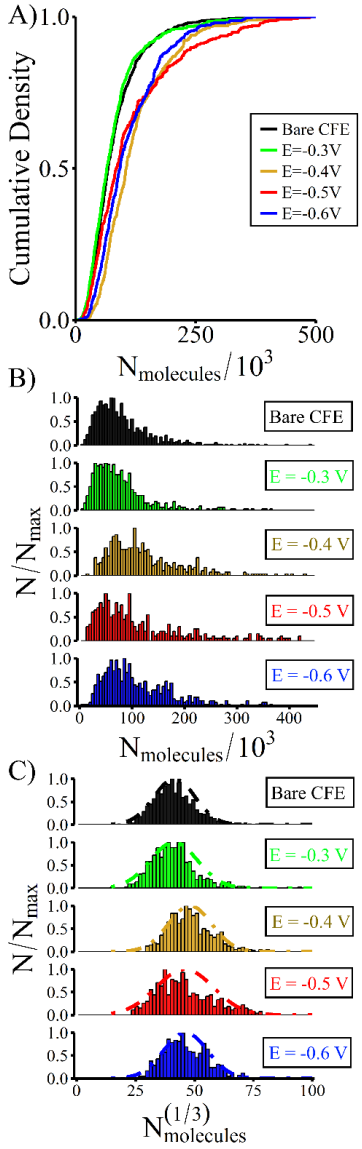

Figure 3.4. Au-CFEs demonstrate improved detection of catecholamine release from PC12 cells. A) Cumulative distributions of release events show a significant difference between Bare CFEs and Au-CFEs modified with $E_{deposit}$ =-0.4V‡, -0.5V‡, and -0.6V‡ (KS-test, ‡ = $p < 0.0001$). B) Normalized frequency histogram of molecules released and C) Normalized frequency distribution of the cube root of the number of molecules released. The cube root distribution may be fit with a Gaussian curve.

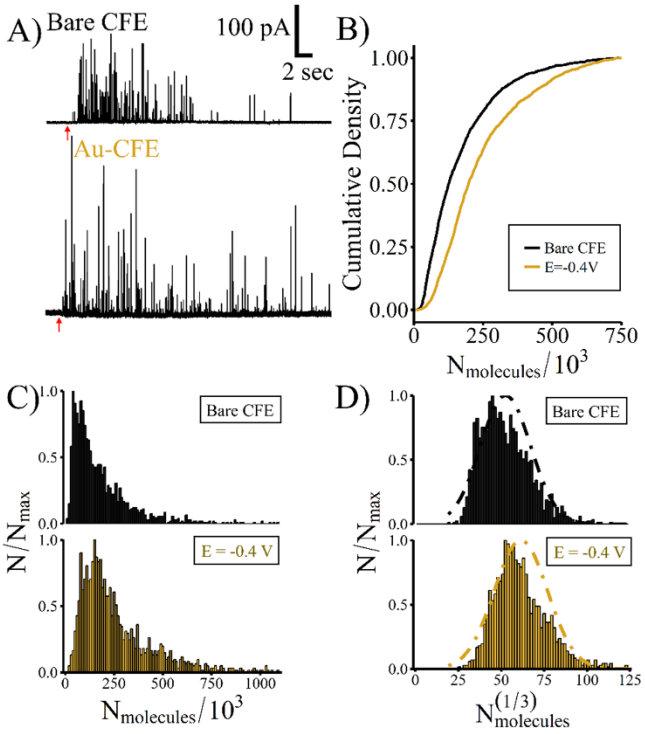

Figure 3.5. Au-CFEs detect more catecholamine release from L-DOPA-augmented PC12 cells. A) Example amperometric traces collected from Bare CFEs or Au-CFEs. The red arrow indicates stimulation with 100 mM K^+. B) Cumulative density distributions of the number of molecules released show $E_{deposit}$ = -0.4 V‡ is significantly different from Bare CFEs (KS-test, ‡ = $p < 0.0001$). C) Normalized frequency histograms of the number of molecules released. Insets show the normalized frequency histogram of the cube root of the number of molecules for each electrode type.

$E_{deposit}$ (V)	# Electrodes	$E_{1/2}$ before Au (mV)	$E_{1/2}$ after Au (mV)
-0.3	13	155±9.6	84.7±12.5
-0.4	14	159±15.8	90.1±11.3
-0.5	10	174±19.8	66.1±14.2
-0.6	10	157±19.9	81.9±19.9

Table S3.1. E1/2 values for oxidation of dopamine on the CFEs before and after gold deposition.

Electrode	Cells	# events	I_{max} (pA)	$t_{1/2}$ (ms)	t_{rise} (ms)	t_{fall} (ms)	$N_{molecules}/10^3$
CFE	7	869	16.7±2.7	1.03±0.1	0.78±0.08	1.81±0.21	95.9±12.9
Pt-CFE	7	599	18.7±3.0	0.83±0.08*	0.69±0.06	1.26±0.18**	76.1±9

Table S3.2. Spike Characteristics collected using Pt-CFEs on PC12 cells. * is $p<0.05$, ** is $p<0.01$.

Electrode	# Cells	Events	I_{max} (pA)	$t_{1/2}$ (ms)	t_{rise} (ms)	t_{fall} (ms)	$N_{molecules}/10^3$
Bare CFE	17	1768	11.7±1.1	1.79±0.11	1.30±0.07	3.04±0.27	135±10.2
Au (-0.4V)	13	1438	32.1±2.0****	1.69±0.21	1.36±0.16	2.73±0.43	199±19.2**

Table S3.3. Spike Characteristics collected from L-DOPA incubated PC12 cells. ** is $p<0.01$, **** is $p<0.0001$.

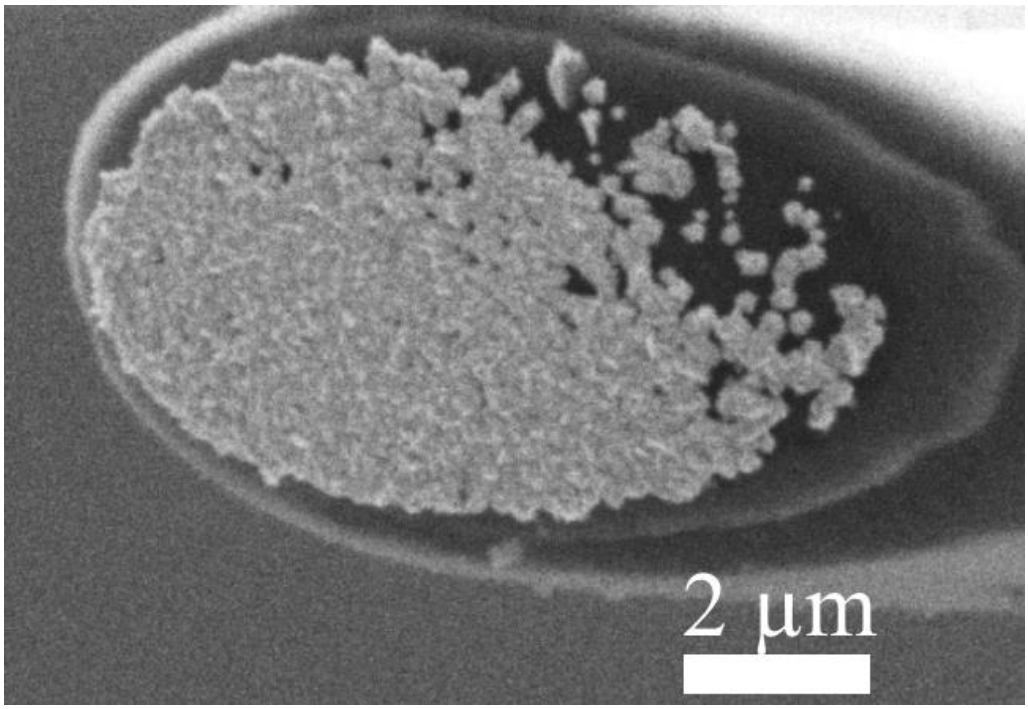

Figure S3.1. Zoomed in SEM image of the Au-CFE from Main-text, Figure 1B.

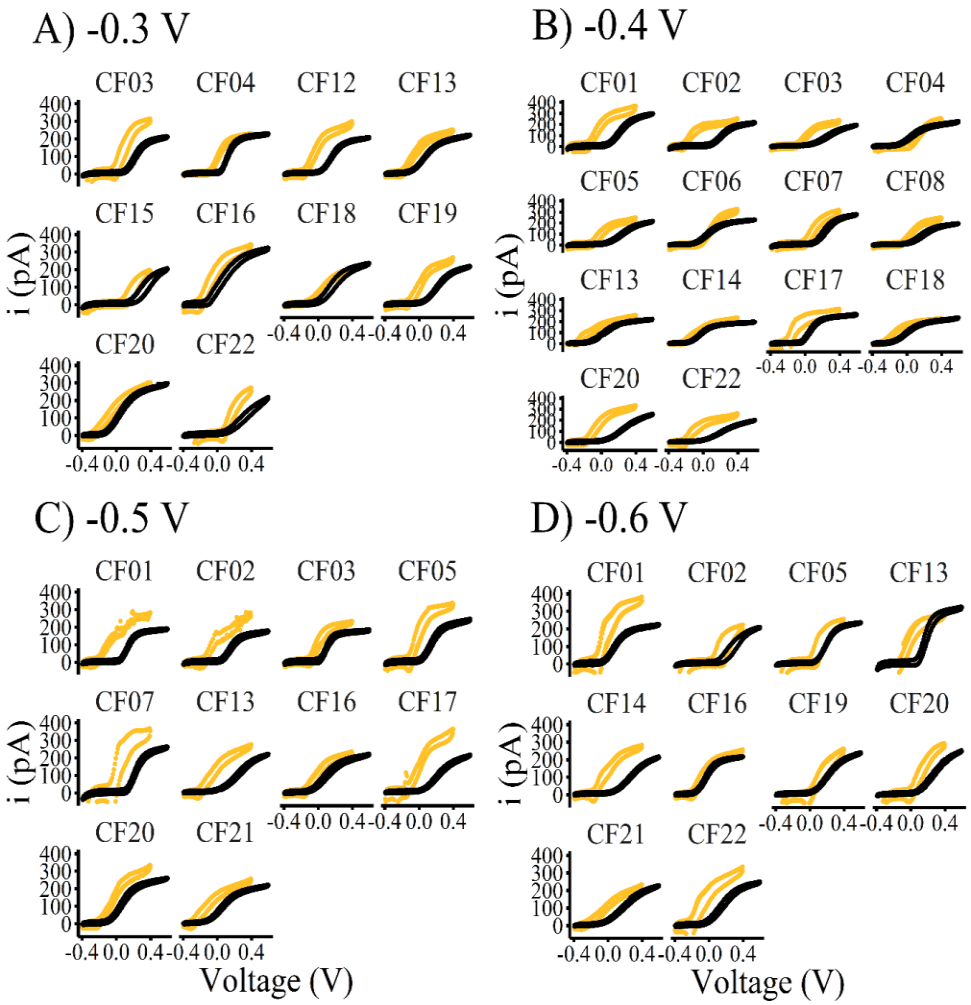

Figure S3.2. Cyclic voltammograms before/after deposition. Cyclic voltammetry of electrodes in 0.1 mM dopamine, 1x PBS before (black) and after (gold) Au deposition. A) $E_{deposit}$ = -0.3 V, B) -0.4 V, C) -0.5 V, D) -0.6 V.

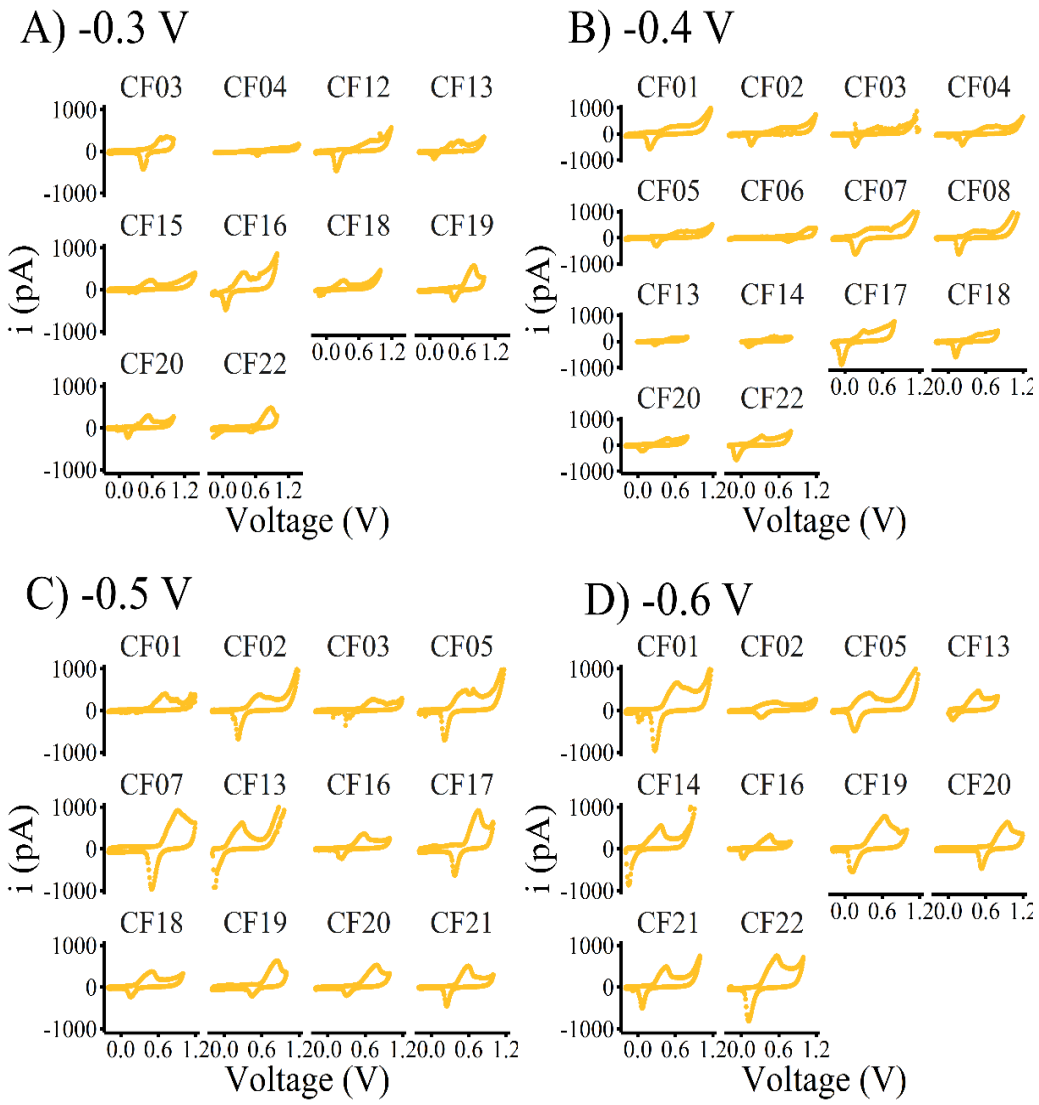

Figure S3.3. Cyclic voltammograms in 0.5 M H2SO4 after Au deposition. A) $E_{deposit}$ = -0.3 V, B) -0.4 V, C) -0.5 V, D) -0.6 V.

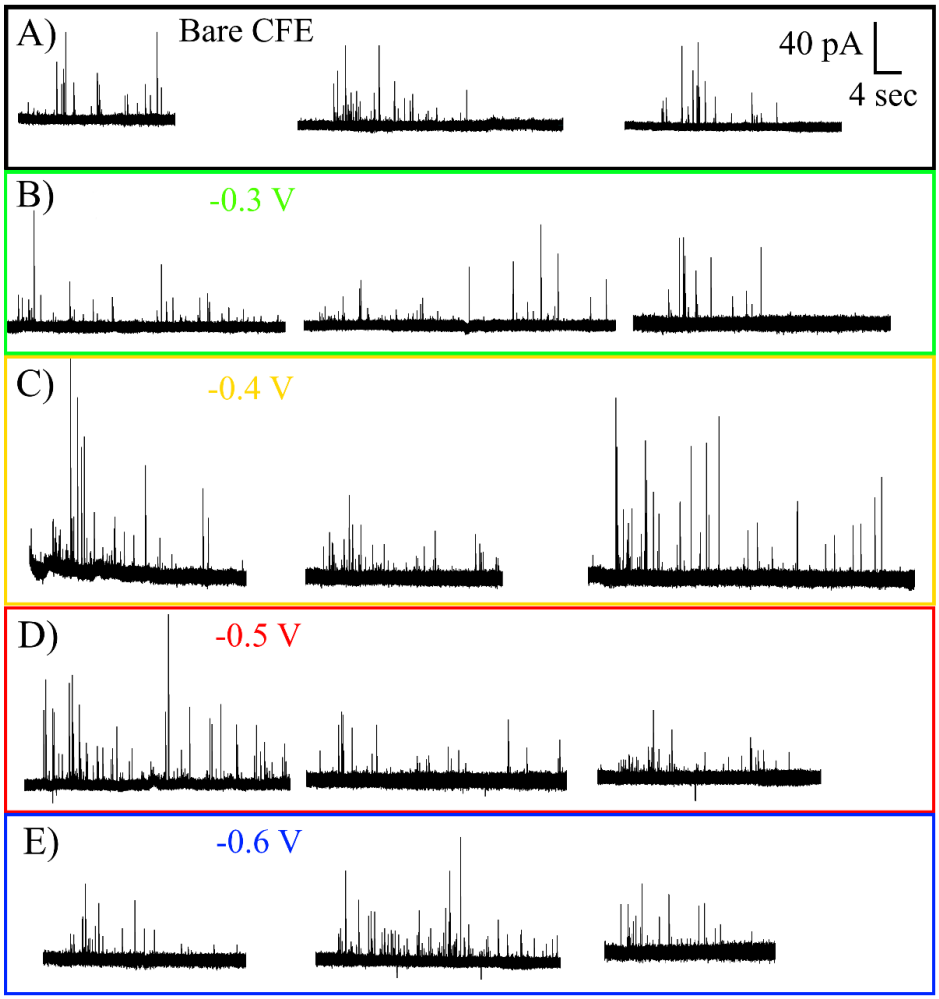

Figure S3.4. Additional amperometric traces at different $E_{deposit}$ conditions. A) Unmodified, bare CFEs, B) -0.3 V, C) -0.4 V, D) -0.5 V, and E) -0.6 V.

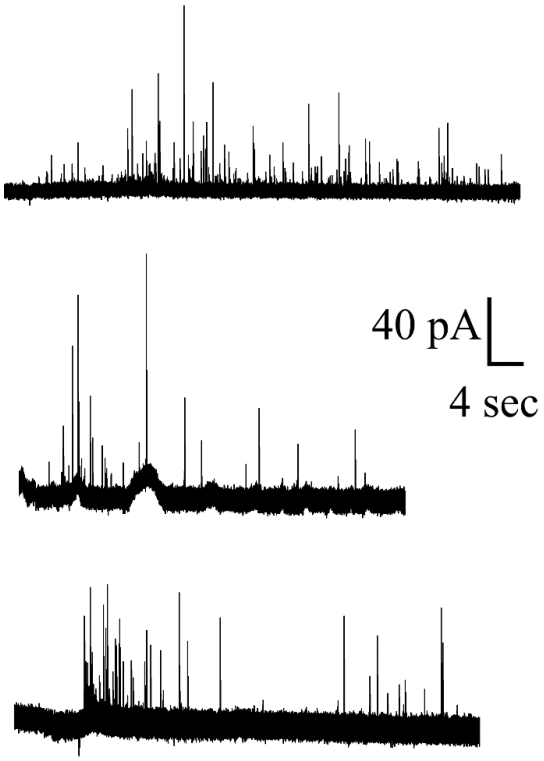

Figure S3.5. Example amperometric traces for Pt-CFEs on PC12 cells.

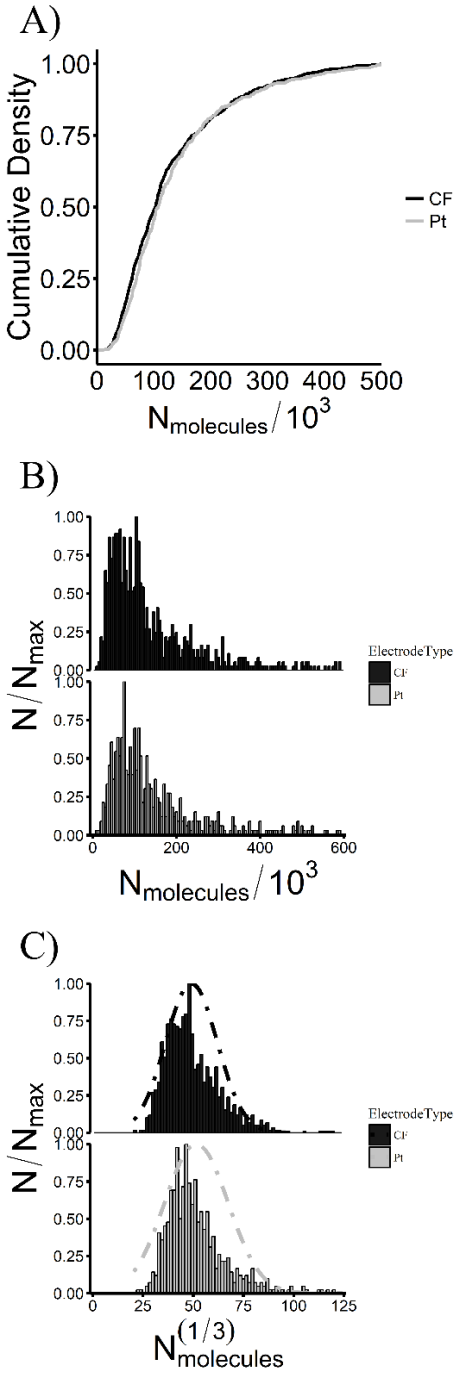

Figure S3.6. Pt-CFEs do not observe the same increased catecholamine release.
A) Cumulative distributions of number of molecules released show no difference (KS-test, $p>0.05$) in events detected with Bare CFEs vs Pt-CFEs. B) Normalized frequency histograms of number of molecules released. C) Normalized frequency histograms of the cube root of number of molecules released may be fit by a gaussian.

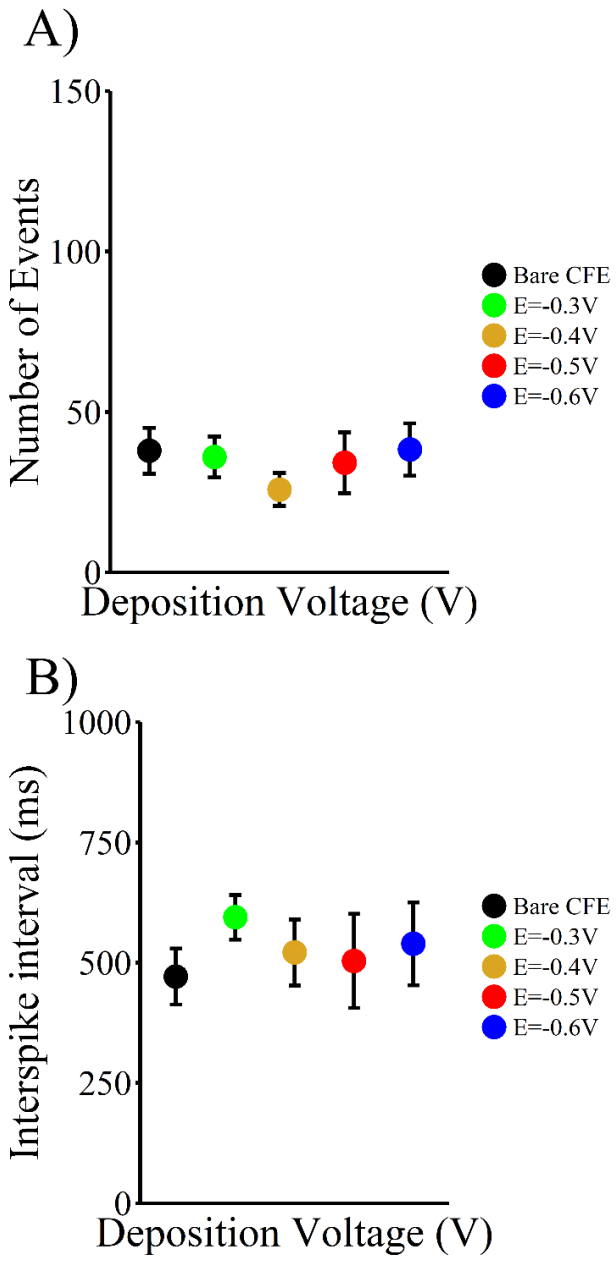

Figure S3.7. Addition of Au does not change bulk exocytosis properties. A) Average number of events recorded per cell with different probes. B) Average interspike interval (ms) for events recorded with different probes.

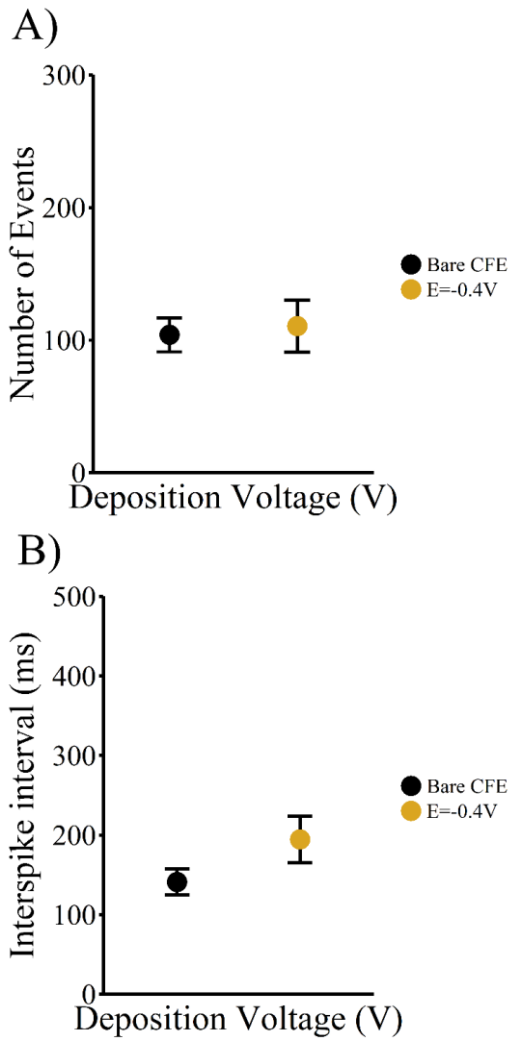

Figure S3.8. Addition of Au does not change observed bulk exocytosis properties in cells pre-treated with L-DOPA. A) Average number of events recorded per cell with different probes. B) Average interspike interval (ms) for events recorded with different probes.

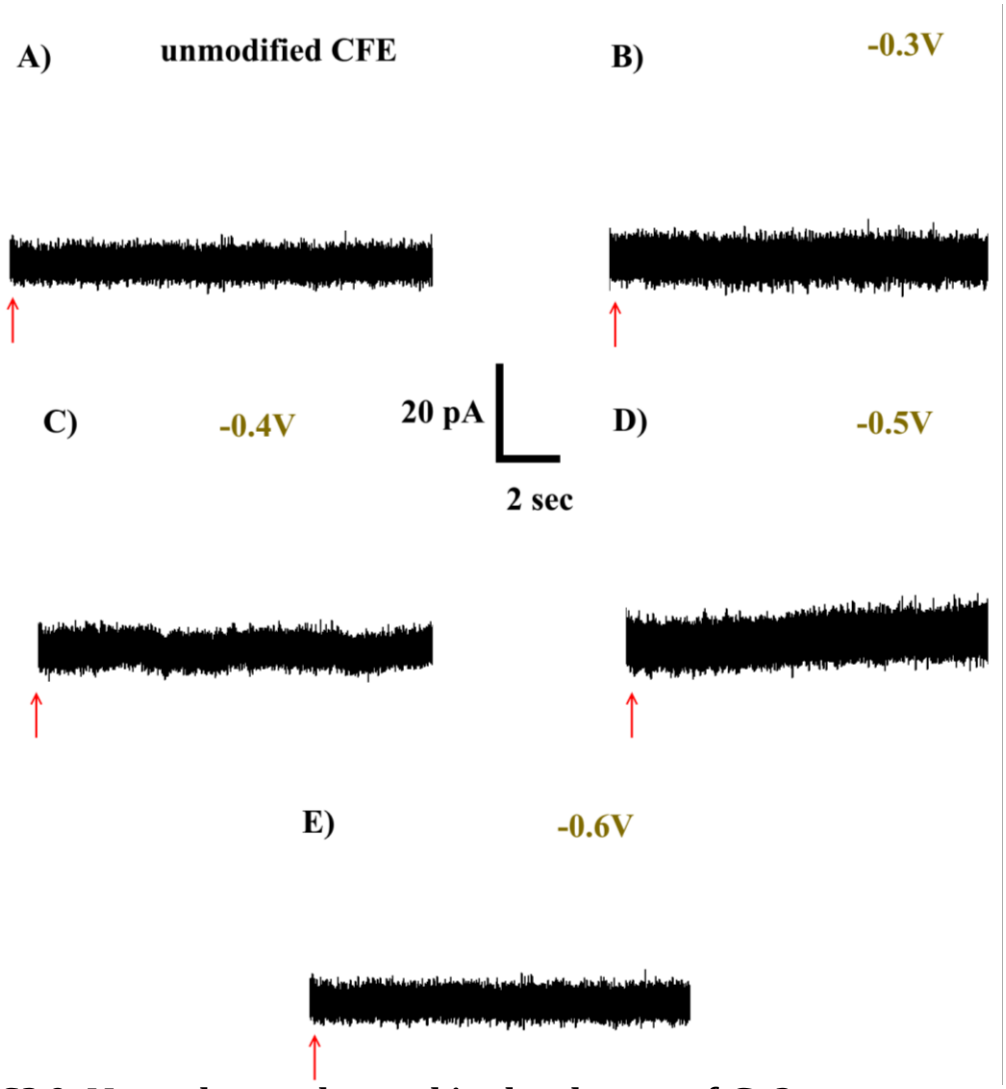

Figure S3.9. No peaks are detected in the absence of Ca2+. A) unmodified CFE, B) -0.3 V, C) -0.4 V, D) -0.5 V, and E) -0.6 V.

3.6 REFERENCES

(1) Robinson, D. L.; Hermans, A.; Seipel, A. T.; Wightman, R. M. "Monitoring Rapid Chemical Communication in the Brain." *Chem. Rev*. **2008**, *108*, 2554–2584.

(2) Mosharov, E. M.; Sulzer, D. "Analysis of exocytotic events recorded by amperometry." *Nature Methods* **2005**, *2*, 651–658.

(3) Ganesana, M.; Lee, S. T.; Wang, Y.; Venton, B. J. "Analytical Techniques in Neuroscience: Recent Advances in Imaging, Separation, and Electrochemical Methods." *Anal. Chem.* **2017**, *89*, 314–341.

(4) Staal, R. G. W.; Mosharov, E. V; Sulzer, D. "Dopamine neurons release transmitter via a flickering fusion pore." *Nat. Neurosci.* **2004**, *7*, 341–346.

(5) Pothos, E. N.; Davila, V.; Sulzer, D. "Presynaptic Recording of Quanta from Midbrain Dopamine Neurons and Modulation of the Quantal Size." *J. Neurosci*. **1998**, *18*, 4106–4118.

(6) Dunevall, J.; Fathali, H.; Najafinobar, N.; Lovric, J.; Wigström, J.; Cans, A. S.; Ewing, A. G. "Characterizing the Catecholamine Content of Single Mammalian Vesicles by Collision–Adsorption Events at an Electrode." *J. Am. Chem. Soc.* **2015**, *137*, 4344–4346.

(7) Li, X.; Dunevall, J.; Ren, L.; Ewing, A.G. "Mechanistic Aspects of Vesicle Opening during Analysis with Vesicle Impact Electrochemical Cytometry." *Anal. Chem.* **2017**, *89*, 9416–9423.

(8) Wightman, R. M.; Jankowski, J. A.; Kennedy, R. T.; Kawagoe, K. T.; Schroeder, T. J.; Leszczyszyn, D. J.; Near, J. A.; Diliberto, E. J.; Viveros, O. H. "Temporally resolved catecholamine spikes correspond to single vesicle release from individual chromaffin cells." *Proc. Natl. Acad. Sci. USA.* **1991**, *88*, 10754–10758.

(9) Zerby, S. E.; Ewing, A. G. "Electrochemical monitoring of individual exocytotic events from the varicosities of differentiated PC12 cells." *Brain Res.* **1996**, *712*, 1–10.

(10) Li, Y.; Zhang, S.; Wang, X.; Zhang, X.; Oleinick, A. I.; Svir, I.; Amatore, C.; Huang, W. "Real-time Monitoring of Discrete Synaptic Release Events and Excitatory Potentials within Self-reconstructed Neuromuscular Junctions." *Angew. Chem. Int. Ed.* **2015**, *54*, 9313–9318.

(11) Li, X.; Majdi, S.; Dunevall, J.; Fathali, H.; Ewing, A. G. “Quantitative Measurements of Transmitters in Vesicles One at a Time in Single Cell Cytoplasm with Nano-tip Electrodes.” *Angew. Chem. Int. Ed.* **2015**, *54*, 11978–11982.

(12) Sombers, L. A.; Hanchar, H. J.; Colliver T. L.; Wittenberg, N.; Cans, A.; Arbault, S.; Amatore, C.; Ewing, A. G. “The effects of vesicular volume on secretion through the fusion pore in exocytotic release from PC12 cells.” *J. Neurosci*. **2004**, *24*, 303–309.

(13) Colliver, T. L.; Pyott, S. J.; Achalabun, M.; Ewing, A. G. “VMAT-Mediated changes in quantal size and vesicular volume.” *J. Neurosci*. **2000**, *20*, 5276–5282.

(14) Sombers, L. A.; Wittenberg, N. J.; Maxson, M. M.; Adams, K. L.; Ewing, A. G. “High Osmolarity and L-DOPA Augment Release via the Fusion Pore in PC12 Cells.” *Chemphyschem* **2007**, *8*, 2471–2477.

(15) Oleinick, A.; Svir, I.; Amatore, C. “‘Full fusion’ is not ineluctable during vesicular exocytosis of neurotransmitters by endocrine cells.” *Proc. Math. Phys. Eng. Sci*. **2017**, *473*, 1–12.

(16) van Kempen, G. Th. H.; vanderLeest, H. T.; van den Berg, R. J.; Eilers, P.; Westerink, R. H. S. “Three Distinct Modes of Exocytosis Revealed by Amperometry in Neuroendocrine Cells.” *Biophys. J*. **2011**, *100*, 968–977.

(17) Ren, L.; Mellander, L.; Keighron, J.; Cans, A.; Kurczy, M.; Svir, I., Oleinick, A.; Amatore, C.; Ewing, A. G. “The evidence for open and closed exocytosis as the primary release mechanism.” *Quart. Rev. Biophys.* **2016**, *49*, E12.

(18) Schroeder, T. J.; Jankowski, J. A.; Kawagoe, K. T.; Wightman, R. M.; Lefrou, C.; Amatore, C. “Analysis of diffusional broadening of vesicular packets of catecholamines released from biological cells during exocytosis.” *Anal. Chem.* **1992**, *6*, 3077–3083.

(19) Zhang, B.; Adams, K. L.; Luber, S.; Heien, M., Ewing, A. G. “Spatially and Temporally Resolved Single-Cell Exocytosis Utilizing Individually Addressable Carbon Microelectrode Arrays.” *Anal. Chem.* **2008**, *80*, 1394–1400.

(20) Zhang, B.; Heien, M. L. A. V.; Santillo, M. F.; Mellander, L.; Ewing, A. G. “Temporal Resolution in Electrochemical Imaging on Single PC12 Cells Using Amperometry and Voltammetry at Microelectrode Arrays.” *Anal. Chem.* **2011**, *83*, 571–577.

(21) Yang, C.; Wang, Y.; Jacobs, C. B.; Ivanov, I.; Venton, B. J. “O2 plasma etching and antistatic gun surface modifications for CNT yarn microelectrode improve sensitivity and antifouling properties.” *Anal. Chem.* **2017**, *89*, 5605–5611.

(22) Yang, C.; Trikantzopoulos, E.; Jacobs, C. B.; Venton, B. J. “Evaluation of carbon nanotube fiber microelectrodes for neurotransmitter detection: Correlation of electrochemical performance and surface properties.” *Anal. Chim. Acta*. **2017**, *965*, 1–8.

(23) Jacobs, C. B.; Ivanov, I. N.; Nguyen, M. D.; Zestos, A. G.; Venton, B. J. “High temporal resolution measurements of dopamine with carbon nanotube yarn microelectrodes.” *Anal. Chem.* **2014**, *86*, 5721–5727.

(24) Larsen, S. T.; Vreeland, R. F.; Heien, M. L.; Taboryski, R. “Characterization of poly(3,4-ethylenedioxythiophene):tosylate conductive polymer microelectrodes for transmitter detection.” *Analyst* **2012**, *137*, 1831–1836.

(25) Schmidt, A. C.; Wang, X.; Zhu, Y.; Sombers, L. A. “Carbon nanotube yarn electrodes for enhanced detection of neurotransmitter dynamics in live brain tissue.” *ACS Nano* **2013**, *7*, 7864–7873.

(26) Chen, R. S.; Huang, W. H.; Tong, H.; Wang, Z. L.; Cheng, J. K. “Carbon Fiber Nanoelectrodes Modified by Single-Walled Carbon Nanotubes.” *Anal. Chem.* **2003**, *75*, 6341–6345.

(27) Zhang, M.; Liu, K.; Xiang, L.; Lin, Y.; Su, L.; Mao, L. “Carbon Nanotube-Modified Carbon Fiber Microelectrodes for In Vivo Voltammetric Measurement of Ascorbic Acid in Rat Brain.” *Anal. Chem.* **2007**, *79*, 6559–6565.

(28) Swamy, B. E.; Venton, B. J. “Carbon nanotube-modified microelectrodes for simultaneous detection of dopamine and serotonin *in vivo*.” *Analyst* **2007**, *132*, 876–884.

(29) Zhu, M.; Zeng, C.; Ye, J. “Graphene – Modified Carbon Fiber Microelectrode for the Detection of Dopamine in Mice Hippocampus Tissue.” *Electroanalysis* **2011**, *23*, 907–914.

(30) Bai, J.; Wang, X.; Meng, Y.; Zhang, H. M.; Qu, L. “Fabrication of Graphene Coated Carbon Fiber Microelectrode for Highly Sensitive Detection Application.” *Anal. Sci.* **2014**, *30*, 903–909.

(31) Puthongkham, P.; Venton, B. J. "Carbon Nanohorn – modified Carbon Fiber Microelectrodes for Dopamine Detection." *Electroanalysis* **2018**, *30*, 1073-1081.

(32) Adams, K. L.; Jena, B. K.; Percival, S. J.; Zhang, B. "Highly sensitive detection of exocytotic dopamine release using a gold-nanoparticle-network microelectrode." *Anal. Chem*. **2011**, *83*, 920–927.

(33) Zachek, M. K.; Hermans, A.; Wightman, R. M.; McCarty, G. S. "Electrochemical Dopamine Detection: Comparing Gold and Carbon Fiber Microelectrodes using Background Subtracted Fast Scan Cyclic Voltammetry*." J. Electroanal. Chem.* **2008**, *614*, 113–120.

(34) Wang, K.; Zhao, X.; Li, B.; Wang, K.; Zhang, X.; Mao, L.; Ewing, A.; Lin, Y. "Ultrasonic-Aided Fabrication of Nanostructured Au-Ring Microelectrodes for Monitoring Transmitters Released from Single Cells." *Anal. Chem.* **2017**, *89*, 8683–8688.

(35) Westerink, R. H. S.; Ewing, A. G. "The PC12 cell as model for neurosecretion." *Acta Phys.* **2008**, *192*, 273–285.

(36) Rothe, J.; Frey, O.; Madangopal, R.; Rickus, J.; Hierlemann, A. "Robust Functionalization of Large Microelectrode Arrays by Using Pulsed Potentiostatic Deposition." *Sensors* **2017**, *17*, 1–13.

(37) Cox, J. T.; Guerrette, J. P.; Zhang, B. "Steady-State Voltammetry of a Microelectrode in a Closed Bipolar Cell." *Anal. Chem.* **2012**, *84*, 8797–8804.

(38) Bath, B. D.; Michael, D. J.; Trafton, B. J.; Joseph, J. D.; Runnels, P. L.; Wightman, R. M. "Subsecond Adsorption and Desorption of Dopamine at Carbon-Fiber Microelectrodes." *Anal. Chem.* **2000**, *72*, 5994–6002.

(39) Guerrette, J. P.; Oja, S. M.; Zhang, B. "Coupled Electrochemical Reactions at Bipolar Microelectrodes and Nanoelectrodes." *Anal. Chem*. **2012**, *84*, 1609–1616.

(40) Mirkin, M. V.; Bard, A. J. "Simple analysis of quasi-reversible steady-state voltammograms." *Anal. Chem.* **1992**, *64*, 2293−2302.

(41) Burke, L. D.; Nugent, P. F. "The electrochemistry of gold: I the redox behaviour of the metal in aqueous media." *Gold Bull.* **1997**, *30*, 43–53.

(42) Kisler, K.; Kim, B. N.; Liu, X.; Berberian, K.; Fang, Q.; Mathai, C. J.; Gangopadhyay, S.; Gillis, K. D.; Lindau, M. "Transparent Electrode Materials for Simultaneous Amperometric

Detection of Exocytosis and Fluorescence Microscopy." *J. Biomat. Nanobio.* **2012**, *3*, 243–253.

(43) Trouillon, R.; Ewing, A. G. "Single Cell Amperometry Reveals that the Glycocalyx Hinders the Release of Neurotransmitters During Exocytosis." *Anal. Chem.* **2013**, *85*, 4822–4828.

Chapter 4. FAST DETECTION OF SINGLE LIPOSOMES USING A COMBINED NANOPORE MICROELECTRODE SENSOR

The work presented in this chapter has been published in the following paper:

1) *Barlow, S. T.; Zhang, B. "Fast Detection of Single Liposomes Using a Combined Nanopore Microelectrode Sensor." Anal. Chem.,* ***2020****, 92, 11318–11324.*

4.1 INTRODUCTION

Resistive-pulse sensing (RPS) is a powerful analytical technique for detection of single particles and molecules as they translocate through a nanopore.[1-4] Particles are usually detected by monitoring the transient changes in the nanopore's ionic current associated with particle translocation events. The passage of a particle through the pore transiently excludes ions from the pore and is resolved as a fast decrease in the ionic current, i.e. a resistive-pulse. The magnitude of this resistive-pulse is related to the size of the object blocking the pore, making RPS a useful technique for counting and sizing small objects like nanoparticles,[5-7] liposomes[8-12] or vesicles,[13] single proteins,[14] DNA,[15] viruses,[16] and organic molecules,[17] provided the precise geometry of the nanopore is known *a priori*.[5,16,18]

Because RPS is in general a size-based method, coupling RPS to a second analytical technique may offer additional chemical information not available from the nanopore sensing alone. For this purpose, amperometry is advantageous due to its simple setup, which is similar to that used in RPS, and its μs temporal resolution. Moreover, both microelectrode amperometry and RPS are popular electroanalytical techniques for ultrafast single entity measurements. To this end, the White group precisely quantified the velocity and collision behavior of polystyrene nanoparticles *via* resistive-pulse delivery to a Pt ultramicroelectrode (UME).[19] Mirkin and coworkers demonstrated simultaneous RPS and electrochemical quantification of redox-filled liposomes using a unique carbon-nanopipette system.[11] More recently, they reported electrochemical RPS of biological entities and nanoparticles inside single cells.[20] The Ewing group

used RPS to size vesicles isolated from adrenal chromaffin cells and electrochemically quantify them using vesicle impact electrochemical cytometry (VIEC),[13] demonstrating the first direct measurements of neurotransmitter concentration in vesicles. However, key challenges remain for both electrochemical RPS[11,20] and VIEC.[13] In both studies, liposomes/vesicles/organelles are electrochemically detected *via* electroporation;[21-23] this electric field-induced membrane breakdown allows detection of vesicular cargoes, but the timescale of breakdown may vary from milliseconds to minutes.[11,13,20-24] Throughput can be limited to a few detections per second or even minute. As a result, assigning individual resistive-pulses to their corresponding amperometric signals can be ambiguous, which may reduce measurement accuracy.

Inspired by these recent studies,[11,13,20] we were interested in developing an alternative nanopore/microelectrode-based method for high throughput electrochemical detection of single vesicles. We synthesized liposomes filled with high-concentration ferrocyanide ($Fe(CN)_6^{4-}$) to function as an analog for isolated, biological vesicles. Driving the liposomes through a pipette nanopore using high applied pressure (P_{app}) facilitated high-throughput, stable recordings of resistive-pulses lasting 10s of minutes. By carefully aligning a carbon-fiber microelectrode (CFE) with the solution stream exiting the nanopore, we achieved simultaneous detection of fast sub-ms resistive-pulses and amperometric redox signals. Critically, resistive-pulses and redox signals were well aligned in time and detected in unambiguous pairs, with >80% of resistive-pulses possessing a matching redox signal. Further, the paired event frequency could be modulated by increasing P_{app}; 100s to 1000s of paired events could be collected in minutes using our technique. Surprisingly, our results suggest that our technique achieves electrochemical detection of liposomes *via* a different mechanism than previous methods (e.g., VIEC) relying on electroporation.[11,13,20-23,26,27] Rather, the similar diameter of the nanopore orifice and the liposomes results in liposome rupture/leakage *during* translocation across the pore orifice; liposome contents are detected at the microelectrode surface before RPS events terminate. Our technique may be useful for unique insights into membrane biophysics under extreme flow conditions. We intend to further develop the present technique for high-throughput, direct measurements of intravesicular concentration, which will facilitate rapid analysis of liposomal drug delivery platforms or isolated, neurotransmitter-containing vesicles. Subsequent

work will focus on precisely understanding the relationship between nanopore geometry and liposome rupture, improving the coulometric efficiency of electrochemical detection, and the development of direct sizing of translocating particles.

4.2 EXPERIMENTAL

4.2.1 Chemicals and Materials

Sodium chloride (NaCl), potassium chloride (KCl), HEPES (4-(2-hydroxyethyl)-1-piperazineethanesulfonic acid), ferrocenemethanol (FcMeOH), potassium ferrocyanide trihydrate ($K_4Fe(CN)_6 \cdot 3H_2O$) and potassium ferricyanide ($K_3Fe(CN)_6$) were purchased from Sigma. DOPC (1,2-dioleoyl-sn-glycero-3-phosphocholine), DOPE (1,2-dioleoyl-sn-glycero-3-phosphoethanolamine) and cholesterol (ovine wool, >98%) were purchased from Avanti Polar Lipids. All chemicals used were reagent grade. Solutions were prepared in ultrapure water (Barnstead Smart2Pure, Thermo Scientific).

4.2.2 Preparation of Liposomes

Lipids dissolved in chloroform (25 mg/mL) were mixed in a mass ratio of 2:1:1 to obtain a concentration of 9.07 mM DOPC, 4.80 mM DOPE, and 9.24 mM cholesterol (Avanti Polar Lipids, USA) before chloroform evaporation as described previously.[21] A thin lipid film was formed by evaporating chloroform under N_2 for 30 min followed by 2 h in a desiccator under vacuum to evaporate any trace organic solvent present in the lipid film. Dried lipid films were hydrated for 1 h with 2 mL of buffer (142 mM NaCl, 10 mM HEPES, pH 7.4) containing 700 mM $K_4Fe(CN)_6$ or $K_3Fe(CN)_6$ and vortexed periodically to support mixing. Hydrated lipid solution was extruded 21 times through a 200 nm polycarbonate membrane (Whatman, USA) using a mini-extruder (Avanti Polar Lipids, USA) to obtain 200 nm liposomes. The extruded solution was then diluted to a final volume of 30 mL with buffer and centrifuged at 10,000 g for 1 h to obtain a liposome pellet, which was resuspended in 2 mL of buffer. Liposomes were stored at 4 °C and all experiments were conducted within 48 h of synthesis.

4.2.3 Nanopore Fabrication

For fabrication of nanopores, quartz capillary tubing (1.0 mm O.D., 0.5 mm I.D.) (National Quartz, USA) was pulled using a CO_2 laser puller (P-2000, Sutter Instrument, USA). Program parameters were as follows: HEAT = 445, FIL = 1, VEL = 30, DEL = 140, PUL = 175.

4.2.4 Carbon-Fiber Microelectrode (CFE) Fabrication

CFEs were prepared as described previously.[25] Briefly, a carbon fiber (5 μm) was aspirated into a borosilicate glass capillary (1.2 mm O.D., 0.9 mm I.D., Sutter Instrument, USA) that was pulled to a fine tip using a P-97 pipet puller (Sutter Instrument, USA). The microelectrode was cut and sealed in epoxy (Epoxy Technologies), followed by curing for 2 h at 150 °C. CFEs were polished at a 45° angle on a home-built micropipette beveler. CFEs were backfilled with 3 M KCl to establish electrical contact and characterized with cyclic voltammetry (-0.4 to +0.6 V, 100 mV/s, vs. Ag/AgCl) in 1 mM FcMeOH, 100 mM KCl. Only electrodes demonstrating good electron-transfer kinetics and stable i-V curves were used for liposome experiments.

4.2.5 Detection of Redox-Filled Liposomes

Liposome stock suspension was diluted in buffer 1000x and loaded into pipette nanopores through a 0.45 μm PES syringe filter (Whatman, USA). Loaded nanopores were directly interfaced with a FemtoJet injection system (Eppendorf) and subjected to an applied pressure, P_{app}. P_{app} was 75 p.s.i., unless otherwise indicated. A Dagan Chem-Clamp amplifier (Dagan Corporation, USA) was interfaced to the nanopore *via* an Ag/AgCl wire to achieve resistive-pulse measurements. To achieve simultaneous electrochemical detection of liposomes, a CFE interfaced to an Axopatch 200B current amplifier (Molecular Devices, USA) was carefully aligned to the nanopore orifice. CFE positioning was achieved using a hydraulic micropositioner (Narishige, Japan). For both measurements, the current was filtered at 10 kHz using an internal low-pass Bessel filter. Currents were sampled at 100 kHz using a Digidata 1322 digitizer (Molecular Devices, USA). All applied potentials were referenced to a Ag/AgCl reference electrode.

4.2.6 Data Analysis

Resistive-pulse signals were analyzed for their duration (full-width at half-maximum, ms) and *%Δi* (percent current change from baseline). Redox signals collected from the CFE were analyzed for several parameters, including: I_{max} (peak amplitude, pA), $t_{1/2}$ (full width at half-maximum, ms), and Q (integrated charge, fC). Q was converted to $N_{molecules}$ (number of molecules) using Faraday's Law, $Q = nFN$, where n is the number of e^- transferred (1 e^- for $Fe(CN)_6^{4-}/Fe(CN)_6^{3-}$) , F (96485 C/mol) is Faraday's constant, and N is the number of moles. Spike parameters were identified using pClamp v10.6 software (Molecular Devices, USA). A spike was identified if the I_{max} exceeded 5 times the standard deviation (SD) of the noise. All identified spikes were inspected, and unfit spikes were manually discarded (such as double or superimposed spikes). Redox signals were paired to parent resistive-pulses by quantifying the temporal difference between peak positions. Signals were paired if their time difference (τ_{delay}) was less than 3 ms. False positives were manually rejected. Statistics are reported as the mean ± SEM (standard error of the mean). Statistical significance was assessed using student's t-test for pair-wise comparisons and ANOVA for one-way comparisons across groups.

4.3 Results and Discussion

4.3.1 Nanopore/CFE Detection of Redox-Containing Liposomes

Figure 4.1A shows the scheme for the nanopore/microelectrode setup for detection of single liposomes. We carefully positioned a laser-pulled quartz nanopipette loaded with redox-filled ($Fe(CN)_6^{4-}$, unless noted otherwise) liposomes in the vicinity of a 5 µm CFE surface. We applied a large pressure to the nanopipette (P_{app} = 25-75 p.s.i), which caused liposomes (~200 nm diameter, **Figure S4.1**) to translocate across the nanopipette orifice (nanopore, **Figure S4.2**). We monitored these translocations by applying a positive DC voltage bias (E_{app} = +1.0 V vs. Ag/AgCl reference electrode), which permitted measurement of the nanopore's ionic current and resolution of the fast translocation events as resistive-pulses. A second DC voltage bias applied to the CFE (vs. Ag/AgCl) facilitated detection of redox species released from

liposomes as redox signals. The signals shown in **Figure 4.1A** are typical resistive-pulses (orange, downward current deflections) corresponding to liposome translocation through the nanopore, and redox signals (black, upward current deflections) corresponding to faradaic current from electrolysis of liposome contents at the CFE. Interestingly, we observed that these resistive-pulse/redox signals occurred in discrete pairs, with oxidation/reduction of liposome contents occurring *coincidently* with resistive-pulses. **Figure 4.1B** shows a 15 second simultaneous recording of both the CFE and nanopore signal showing numerous coincident detection (co-detection) events.

While performing these experiments, we made an intriguing observation: redox signals and their parent resistive-pulses arose *coincidently*. **Figure 4.1C** displays 5 randomly selected signal pairs; for each pair, a dotted line was drawn to indicate when the resistive-pulse begins. One can see that the redox signal occurs coincidently with the resistive-pulse – there is essentially no observable time delay between the two signals. These results suggest that the CFE surface "sees" the redox molecules as soon as the liposome enters the sensing zone of the nanopore. Since the CFE is positioned outside of the pipette and the sensing zone of the nanopore probably extends ~1 μm into the pipette at these orifice diameters,[5] it is likely that redox molecules are being released from liposomes *before the liposome reaches the pore orifice*. As will be shown in the next section, we believe these molecules are detected on the CFE surface before the liposome touches the CFE surface.

To verify that the redox signals recorded at the CFE arise from oxidation/reduction of released redox molecules from liposomes, we performed a series of experiments varying the CFE potential and the liposome loading conditions. **Figure 4.2A** shows a typical paired nanopore/CFE recording in which liposomes loaded with an oxidizable species, $Fe(CN)_6^{4-}$, were detected. The nanopore and CFE were both held at E_{app} = +1 V vs. Ag/AgCl. Here, from 13 liposome translocations detected, we collected 11 redox signals.

By varying the applied CFE potential from 0 to +1 V while holding the nanopore at E_{app} = +1 V, we found that redox signal frequency increased to a plateau at more oxidizing potentials (**Figure 4.2B**). Interestingly, we observed only a few, low amplitude redox signals beginning at E_{app} = 0.4 V, with higher

amplitude signals observed at E_{app} = 1.0 V, in good agreement with the cyclic voltammogram (CV) for 10 mM $Fe(CN)_6^{4-}$ (**Figure 4.2C**, **Figure S4.3**). When we repeated the experiment with liposomes loaded with a reducible redox species, $Fe(CN)_6^{3-}$, we found that redox signals were only detected when the CFE was held at reducing potentials (the nanopore potential was maintained at E_{app} = +1.0 V), which agreed with the cyclic voltammogram for 10 mM $Fe(CN)_6^{3-}$ (**Figure S4.4**). Conversely, we were unable to observe any redox signals on the CFE when we performed the nanopore/CFE experiment with liposomes loaded only with buffer (**Figure S4.5**). Taken together, these experiments demonstrate that redox signals are indeed due to the release of redox contents from liposomes.

In addition, the frequency of resistive-pulses and redox signals was controlled by the concentration of liposome particles present. As liposome concentration increased ~100-fold, resistive-pulse detection frequency increased from 0.7 ± 0.2 s^{-1} to 135 ± 34.7 s^{-1}, while redox signal detection frequency increased from 0.6 ± 0.1 s^{-1} to 82.4 ± 2.0 s^{-1} (**Figure S4.6**). We note that the number of resistive-pulses was always greater than the number of redox signals, especially at higher liposome concentrations, suggesting that there is a stochastic component to the detection mechanism, consistent with other studies.[11,13,21-23,25,26]

4.3.2 Effect of Nanopore/CFE Distance

Interestingly, we found that the distance between the nanopore orifice and the CFE surface plays a critical role in successful liposome detection (**Figure S4.7**). Although liposomes can always be detected at the nanopore *via* RPS for our liposome/nanopore combination, detection of associated redox signals is limited to an inter-probe distance of less than ~7 μm between the nanopore orifice and CFE surface. These results are summarized in **Figure 4.3** (for optical micrographs of corresponding nanopore/CFE positioning, see **Figure S4.8**). One can readily observe in **Figure 4.3A** that resistive-pulses and redox signals still occurred in well-resolved pairs as the inter-probe distance increased from ~0.5 μm to 6.0 μm, but redox signal amplitude decreased, while redox signal durations increased. Average signals from each trace are compared in **Figure 4.3B**. Redox signal half-widths, $t_{1/2}$, increased significantly from 0.15 ± 0.01 ms to 0.67 ± 0.06 ms (**Figure 4.3C**, statistically significant by one-way ANOVA, $p < 2.2e\text{-}16$) as inter-probe

distance increased from ~0.5 µm to 6.0 µm. We also observed an increasing time delay, τ_{delay}, between redox signals and their preceding resistive-pulse, increasing from 60 ± 10 µs to 1.2 ± 0.06 ms (**Figure 4.3D**, statistically significant by one-way ANOVA, p < 2.2e-16). The decreasing peak amplitude and increasing peak width of redox signals with increasing inter-probe distance resemble classic diffusional broadening experiments by Wightman and coworkers in their recordings of exocytosis events from single cells using CFEs.[28] When they increased the distance between the CFE and the cell surface (site of redox molecule release), they also observed smaller amplitude, temporally-broadened peaks due to molecular diffusion. Taken together with the increasing value of τ_{delay} with inter-probe distance, our data strongly suggest that liposomes are releasing their contents at the nanopore orifice, rather than upon collision with the CFE surface.

4.3.3 Effect of the Applied Pressure

We discovered that there was a minimum applied pressure (P_{app}) for successful liposome detection. We began to observe paired RPS/redox signals with appreciable frequency starting at P_{app} = 25 p.s.i.; below 25 p.s.i., the pipette suffered from constant clogging (data not shown). When the P_{app} was increased from 25 to 75 p.s.i., the overall detection frequency increased significantly, from 3.1 ± 0.7 s^{-1} to 16.1 ± 1.7 s^{-1} (**Figure 4.4A,B**) due to faster fluid flow. Increasing P_{app} also increased the proportion of resistive-pulses with a paired redox signal, from 75.8 ± 4.5% at 25 p.s.i. to 86.3 ± 1.6% at 75 p.s.i. This suggested that the speed of fluid flow may influence the probability of liposome opening and detection, though this was not statistically significant by ANOVA (p=0.145). A second key observation was that the average amplitude of resistive-pulses and redox signals decreased at higher pressures. The resistive-pulse amplitude, Δi, decreased significantly from Δi = 15.7 ± 1.4 % at 25 p.s.i. to Δi = 4.9 ± 0.3% at 75 p.s.i. As the magnitude of Δi is proportional to the size of the object translocating across the nanopore, this result implied that liposomes are compressed in response to faster fluid flow at higher pressures (**Figure 4.4C**). Compared to the RPS signal, the redox signal (I_{max}) decreased from 229 ± 14.6 pA to 171 ± 4.9 pA (**Figure 4.4D**). The

decrease in redox signal could be due to faster fluidic flow pushing the CFE surface away, which may result in decreased coulometric efficiency per liposome.

4.3.4 Effects of Pore Size and Voltage Bias

The nanopore diameter also played a key role in liposome detection. Pores with diameters near the average diameter of synthesized liposomes (180-250 nm) produced paired RPS/redox signals. Pores smaller than this range clogged easily (**Figure S4.9**). Pores with diameters >300 nm, on the other hand, could only produce small RPS signals with reduced signal-to-noise ratio and no paired redox signals. The absence of redox signals could possibly be due to reduced pore/liposome interaction as liposomes pass through a larger pore orifice.

Interestingly, we did not find a clear dependence between our ability to observe redox signals and the applied voltage bias across the pore orifice (**Figure S4.10A**); redox signal frequency did not change significantly as the nanopore E_{app} was varied from -1 to +1 V in 0.25 V increments (**Figure S4.10B**). This was unexpected, as we had anticipated that the strong electric field confined to the nanopore orifice would decrease liposome membrane stability during translocation through the pore orifice or even cause liposomes to open *via* electroporation. [11,13,21-23,26,27] This result may imply that the electric field at the pore orifice is either insufficient for electroporation and/or liposomes travel too quickly through the electric field to undergo electroporation. Quantitatively, there was a minor relationship between the magnitude of the nanopore E_{app} and the total number of redox molecules, $N_{molecules}$, detected at the CFE. The maximum $N_{molecules}$ detected occurred at E_{app} = 0 V, perhaps indicating that the nanopore electric field influences the motion of molecules to the CFE (**Figure S4.11**). We also note that E_{app} influenced the resistive-pulse frequency, due to the common threshold used to identify peaks – at smaller E_{app}, fewer resistive-pulses can be identified due to their smaller SNR (**Figure S4.10B**).

4.3.5 Quantification of Redox Concentration

Though the present technique is remarkable for its throughput and reliability in simultaneous RPS and redox signal detection of redox-filled liposomes, currently we cannot use the technique to quantify redox concentration of individual liposomes. This is due to two primary challenges. First, it appears that only ~5-10% of the encapsulated redox molecules were detected on CFE. Liposomes used in this study were synthesized in the presence of 700 mM $Fe(CN)_6^{4-}$, but we only detected quantities corresponding to the encapsulation of 50 mM $Fe(CN)_6^{4-}$ (**Figure S4.12**). It is possible that liposomes rupture and reclose during fast nanopore translocation, resulting in partial release of their cargo to the CFE surface as has been observed during neurotransmitter exocytosis.[29] The behavior could also be explained by poor loading efficiency of $Fe(CN)_6^{4-}$ in liposomes, which has been observed in other studies.[11,21] The liposomes could also be multilamellar, which would dramatically decrease the available internal volume for $Fe(CN)_6^{4-}$ loading. Multilamellarity is favored by high salt (which screens surface charges on particles and lipids) and the use of neutral lipids (such as DOPC and DOPE),[30] both of which are present in our system.

Second, the magnitude of the nanopore signal *decreased* as a function of pressure (**Figure 4.4C**), indicating that liposomes may be more compressed with faster fluid flow. This may present a challenge in using the RPS signal for particle size measurement. A more accurate liposome size determination is needed to calculate internal redox concentration of individual liposomes. We believe this is possible once we more fully consider the possible relationship between particle shape, pore size, and applied pressure using a combination of numerical simulation and nanopore measurements.

4.4 CONCLUSIONS

In summary, we have demonstrated an electrochemical method for fast and continuous detection of single redox-containing liposomes. By aligning a microelectrode surface to a pipette nanopore and delivering liposomes onto the electrode, one can obtain a pair of simultaneously recorded current signals for each liposome corresponding to its translocation through nanopore and redox detection on the electrode. This detection method is both high throughput and robust allowing one to collect hundreds to thousands of

liposome detections in minutes, of which, 80% are resistive-pulse/redox signal pairs. Our results suggest that redox detection of liposome content is due to membrane rupture *during* translocation, in contrast to previous studies which rely on stochastic electroporation.

Despite its usefulness in liposome detection, challenges remain in using this method to analyze redox concentration. These include the lower apparent detection efficiency of redox content and the inability to estimate particle size using nanopore data. Our future work will understand the origin of the lower faradaic efficiency and extract liposome size information from nanopore data using microfabricated nanopores and simulation methods. We anticipate that we can further develop this method into a more useful analytical tool for fast single-liposome analysis. Such an analytical tool will find use in a variety of applications ranging from rapid analysis of liposomal drug formulations and high-throughput quantification of neurotransmitter concentration in single, isolated vesicles, as well as fundamental studies of liposome membrane dynamics under membrane stress.

4.5 FIGURES

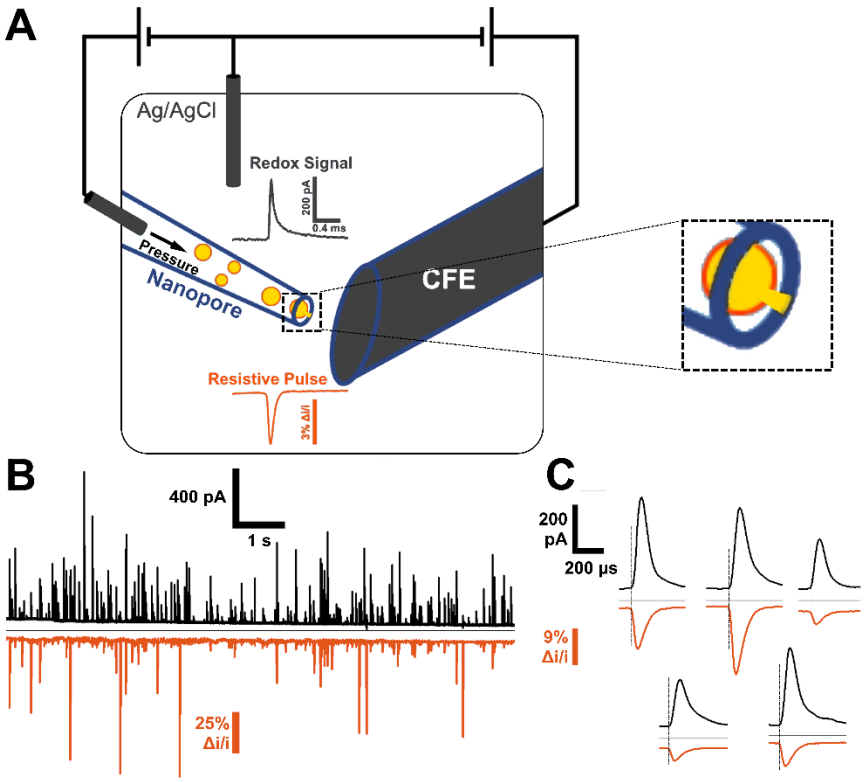

Figure 4.1. An integrated nanopore/microelectrode sensor for high-throughput detection of redox-filled liposomes. **A)** Scheme for detection. Liposomes were forcibly ejected from a nanopore using pressure. Due to the fast fluid flow and similar size of the nanopore orifice to the liposomes, liposomes ruptured/leaked during translocation (inset), releasing their contents to the carbon-fiber microelectrode (CFE) where they were oxidized/reduced. This resulted in paired resistive-pulses (orange) and redox signals (black). **B)** a typical simultaneous nanopore/CFE recording showing numerous co-detection events on both sensors in this 15 s trace. **C)** Redox signals and resistive-pulses occur coincidently, indicating that redox molecules leak out of liposomes during passage through the nanopore. A dotted line has been drawn where the resistive-pulse begins to guide the eye.

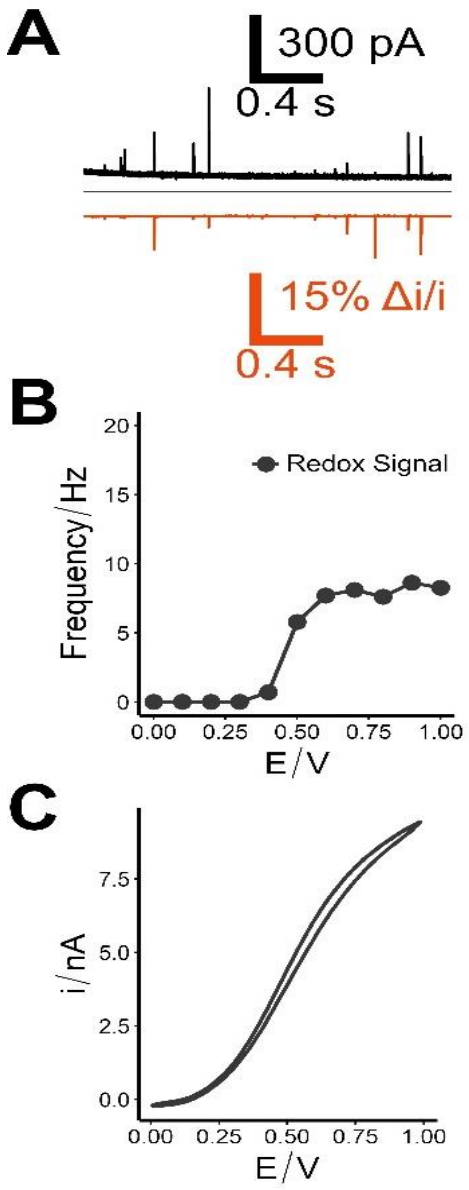

Figure 4.2. The applied potential bias (E) on the CFE controls observation of redox signals. **A)** A typical recording of liposomes synthesized in the presence of $Fe(CN)_6^{4-}$. Here, the nanopore and CFE are held at +1 V vs. Ag/AgCl. Redox signals are positive-going, indicating oxidation. **B)** Frequency of redox signals vs. CFE potential for liposomes loaded with $Fe(CN)_6^{4-}$. **C)** Cyclic voltammogram for 5 µm CFE in 10 mM $Fe(CN)_6^{4-}$, 142 mM NaCl, 10 mM HEPES, pH 7.4. Scanned 100 mV s^{-1} vs Ag/AgCl.

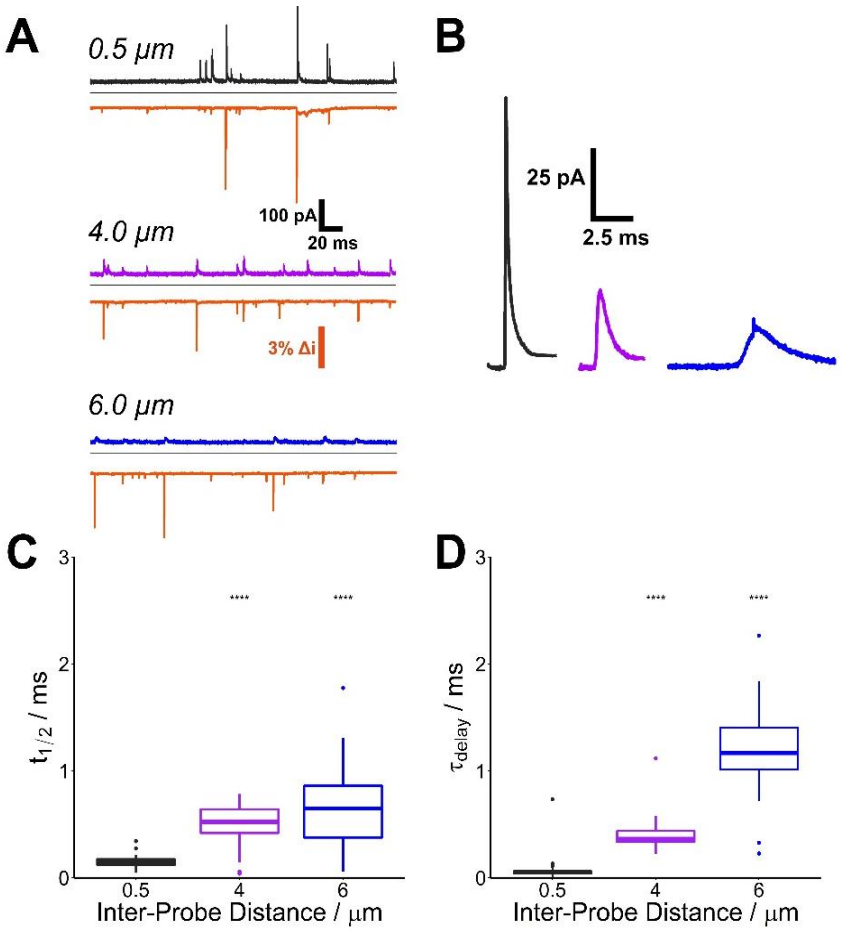

Figure 4.3. Dependence of redox signals on inter-probe distance suggests liposome leak molecules at the nanopore orifice. **A)** Recordings of paired resistive-pulses/redox signals at different CFE distances from the nanopore orifice. Redox signals broaden in time and decrease in amplitude. For optical micrographs corresponding to these recordings, see **Figure S8**. **B)** Average redox signals collected at the positions indicated in **A**. **C)** $t_{1/2}$ of redox signals increased with distance from nanopore orifice. **D)** The time delay, τ_{delay}, between resistive-pulses and their corresponding redox signals, increased with distance from the nanopore orifice. For **C)** and **D)**, statistical significance was assessed with one-way ANOVA and pair-wise with student's t-test. For both, $p < 2.2e\text{-}16$ by ANOVA. Reference group was 0.5 μm, ****=$p<0.0001$.

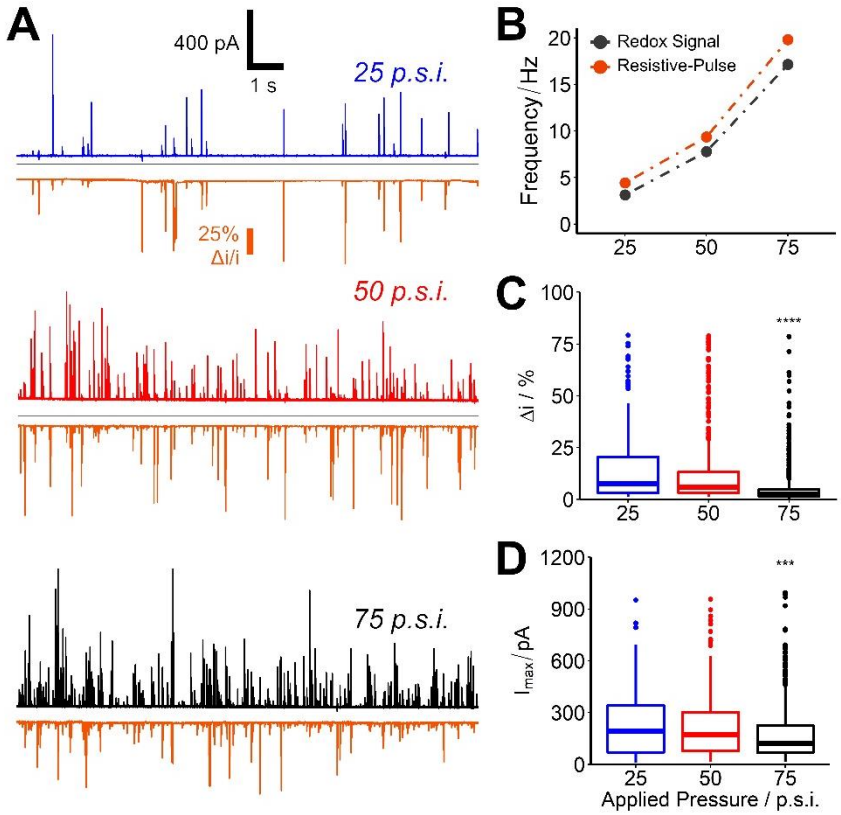

Figure 4.4. Increasing applied pressure (Papp) increased match frequency, probability of liposome rupture during translocation. **A)** Recordings of paired resistive-pulses/redox signals at different P_{app}. Frequency of signals increased as a function of P_{app} due to faster fluid flow through the nanopore orifice. **B)** Frequency of resistive-pulses (orange) and redox signals (grey) at different P_{app}. Proportion of resistive-pulses with a paired redox signal increased from 75% at P_{app} = 25 p.s.i. to 86% at P_{app} = 75 p.s.i. **C)** Δi (amplitude of resistive-pulse) decreased as a function of P_{app}. **D)** I_{max} (amplitude of redox signal) decreased as a function of P_{app}. For **C)** and **D)**, statistical significance was assessed pair-wise with student's t-test. Reference group was P_{app} = 25 p.s.i. *** = p<0.001, ****=p<0.0001.

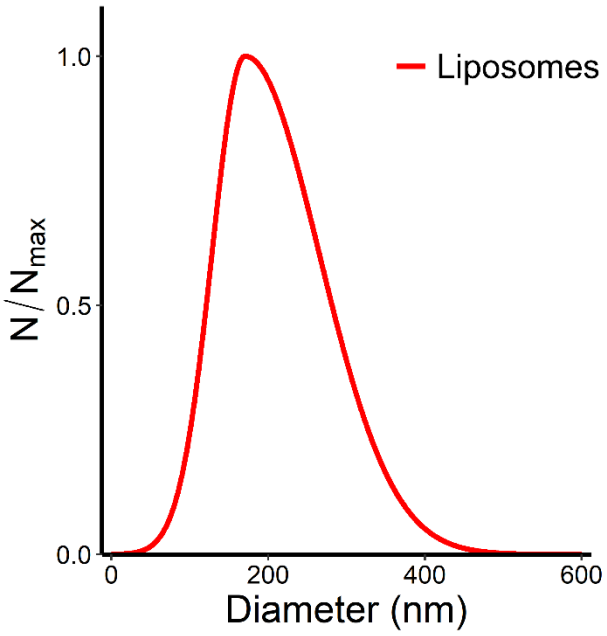

Figure S4.2. Dynamic Light Scattering (DLS) sizing of liposomes.
Average liposome diameter was 212.6 nm. Polydispersity index (PDI) for this sample was 0.11. Data is normalized to the max intensity observed diameter (N_{max}).

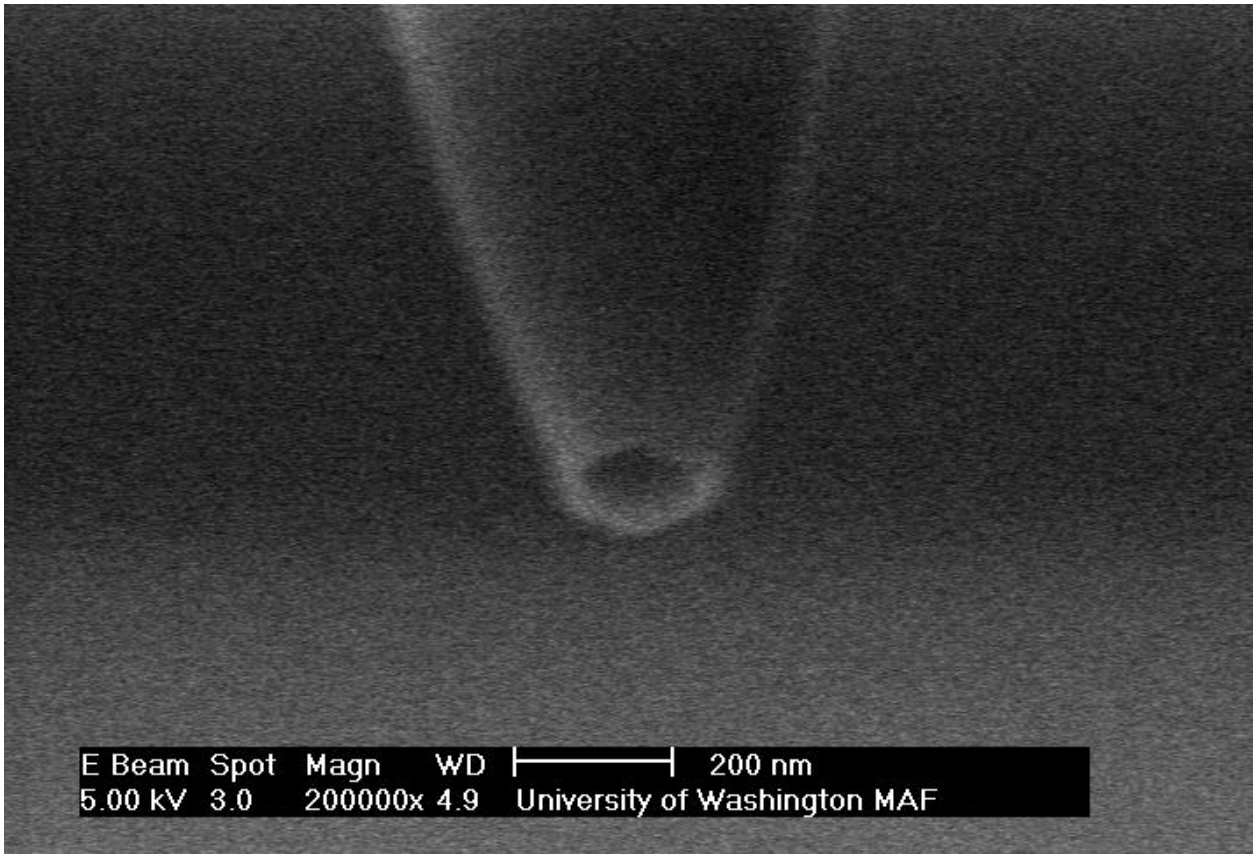

Figure S4.3. SEM image of a typical nanopore used for experiments, d = 180 nm.

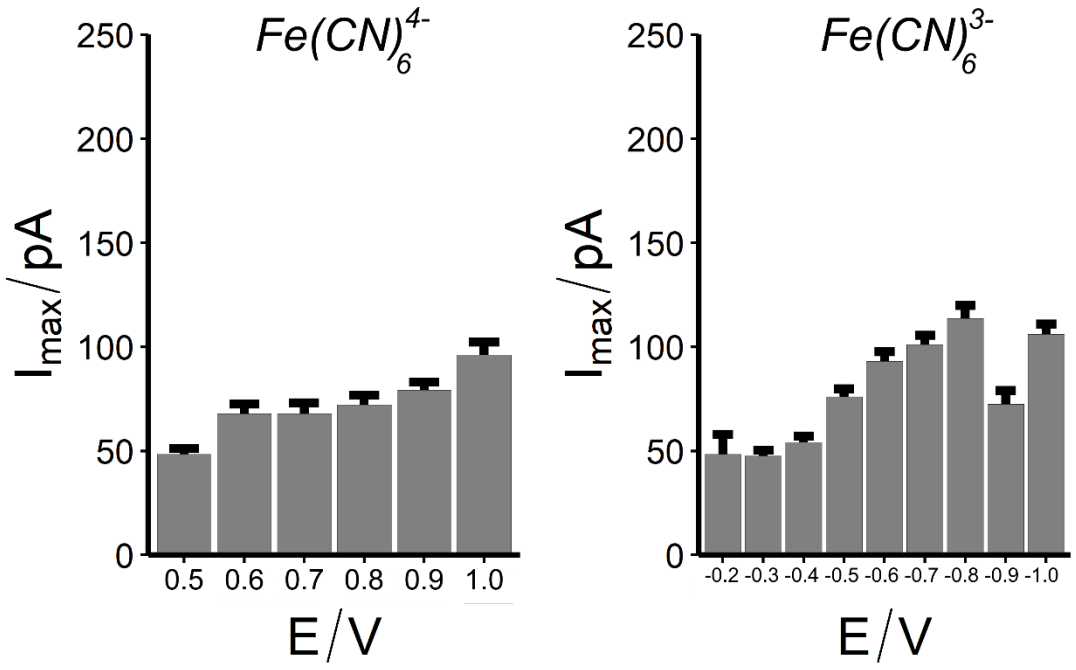

Figure S4.4. Dependence of redox signal amplitude on applied potential at carbon-fiber microelectrode. Left, signal amplitude (I_{max}) peaks at +1.0 V vs Ag/AgCl for liposomes loaded with $Fe(CN)_6^{4-}$. Right, signal amplitude (I_{max}) peaks at +0.8 V vs Ag/AgCl for liposomes loaded with $Fe(CN)_6^{3-}$

.

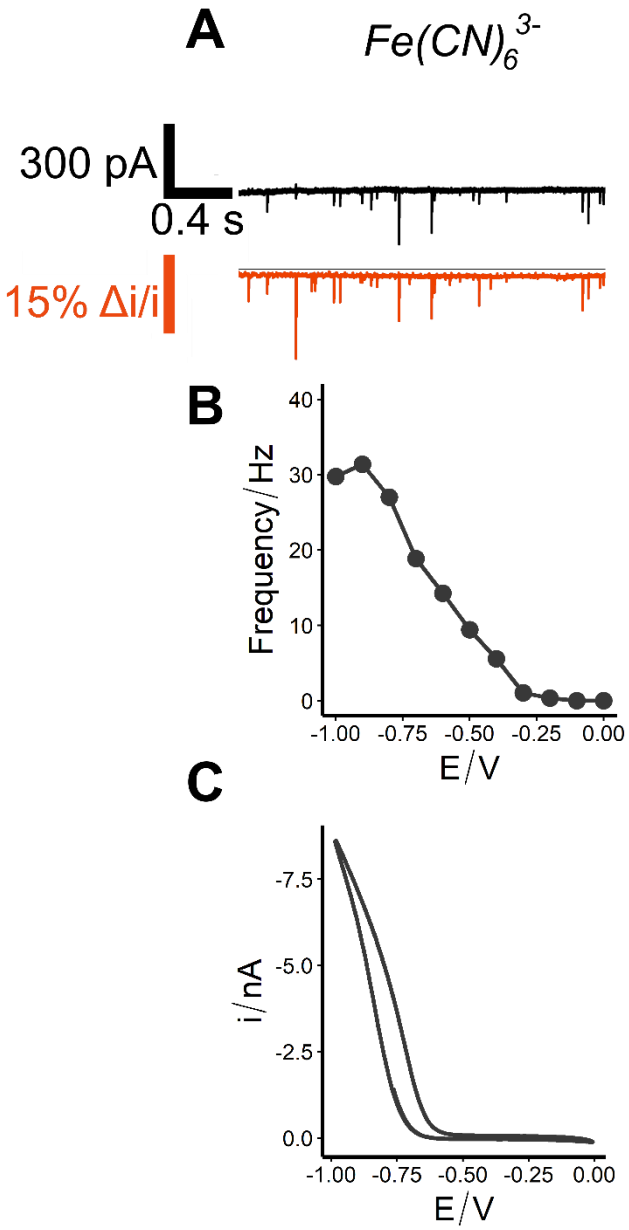

Figure S4.5. The applied potential bias (E) on the CFE controls observation of redox signals. **A)** A typical recording of liposomes synthesized in the presence of $Fe(CN)_6^{3-}$. Here, the CFE is held at -1 V vs. Ag/AgCl, while the nanopore is held at E = +1 V vs. Ag/AgCl. Redox signals are negative-going, indicating reduction. **B)** Frequency of redox signals vs. CFE potential for liposomes loaded with $Fe(CN)_6^{3-}$. **C)** Cyclic voltammogram for 5 µm CFE in 10 mM $Fe(CN)_6^{3-}$, 142 mM NaCl, 10 mM HEPES, pH 7.4. Scanned 100 mV s^{-1} vs Ag/AgCl.

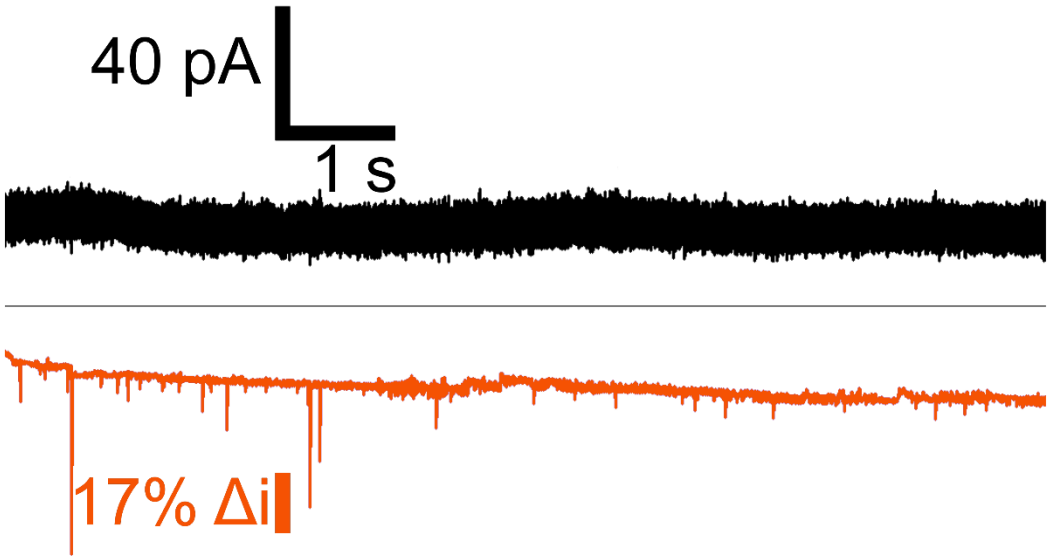

Figure S4.6. Liposomes loaded with only buffer and no redox mediator do not give rise to redox signals.

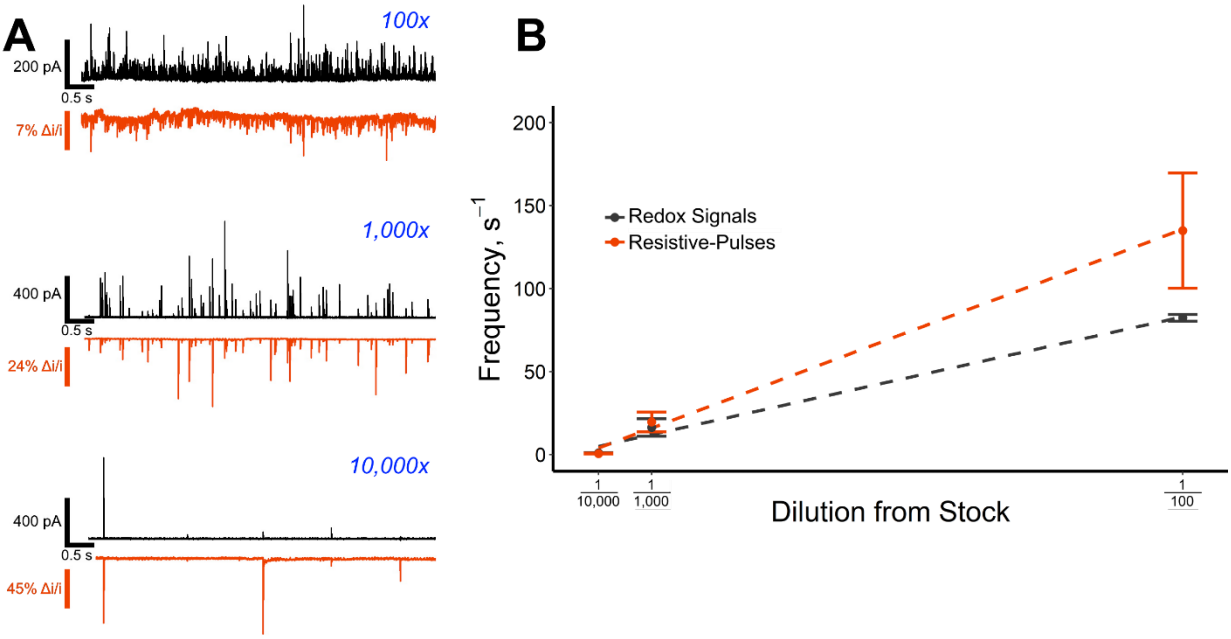

Figure S4.7. Concentration dependence of detection. When the dilution factor from stock suspension of liposomes was decreased (10,000x → 100x), we observed an increase in the event frequency for resistive-pulses and redox signals. **A)** Typical recordings for nanopipettes loaded with 100x, 1,000x, or 10,000x diluted liposomes. **B)** Relationship between event frequency and dilution factor. Resistive-pulse frequency is always higher than redox signal frequency, with a greater disparity at higher concentrations. This indicated that there is a stochastic component to successful redox signal detection.

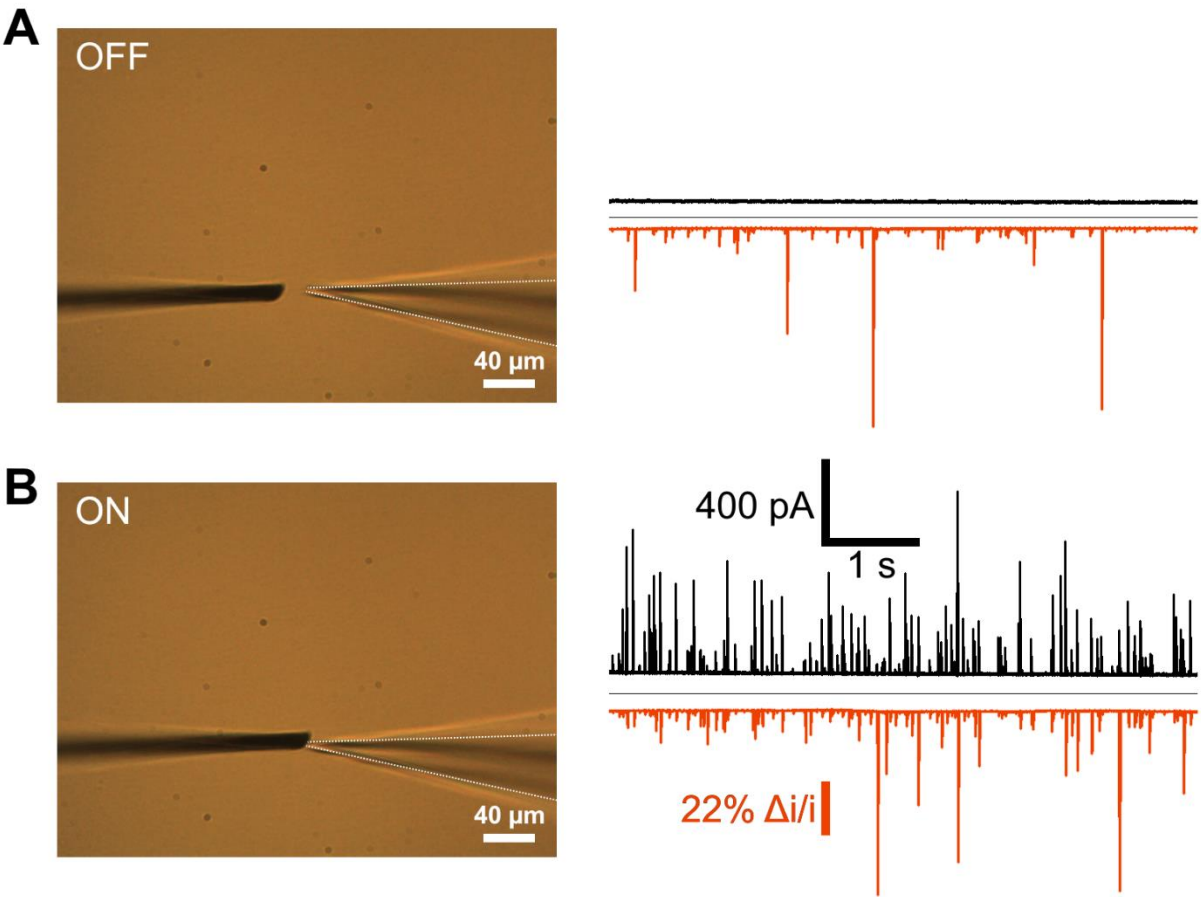

Figure S4.8. Typical experimental configuration. Estimated difference between the CFE surface and nanopore orifice is <1 µm. **A)** shows the microscope view and corresponding recording. No redox signals are observed when there is significant distance between the probes. **B)** shows the configuration of probes and response during successful redox signal generation. Paired signals are abundant.

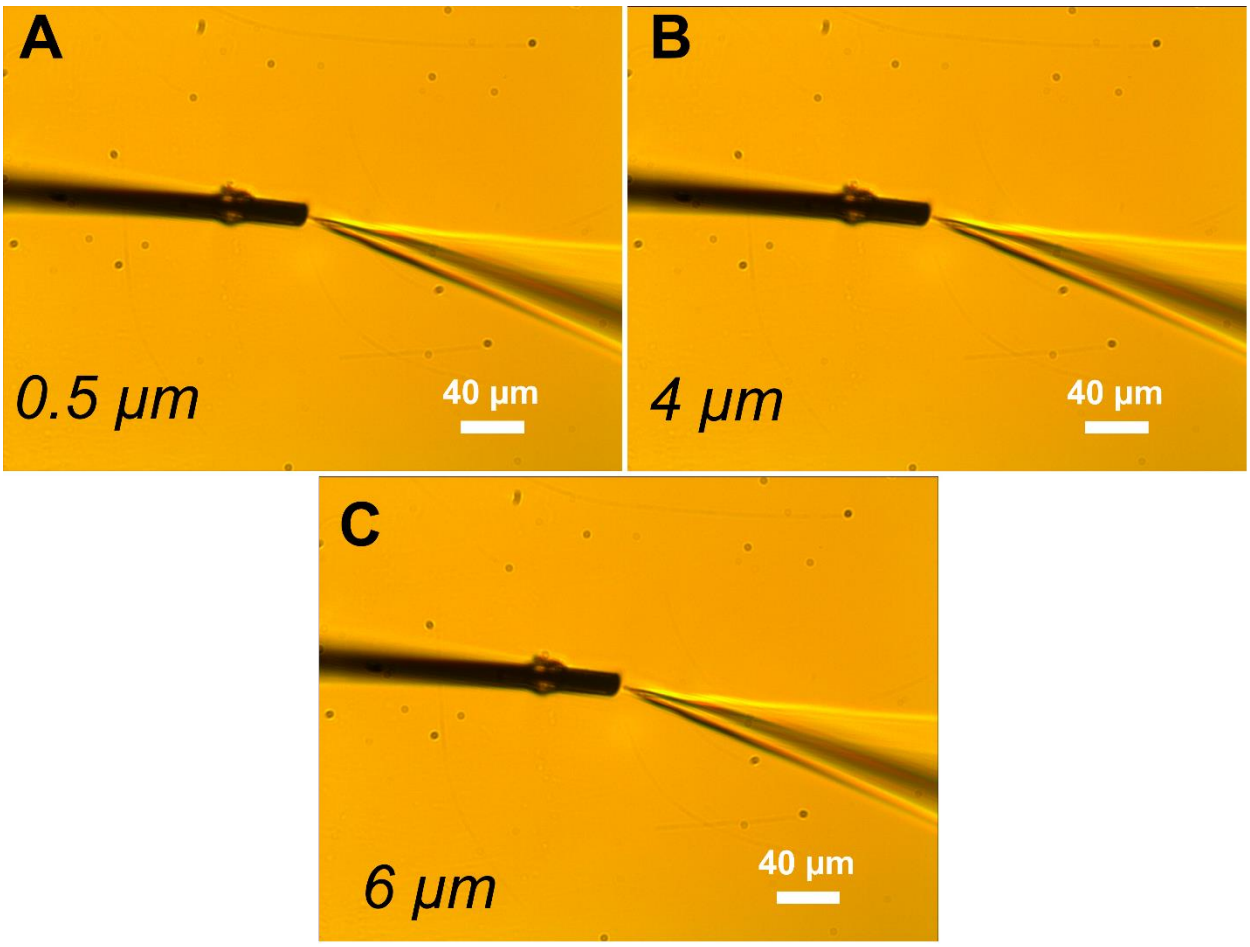

Figure S4.9. Zoomed-in optical microscope images corresponding to the distance dependence traces shown in main text **Figure 4.3**. **A)** No perceptible distance between CFE surface and nanopore orifice – we estimated to be ~0.5 µm. **B)** Measured distance 4 µm between probes. **C)** Measured distance 6 µm between probes.

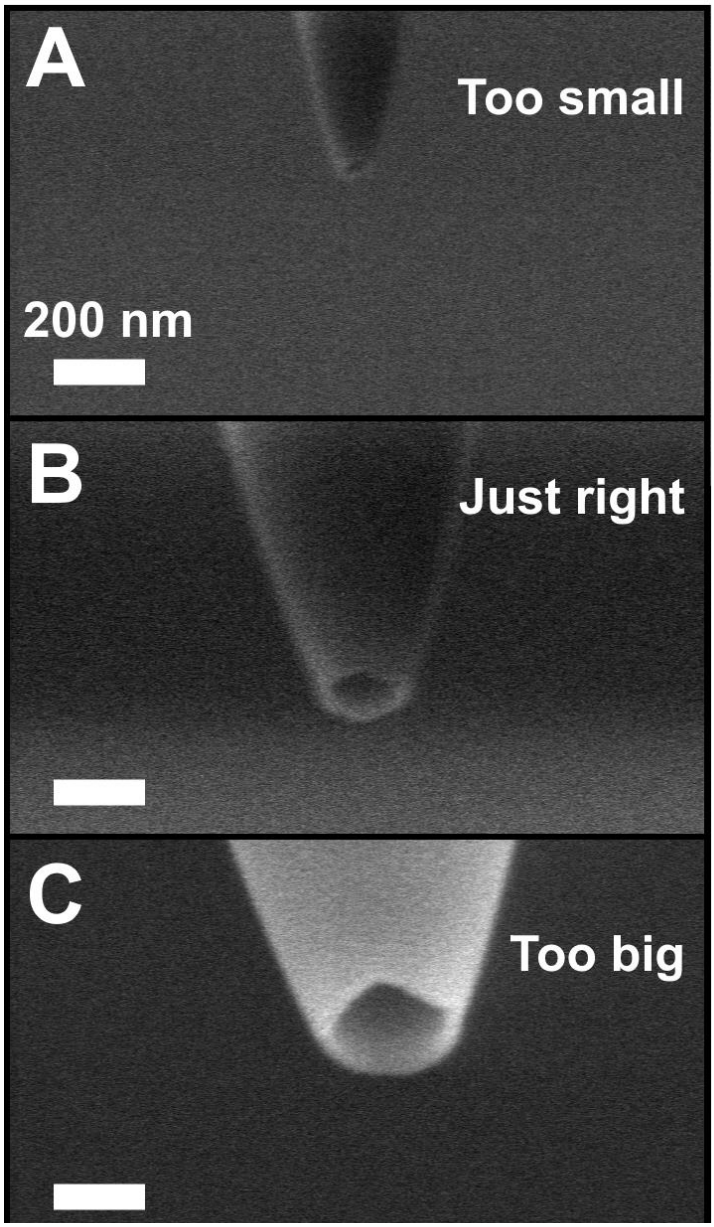

Figure S4.10. SEM images of nanopores used for experiments. **A)** Nanopores that were much smaller than the diameter of liposomes (d = 50nm) clogged immediately. No resistive-pulses or redox signals could be observed. **B)** Nanopores that were close to the diameter of liposomes (d=180 nm, but we found 170-250 nm were functional) could produce paired signals. **C)** Nanopores much larger than the diameter of liposomes (here, d=300 nm) could not produce paired signal behavior or produced paired signals rarely. We never observed redox signals without a preceding resistive-pulse, indicating that the size of the pore orifice relative to the liposome is a critical parameter for promoting paired signal behavior.

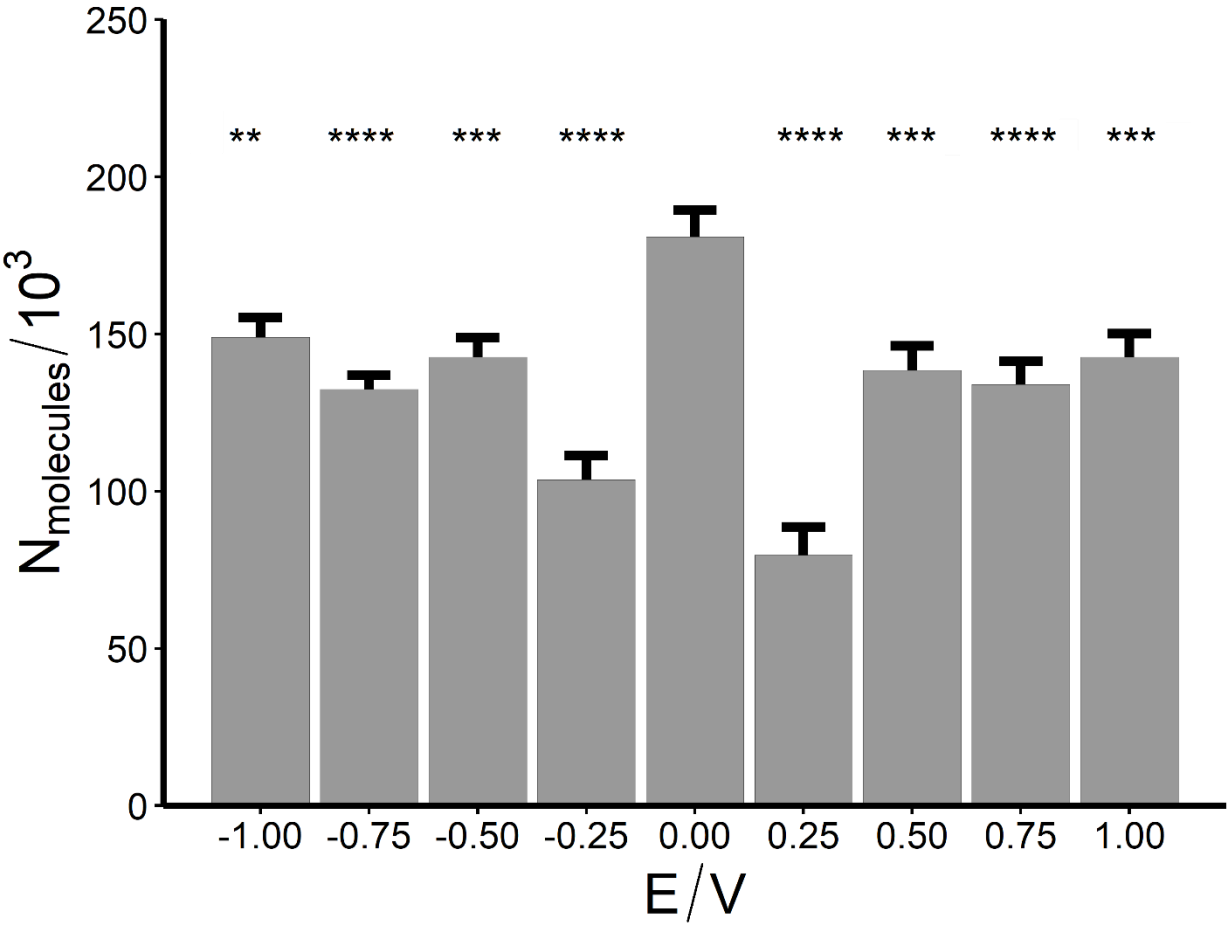

Figure S4.11. Nanopore electric field does not participate in redox signal generation. **A)** Recordings of paired resistive-pulses/redox signals. When the nanopore potential is switched from -1 V to 0 V or +1 V to 0 V, redox signals continue at the same frequency. **B)** Frequency vs applied nanopore potential (E_{app}) shows that the redox signal frequency is unrelated to E_{app}. Resistive-pulse frequency is also plotted, which shows a parabolic trend due to the common threshold used for resistive-pulse identification at all E_{app}. SNR increases as the magnitude of E_{app} increases, thus, more peaks are identified at large E_{app} than at small E_{app}.

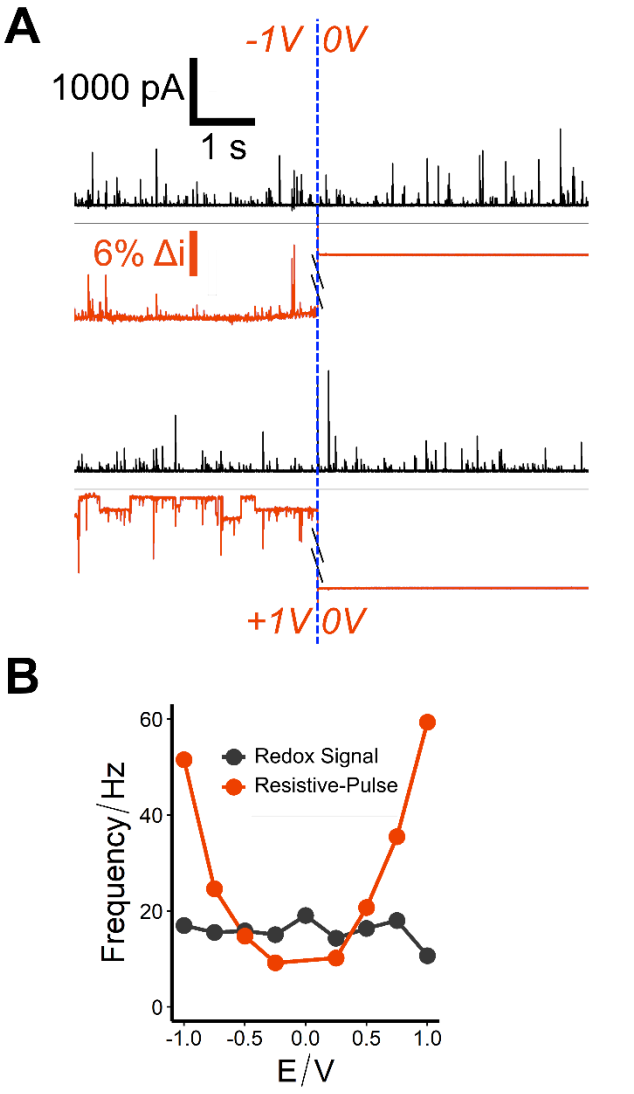

Figure S4.12. Applied nanopore voltage influences the detection of molecules at the CFE. We observed that signal-to-noise ratio and collection of molecules peaked when the nanopore E_{app} was 0 V, perhaps indicating that the nanopore electric field influences the motion of molecules to the electrode surface. Interestingly, there were local minima in detection at -0.25 V and 0.25 V. We do not know the origin of this behavior. Statistical significance was assessed pair-wise with student's t-test. Reference group was E_{app} = 0.00 V. ** = p<0.01, *** = p<0.001, ****=p<0.0001.

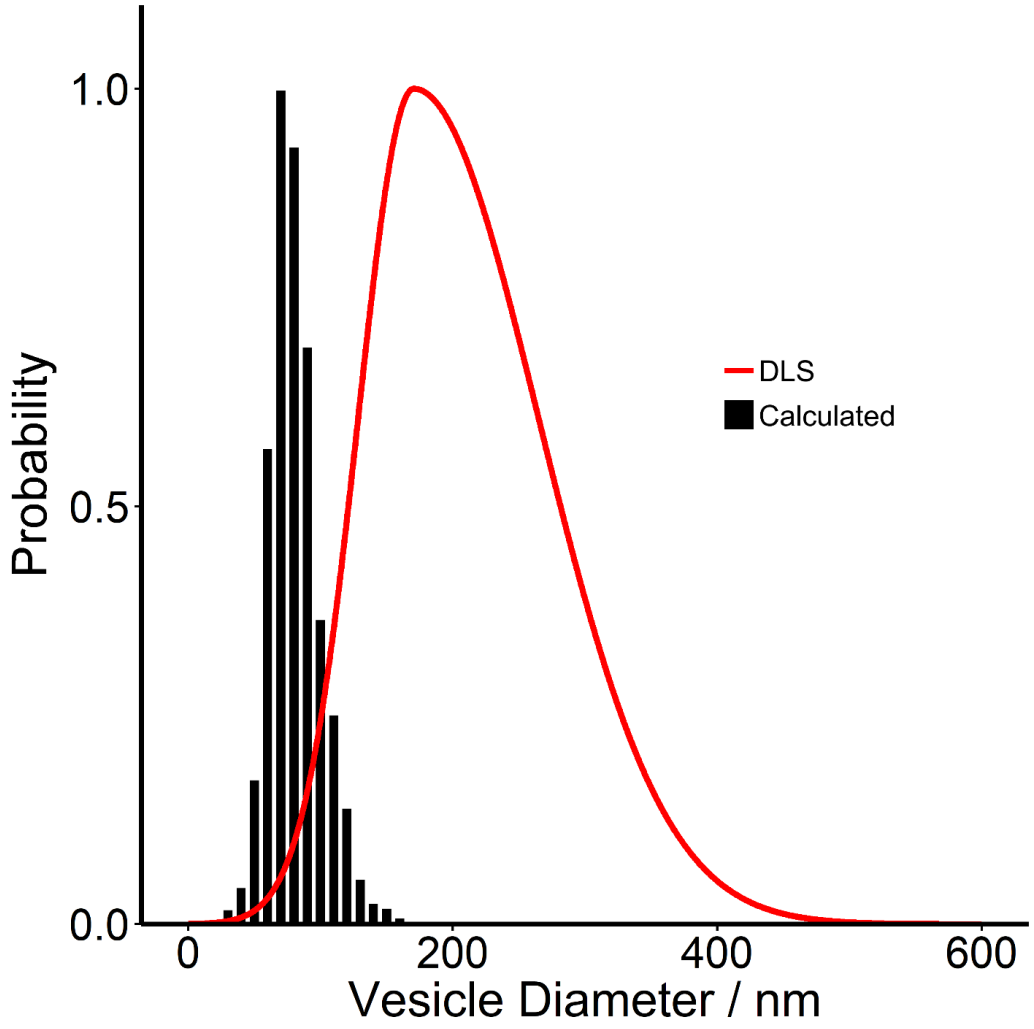

Figure S4.13. Liposome quantification is well below expectation. Using the charge in fC obtained from redox signals, we calculated the liposome diameter assuming our loading concentration of 700 mM $Fe(CN)_6^{4-}$ was fully encapsulated. Average liposome diameter d=90.5 ± 2.2 nm. DLS diameter d = 212.6 nm.

4.6 REFERENCES

(1) Luo, L.; German, S. R.; Lan, W.-J.; Holden, D. A.; Mega, T. L.; White, H. S. “Resistive-pulse Analysis of Nanoparticles.” *Annu. Rev. Anal. Chem.* **2014**, *7*, 513–535.

(2) Shi, W.; Friedman, A. K.; Baker, L. A. “Nanopore Sensing.” *Anal. Chem*. **2017**, *89*, 157−188.

(3) Wang, Y.; Wang, D.; Mirkin, M. V. “Resistive-pulse and Rectification Sensing with Glass and Carbon Nanopipettes.” *Proc. R. Soc. London, Ser. A* **2017**, *473*, 20160931.

(4) Bayley, H.; Martin, C. R. “Resistive-Pulse Sensing-From Microbes to Molecules.” *Chem. Rev.* **2000**, *100*, 2575−2594.

(5) Lan, W.-J.; Holden, D. A.; Zhang, B.; White, H. S. “Nanoparticle transport in conical-shaped nanopores.” *Anal. Chem.* **2011**, *83*, 3840–47.

(6) German, S. R.; Luo, L.; White, H. S.; Mega, T. L. “Controlling Nanoparticle Dynamics in Conical Nanopores.” *J. Phys. Chem. C* **2013** *117*, 703-711.

(7) Ito, T.; Sun, L.; Henriquez, R. R.; Crooks, R. M. "A Carbon Nanotube-Based Coulter Nanoparticle Counter." *Acc. Chem. Res.* **2004**, *37*, 937–945.

(8) Cox, J. T. and Zhang, B. "Resistive-pulse Analysis of Single Phospholipid Vesicles Using Quartz Nanochannels" *J. Electrochem.* **2017**, *23*, 207–216.

(9) Holden, D. A.; Watkins, J. J.; White, H. S. “Resistive-pulse detection of multilamellar liposomes.” *Langmuir* **2012**, *28*, 7572–77.

(10) Chen, L.; He, H.; Jin, Y. “Counting and Dynamic Studies of the Small Unilamellar Phospholipid Vesicle Translocation with Single Conical Glass Nanopores.” *Anal. Chem.* **2015**, *87*, 522−529.

(11) Pan, R.; Hu, K.; Jiang, D.; Samuni, U.; Mirkin, M. V. “Electrochemical Resistive-Pulse Sensing.” *J. Am. Chem. Soc.* **2019**, *141*, 19555-19559.

(12) Liu, Y.; Xu, C.; Chen, X.; Wang, J.; Yu, P.; Mao, L. “Voltage-driven Counting of Phospholipid Vesicles with Nanopipettes by Resistive-pulse Principle.” *Electrochem. Commun*. **2018**, *89*, 38−42.

(13) Zhang, X.-W.; Hatamie, A.; Ewing, A. G. “Simultaneous Quantification of Vesicle Size and Catecholamine Content by Resistive-pulses in Nanopores and Vesicle Impact Electrochemical Cytometry.” *J. Am. Chem. Soc.* **2020**, *142*, 4093-4097.

(14) Heins, E. A.; Siwy, Z. S.; Baker, L. A.; Martin, C. R. “Detecting Single Porphyrin Molecules in a Conically Shaped Synthetic Nanopore.” *Nano Lett*. **2005**, *5*, 1824−1829.

(15) Branton, D. et al. “The Potential and Challenges of Nanopore Sequencing.” *Nat. Biotechnol.* **2008**, *26*, 1146−1153.

(16) Terejánszky, P.; Makra, I.; Fürjes, P.; Gyurcsányi, R. E. “Calibration-less Sizing and Quantitation of Polymeric Nanoparticles and Viruses with Quartz Nanopipets.” *Anal. Chem.* **2014**, *86*, 4688− 4697.

(17) Gu, L. Q.; Braha, O.; Conlan, S.; Cheley, S.; Bayley, H. “Stochastic sensing of organic analytes by a pore-forming protein containing a molecular adapter.” *Nature* **1999**, *398*, 686–690.

(18) Kozak, D.; Anderson, W.; Vogel, R.; Chen, S.; Antaw, F.; Trau, M. “Simultaneous size and zeta- potential measurements of individual nanoparticles in dispersion using size-tunable pore sensors.” *ACS Nano* **2012,** *6*, 6990–97.

(19) McKelvey, K.; Edwards, M. A.; White, H. S. “Resistive-pulse Delivery of Single Nanoparticles to Electrochemical Interfaces.” *J. Phys. Chem. Lett.* **2016**, *7*, 3920−3924.

(20) Pan, R.; Hu, K.; Jia, R.; Rotenberg, S. A.; Jiang, D.; Mirkin, M. V. “Resistive-Pulse Sensing Inside Single Living Cells.” *J. Am. Chem. Soc.* **2020**, *142*, 5778-5784.

(21) Lovrić, J.; Najafinobar, N.; Dunevall, J.; Majdi, S.; Svir, I.; Oleinick, A.; Amatore, C.; Ewing, A. G. “On the mechanism of electrochemical vesicle cytometry: chromaffin cells and liposomes.” *Faraday Discuss.* **2016**, *193*, 65–79.

(22) Li, X.; Dunevall, J.; Ren, L.; Ewing, A. G. “Mechanistic aspects of vesicle opening during analysis with vesicle impact electrochemical cytometry.” *Anal. Chem.* **2017**, *89*, 9416–9423.

(23) Li, X.; Ren, L.; Dunevall, J.; Ye, D.; White, H. S.; Edwards, M. A.; Ewing, A. G. “Nanopore Opening at Flat and Nanotip Conical Electrodes during Vesicle Impact Electrochemical Cytometry.” *ACS Nano*, **2018**, *12*, 3010–3019.

(24) Riske, K. A.; Dimova, R. “Electro-deformation and poration of giant vesicles viewed with high temporal resolution.” *Biophys. J.* **2005**, 88, 1143–1155.

(25) Barlow, S. T.; Louie, M.; Hao, R.; Defnet, P. A.; Zhang, B. "Electrodeposited Gold on Carbon-Fiber Microelectrodes Enhances Amperometric Detection of Dopamine Release from PC12 Cells" *Anal. Chem.* **2018**, *90*, 10049-10055.

(26) Lebègue, E.; Anderson, C. M.; Dick, J. E.; Webb, L. J.; Bard, A. J. “Electrochemical Detection of Single Phospholipid Vesicle Collisions at a Pt Ultramicroelectrode.” *Langmuir*, **2015**, *31*, 11734–11739.

(27) Lebègue, E.; Barrière, F.; Bard, A. J. “Lipid Membrane Permeability of Synthetic Redox DMPC Liposomes Investigated by Single Electrochemical Collisions.” *Anal. Chem.* **2020**, *92*, 2401-2408.

(28) Schroeder, T. J.; Jankowski, J. A.; Kawagoe, K. T.; Wightman, R. M.; Lefrou, C.; Amatore, C. “Analysis of diffusional broadening of vesicular packets of catecholamines released from biological cells during exocytosis.” *Anal. Chem.* **1992**, *64*, 3077–83.

(29) Ren, L.; Mellander, L. J.; Keighron, J.; Cans, A.-S.; Kurczy, M. E.; Svir, I.; Oleinick, A.; Amatore, C.; Ewing, A. G. “The evidence for open and closed exocytosis as the primary release mechanism.” *Q. Rev. Biophys.* **2016**, *49*, e12.

(30) Scott, H. L.; Skinkle, A.; Kelley, E. G.; Waxham, M. N.; Levental, I.; Heberle, F. A. “On the Mechanism of Bilayer Separation by Extrusion, or Why Your LUVs Are Not Really Unilamellar.” *Biophys. J.* **2019** *117*, 1381–1386.

Chapter 5. MEMBRANE TENSION MODIFIES REDOX LOADING AND RELEASE IN SINGLE LIPOSOMES

The work presented in this chapter has been submitted for publication and is under review.

5.1 INTRODUCTION

Liposomes are soft nanoparticles comprised of a lipid bilayer (~5 nm thickness) enclosing an aqueous solution compartment. Liposomes are specifically useful as mimics for cell membranes, enabling the controlled study of diverse phenomena in membrane biophysics.[1] For example, giant unilamellar vesicles (GUVs, 1-200 μm diameter) can be observed with optical microscopy, making them useful for understanding dynamic membrane behavior such as phase separation,[2,3] domain formation,[4-6] and electroporation.[7-9] Conversely, small unilamellar vesicles (SUVs, 20-100 nm diameter) have been used as analogs for synaptic vesicles (30-50 nm diameter) to understand SNARE-triggered membrane fusion.[10-13]

Electrochemistry has recently emerged as a promising complementary technique for studying liposomes (100-400 nm diameter). Electrochemical methods, such as amperometry, have exceptional temporal resolution (sub-millisecond) and low limits of detection (a few thousand molecules).[14] Thus, amperometry has been useful for the direct quantitation of redox-active liposome contents as well as understanding how liposomes open during collision with an ultramicroelectrode (UME) surface.[15-17]

However, key questions remain in collision-based electrochemical detection of liposomes. What is the detection mechanism for liposomes colliding with an UME? It is critical to note that electrochemical detection of liposome contents requires the opening of the lipid bilayer upon collision – otherwise, contents will not be electrolyzed, as the lipid bilayer is too thick for efficient

electron tunneling unless other electroactive dopants or defects are added.[18-21] Consistent with this, Lebegué et al. showed that they failed to detect 100 nm DMPC liposomes upon collision with a Pt UME unless a sufficient concentration of surfactant was present, implying that membrane destabilization is critical to detection.[22] More recent work extended these results and added temperature and additional redox probes in solution as possible methods for membrane permeabilization.[23] By contrast, Cheng and Compton used carbon-fiber microelectrodes (CFEs) to detect commercial liposomes containing ascorbate; they demonstrated quantitative detection without any destabilizing agents present and suggested a detection mechanism due to complete rupture of the liposome upon collision.[24] The Ewing group used CFEs to detect liposomes loaded with dopamine (DA) but suggested an electroporation-based mechanism due to the dependence of detection frequency on applied potential.[25]

Critically, it is also unclear how liposomes are loaded with redox molecules and whether liposome detection is quantitative. The Ewing group attempted to load 400 nm liposomes with 150 mM DA, but only detected 40-70% of the expected amount – they attributed the disparity to poor encapsulation efficiency.[25] Our group and the Mirkin group recently published similar results using $K_4Fe(CN)_6$-loaded liposomes; the calculated concentration of $K_4Fe(CN)_6$ based on electrochemical signals was dramatically lower than the expected concentration.[26,27]

We were keenly interested in addressing these key points of liposome loading and release. By using amperometry, we measured the collision of $K_4Fe(CN)_6$-loaded, 200 nm liposomes with a 5 μm CFE. Importantly, the electroporation mechanism suggested by the Ewing group[25] should depend strongly on initial membrane tension, which can be tuned by modifying the osmolarity of the buffer in which liposomes are suspended. Indeed, we found that we could manipulate the frequency of amperometric events by altering the osmolarity of the buffer, consistent with an

electroporation mechanism for liposome detection. The rate and quantity of $Fe(CN)_6^{4-}$ released during liposome collision/electroporation was also controlled by buffer osmolarity. Significantly, we found that $[Fe(CN)_6^{4-}]$ in liposomes varies dramatically with buffer osmolarity, consistent with a recent report.[28] We also provide evidence that single liposomes may release a fraction of their contents, i.e., may be detected more than once, as suggested by the Mirkin group.[27]**Error! Bookmark not defined.** We believe this work clarifies detection and loading of redox-filled liposomes, and may be useful for a more complete understanding of electrochemical detection of biological vesicles[29-33] and/or the development of rapid, quantitative techniques for liposome analysis.

5.2 EXPERIMENTAL

5.2.1 Chemicals and Materials

1,2-Dioleoyl-sn-glycero-3-phosphocholine (DOPC, >99%), 1,2-dioleoyl-sn-glycero-3-phosphethanolamine (DOPE, >99%) and cholesterol (ovine wool) were purchased from Avanti Polar Lipids (USA). Potassium chloride (KCl), HEPES (4-(2-hydroxyethyl)-1-piperazineethanesulfonic acid), ferrocenemethanol (FcMeOH), and potassium hexacyanoferrate(II) trihydrate ($K_4Fe(CN)_6$, ferrocyanide) were purchased from Sigma. All aqueous solutions were prepared using 18.2 MΩ cm^{-1} water and adjusted to pH 7.4 using 1 M KOH. All reagents used were reagent grade or better.

5.2.2 Solutions

Experiments were performed in recording buffer (RB) with base recipe: 0.5 M KCl, 10 mM HEPES, pH 7.4. To change the osmolarity of the recording buffer, we made solutions with 0.1-0.7 M KCl, 10 mM HEPES, pH 7.4, corresponding to osmolarities of 0.2-1.4 osmol (Osm) L-1. Note: We assumed 1 Osm L-1 (0.5 M KCl, 10 mM HEPES, pH 7.4) to be isotonic relative to the liposome lumen, which is indicated by the dashed vertical line on several figures.

5.2.3 Liposome Synthesis

Lipids dissolved in chloroform were mixed in a mass ratio of 2:1:1 to obtain a concentration of 9.07 mM DOPC, 4.80 mM DOPE, and 9.24 mM cholesterol before chloroform evaporation as described previously. A thin lipid film was formed by evaporating chloroform under N2 for 30 minutes followed by 2 hours under vacuum dessicator to evaporate any trace organic solvent present in the lipid film. To load liposomes with a redox mediator, the lipid film was hydrated for 1 hour with 2 mL of 500 mM K4Fe(CN)6, 10 mM HEPES, pH 7.4 and vortexed periodically to support mixing. Hydrated lipid solution was extruded through a 200 nm polycarbonate membrane (Whatman) in a mini-extruder (Avanti) 21 times to obtain 200 nm liposomes. The extruded solution was then diluted to a final volume of 30 mL with RB (0.5 M KCl, 10 mM HEPES, pH 7.4) and centrifuged at 16,000 g for 2 hours to obtain a liposome pellet. Pellet was resuspended in 2 mL of 0.5 M KCl, 10 mM HEPES, pH 7.4. Liposomes could be stored at 4 °C for up to 2 days.

5.2.4 Microelectrode Preparation

CFEs were prepared as described previously by aspirating a carbon fiber (5 μm) into a borosilicate glass capillary (1.2 mm o.d., 0.9 mm i.d., Sutter) that was pulled to a fine tip using a P97 pipet puller (Sutter). Microelectrodes were cut and sealed in epoxy (Epoxy Technologies), followed by 2 h at 80 °C and 2 h at 150 °C to cure. CFEs were polished on a home-built micropipette beveler. CFEs were backfilled with 3 M KCl to establish electrical contact. Electrodes were tested with cyclic voltammetry in 1 mM FcMeOH, 100 mM KCl at 100 mV/s vs. Ag/AgCl. Only electrodes with stable i-E curves and good electron-transfer kinetics were used for experiments.

5.2.5 Liposome Collision and Detection

In a typical experiment, the stock suspension of liposomes (suspended in 0.5 M KCl, 10 mM HEPES, pH 7.4) were spiked into a recording buffer of the same or different osmolarity (typically 50× dilution factor). The CFE was immersed in this suspension and poised at E_{app} = +1 V vs. Ag/AgCl unless otherwise indicated.

5.2.6 Data Acquisition and Analysis

Electrodes were held at E_{app} vs. Ag/AgCl using a commercial patch-clamp current amplifier (Axopatch 200B; Axon Instruments). The current was filtered at 2 kHz using an internal low-pass Bessel filter and sampled at 100 kHz using a Digidata 1440 digitizer (Axon Instruments). Amperometric spike characteristics characteristics, including I_{max} (peak amplitude, pA), $t_{1/2}$ (full width of peak at half-maximum, ms), t_{rise} (10−90% max peak height, ms), t_{fall} (90−10% max peak height, ms), and Q (integrated charge, fC) were identified using pClamp v10.6 software (Axon Instruments). Spikes were identified if the I_{max} exceeded 5 times the standard deviation (SD) of the noise. All identified spikes were inspected, and unfit spikes were manually discarded (such as those associated with electrical noise or vibrations). Statistical significance between groups was assessed using the Mann−Whitney−Wilcoxon rank-sum U test (Mann−Whitney) and statistical significance across multiple groups was measured by one-way ANOVA (ANOVA). Statistics are reported as the mean ± SEM (standard error of the mean).

5.2.7 Dynamic Light Scattering

Dynamic light scattering was performed using a Zetasizer Nano ZS (Malvern Instruments) courtesy of the Chiu lab at UW.

5.2.8 Stimulated Raman Scattering (SRS) Microscopy

SRS microscopy is a nonlinear optical imaging technique that uses two ultrashort laser pulses (pump and Stokes) to coherently excite a Raman vibration that has an energy corresponding to the energy difference between the pump and the Stokes pulses. This coherent excitation improves signal intensity by several orders over its spontaneous Raman counterpart.[40] The 200 nm $K_4Fe(CN)_6$-filled liposomes were analyzed with an SRS microscope for the presence of the spectral signature of the nitrile group, which has a strong Raman peak at 2098 cm^{-1} (**Figure S5.9**) within the "silent-region".[41] A 63x magnification Leica microscope objective was used for imaging. In a typical experiment, we imaged 5 fields of view to survey multiple liposomes per osmotic condition. The concentration of each liposome was obtained by correlating the signal with the point spread function of the microscope to account for the spatial resolution limits of the objective. The pump and Stokes pulses had an average power of 40 mW each at the focus.

5.3 Results and Discussion

5.3.1 Redox-Filled Liposomes are Detected Electrochemically via Electroporation

Similar to what has been demonstrated in other works,[22-27] we were able to detect freely diffusing, $K_4Fe(CN)_6$-filled liposomes (~200 nm diameter, **Figure S5.1**) upon collision at a CFE *via* amperometry (**Figure 5.1A**). The frequency of amperometric signals depended on the applied voltage to the CFE (E_{app}), with no signals observed when $E_{app} < +0.4$ V vs. Ag/AgCl; the maximum frequency of signals was observed at $E_{app} = +1$ V, consistent with the cyclic voltammogram (CV) for 5 mM $Fe(CN)_6^{4-}$ (**Figure S5.2**). Liposomes loaded with buffer free of redox molecules could not be detected (**Figure S5.3**). The frequency of signals also depended strongly on the concentration of liposomes in solution; when liposomes were diluted 1000× in buffer (see *Experimental*), we observed signals at a frequency of 0.04 ± 0.01 s^{-1}; at 50×, the signal frequency

was 0.73 ± 0.20 s^{-1} (**Figure S5.4**, **Table S5.1**). Taken together, these observations strongly suggest that the observed amperometric signals are the result of single liposome collisions with the CFE surface and subsequent electrolysis of their contents.

To electrochemically detect redox-filled liposomes, the lipid bilayer separating the internal redox contents from the external solution must open. As suggested previously, the most likely mechanism for liposome or vesicle electrochemical detection is *electroporation*, which we describe as follows (**Figure 5.1B**): *i)* Initially, the internal compartment of liposomes are in a state of equilibrium with the external solution – any differences in the concentration of osmolytes between the liposome lumen and the bulk solution are small enough that the membrane is stable; *ii)* when the liposome encounters the large electric field nanometers from the electrode surface (due to the electrical double layer, ~10^6 V/cm),**Error! Bookmark not defined.**,[34] the lipid membrane b ehaves as a capacitor, as charged species cannot pass through the bilayer; charges accumulate on either side, increasing the transmembrane voltage and subsequently, membrane tension; *iii)* eventually, the tension energy exceeds the limit of the membrane, causing membrane rupture (electroporation) and leakage of internal contents to the electrode surface, where they are detected.[7-9]

5.3.2 Manipulation of Membrane Tension Modifies Liposome Electroporation

It was shown previously that the critical voltage required for electroporation of liposomes depends strongly on the initial membrane tension.[9] Thus, changing the liposome membrane tension should change the favorability of electroporation and subsequently, the frequency of amperometric events. As our stock of liposomes was stored in 0.5 M KCl (1 Osm L^{-1}), we reasoned that liposome membrane tension would change when we exposed liposomes to more hypotonic (0.2-0.9 Osm L^{-1}) or hypertonic (1.1-1.4 Osm L^{-1}) buffers relative to the storage buffer (see

Experimental). Measuring liposome size with DLS confirmed this expectation, with the average diameter of liposomes decreasing from 213 ± 5 nm in 0.2 Osm L^{-1}, to 183 ± 1 nm in 1.4 Osm L^{-1} ($p = 2.4 \times 10^{-7}$, ANOVA), consistent with swelling or shrinking behavior associated with hypotonic or hypertonic conditions, respectively.[35]

When we amperometrically detected liposomes suspended at the same concentration (50×) in different osmolarity buffers, we observed a stark decrease in the frequency of detection events, from 1.40 ± 0.19 s^{-1} in 0.2 Osm L^{-1} to 0.36 ± 0.05 s^{-1} in 1.4 Osm L^{-1} ($p = 3.22 \times 10^{-4}$, ANOVA). The variation of event frequency with osmolarity (*despite* similar particle concentrations) suggested electrochemical detection is more favorable when the liposome membrane is more tense, consistent with electroporation (**Figure 5.2A**, **C**). For examples of single signals, see **Figure S5.5**.

Figure 5.3A shows the average amperometric signal from the oxidation of released $Fe(CN)_6^{4-}$ during liposome collision/electroporation for four selected osmolarities (average peaks at all osmolarities, **Figure S5.6**). Signal shapes shifted from high amplitude with shorter duration at more hypotonic osmolarities (0.2-0.9 Osm L^{-1}) to low amplitude with longer duration at more hypertonic osmolarities (1.0-1.4 Osm L^{-1}), implying that the fluid junction (fusion pore) that forms during electroporation is wider under hypotonic conditions, facilitating faster flux of molecules out of the liposome (detailed peak statistics, **Figure S5.7** and **Table S5.2**).

To quantitatively understand how electroporation behavior changes as a function of osmolarity, we applied procedures outlined by Amatore and Ewing, to calculate the radius of the fusion pore.[25,36] By fitting the falling phase of the average peaks with an exponential decay function (dashed lines, **Figure 5.3A**), we extracted the time constant of decay, τ. The maximum pore radius, R_{pore}, is given by the following relationship:

$$R_{pore} = \frac{R_{lip}^{3}}{D_{lip} \times \tau}$$

where R_{lip} is the radius of the liposome at each osmolarity (extracted from DLS sizing, Figure 5.2B); D_{lip} is the diffusion coefficient of $Fe(CN)_6^{4-}$ within the liposome, which we assumed was identical to its coefficient in bulk ($D_{lip} = 7.2 \times 10^{-6}$ cm^2 s^{-1}).[37] By our calculation, R_{pore} increased as osmolarity decreased, from 0.7 ± 0.2 nm at 1.4 Osm L^{-1} to 4.3 ± 0.6 nm at 0.2 Osm L^{-1} ($p = 2.35 \times 10^{-5}$, ANOVA).

R_{pore} depended strongly on the initial membrane tension, and interestingly, the ratio of R_{pore} to R_{ves} did not remain constant (e.g. 4.0 ± 0.5 % at 0.2 Osm L^{-1}, 0.7 ± 0.2 % at 1.4 Osm L^{-1}, **Table S5.3**). We also note that the magnitude of the difference between the fit and the observed data increased steadily as osmolarity decreased **(Figure S5.8**). This can be readily seen in **Figure 5.3A**, where the single exponential decay fit is in much better agreement with the data for 1.0 or 1.4 Osm L^{-1} than for 0.2 or 0.9 Osm L^{-1}. We speculate that these data suggest a secondary process occurs during electroporation of liposomes at greater initial membrane tension, e.g. a fluctuating fusion pore structure.

5.3.3 Redox Concentration in Liposomes Depends on Osmolarity of the Buffer

Looking at **Figure 5.3A**, it is obvious that peaks were larger in amplitude and longer in duration at 0.9 Osm L^{-1} than at 0.2 Osm L^{-1}, implying that more redox molecules are released from liposomes under this experimental condition. One can quantify the number of molecules ($N_{molecules}$) released per liposome collision/electroporation event using Faraday's equation: $N_{molecules} = Q/nF \times N_A$, where Q is the integrated charge from each amperometric event, n is the number of electrons transferred per molecule (1 e$^-$ for $Fe(CN)_6^{4-}$), F is Faraday's constant (96485 C mol^{-1}),

and N_A is Avogadro's number. When we analyzed the events at each osmolarity, we found surprising non-monotonic behavior, with $N_{molecules}$ per event reaching a maximum of 248,000 ± 17,400 molecules at 0.9 Osm L^{-1}; at the extremes, $N_{molecules}$ = 143,000 ± 8,100 at 0.2 Osm L^{-1} and $N_{molecules}$ = 101,000 ± 13,300 at 1.4 Osm L^{-1} ($p = 2.2 \times 10^{-16}$, ANOVA) (**Figure 5.4A**).

What is the mechanism for this behavior? A recent detailed study from the Rangamani group showed that when GUVs (radius 8, 14, or 20 μm) loaded with 200 mM sucrose were exposed to hypotonic buffer devoid of osmolytes, they initiated "swell-burst" cycles; hypotonic swelling due to H_2O influx increased GUV membrane tension to the point of rupture, permitting solution exchange.[28] Rupture events opened pores with radii as large as ~10 μm (GUV radius 20 μm), which resealed in about 100 ms. Cycles of swelling and bursting continued until the concentration differential between the inside and outside of the GUV was <10 mM.

If swell-burst cycles can also regulate osmolyte concentration in our 200 nm liposomes, then we reasoned that liposomes would release fewer molecules under more hypotonic conditions due to decreased internal $[Fe(CN)_6^{4-}]$. Indeed, from amperometric signals and DLS, we estimated that liposomes contained $[Fe(CN)_6^{4-}]$ = 47.5 ± 1.4 mM at 0.2 Osm L^{-1}, compared to 112 ± 4.2 mM at 0.9 Osm L^{-1}. However, estimated $[Fe(CN)_6^{4-}]$ also decreased under hypertonic conditions (54.4 ± 2.8 mM at 1.4 Osm L^{-1}), when we expected the internal $[Fe(CN)_6^{4-}]$ to be stable (**Figure 5.4B**); this implies that liposome collision/electroporation events do not always result in complete electrolysis of liposome contents.

To more directly probe how liposome $[Fe(CN)_6^{4-}]$ changes in response to osmotic pressure, we used an orthogonal technique, stimulated Raman scattering (SRS) microscopy. SRS microscopy is able to probe liposome contents label-free, by measuring the vibrational signature

of $Fe(CN)_6^{4-}$ and correlating the signal intensity to a known [$Fe(CN)_6^{4-}$] standard (**Figure S5.9**). As expected, SRS revealed that the internal [$Fe(CN)_6^{4-}$] changed significantly with osmolarity, from [$Fe(CN)_6^{4-}$] = 107 ± 12.8 mM at 0.2 Osm L^{-1} to 224 ± 13.2 mM at 1.4 Osm L^{-1} ($p = 5.8 \times 10^{-15}$, ANOVA).

Assuming the SRS determination of [$Fe(CN)_6^{4-}$] in liposomes to be ground truth, amperometry detected 44.2 ± 1.5 % of the total contents at 0.2 Osm L^{-1}, which decreased to only 23.2 ± 1.8 % at 1.4 Osm L^{-1} (**Table S5.4**). Consequently, we believe liposomes can release a fraction of their total contents during electroporation, the magnitude of which depends on the initial membrane tension on the liposome.

5.3.4 Multipeak Detection of Single Liposomes

If liposomes can release a fraction of their total contents during electroporation, it stands to reason that liposomes may sometimes be detected multiple times, as was recently suggested by the Mirkin group.[27] Consistent with this hypothesis, we observed high frequency barrages of amperometric signals that far exceeded the expected rate, similar to what our group observed with Ag nanoparticle collision (**Figure 5.5**).[38] To capture this behavior quantitatively, we diluted liposomes 1000× in buffers ranging from 0.2-1.0 Osm L^{-1} (more hypertonic conditions gave rise to extremely low detection frequencies, data not shown) and recorded liposome collisions for 10 minutes. The Poisson probability that each amperometric event occurred due to an independent particle collision is given by:

$$\boldsymbol{P(t) = \frac{rt^k e^{-rt}}{k!}}$$

where t is the arbitrary time interval (s), r is the overall frequency of events (s^{-1}), and k is the number of events occurring during the time interval.

Figure 5.5 shows selected traces featuring multipeak behavior with $P(t)$ calculated manually. We observed as many as 13 events in 1.48 s ($r = 0.213\ s^{-1}$ for this trace) for a calculated $P(t) = 1.16 \times 10^{-11}$ that these were due to 13 independent particles. One can automate this analysis by setting t to the interspike interval[39] and k = 2; then, each event is associated with a Poisson probability, P. Interestingly, we found a population of events that occurred frequently though their calculated Poisson probability was low ($P < 1 \times 10^{-4}$). Their prevalence at all osmolarities tested was ~25% though the expected incidence was only 0.5% based on simulation (**Figure S5.10**, **Table S5.5**). We did not observe a statistically significant difference between probability distributions depending on osmolarity (p = 0.397, ANOVA). For a more detailed discussion of the statistical basis for classifying multipeak behavior, see **Supplementary Note 5.1**.

We believe that these low probability signals correspond to multiple detections of a single liposome. Liposomes do not appear to release their entire contents during electroporation (Figure 5.4). These low probability signals do not depend on osmolarity, implying that multipeak behavior arises through a separate mechanism. It is possible that multipeak behavior may be related to multilamellarity, which has been observed in liposomes synthesized under similar conditions.[40] It is also possible that multipeak events arise due to collision of aggregates of multiple liposomes. We plan to study this phenomenon in greater detail in a future work.

5.4 CONCLUSION

In conclusion, we used amperometry to study single, 200 nm liposomes loaded with redox molecules. We found the liposome detection frequency depended strongly on the liposome membrane tension, consistent with detection *via* electroporation. The size of the fusion pore that formed during liposome electroporation also depended on membrane tension, with tense membrane conditions favoring wider fusion pores.

Critically, the concentration of redox molecules inside liposomes was regulated by the osmolarity of the external solution, confirmed by both amperometry and SRS. We suspect that this dynamic control of liposome contents is related to "swell-burst cycles," a phenomenon observed in GUVs. The disparity between the concentration estimates from amperometry and SRS support that liposomes only release a fraction of their contents during electroporation, i.e. they may open and close more than once. We provide statistical evidence for such "multipeak" behavior. This study improves the understanding of how liposomes accumulate molecules and release them during electroporation, which may be relevant to vesicle analysis or the development of rapid, quantitative techniques for characterizing liposomes.

5.5 Tables, Figures, and Supplementary Notes

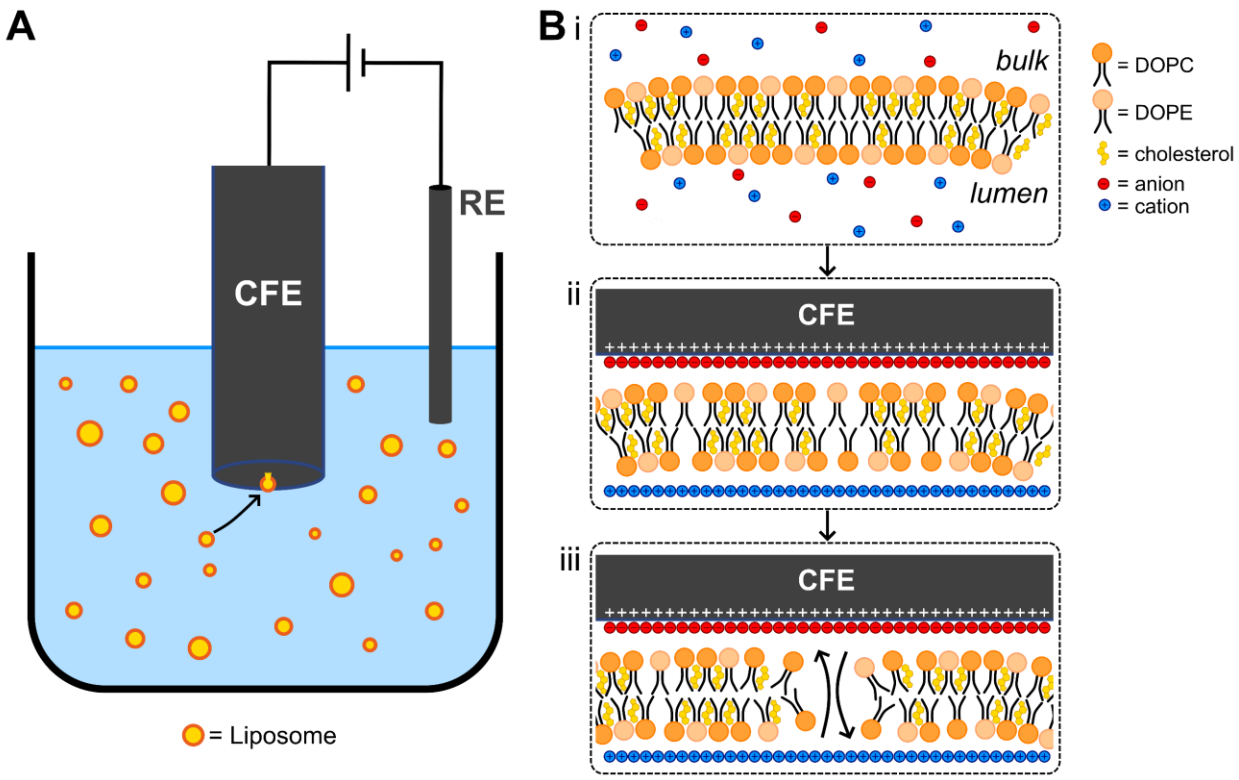

Figure 5.1. Electrochemical detection of redox-filled liposomes. A) Cartoon depicting liposome detection via amperometry. A redox-filled liposome diffuses to the CFE surface, where it is electroporated and leaks its contents to the electrode for detection. B) Mechanism for electrochemical detection of liposomes via electroporation. i) Initially, the lipid bilayer separating the liposome contents (lumen) from the external solution (bulk) is in a state of equilibrium. ii) The liposome encounters the electrode surface (positively biased). Charging of the bilayer membrane occurs, increasing membrane tension. iii) Membrane tension reaches a critical point and the membrane ruptures (electroporation), permitting solution exchange and electrochemical detection of liposome contents.

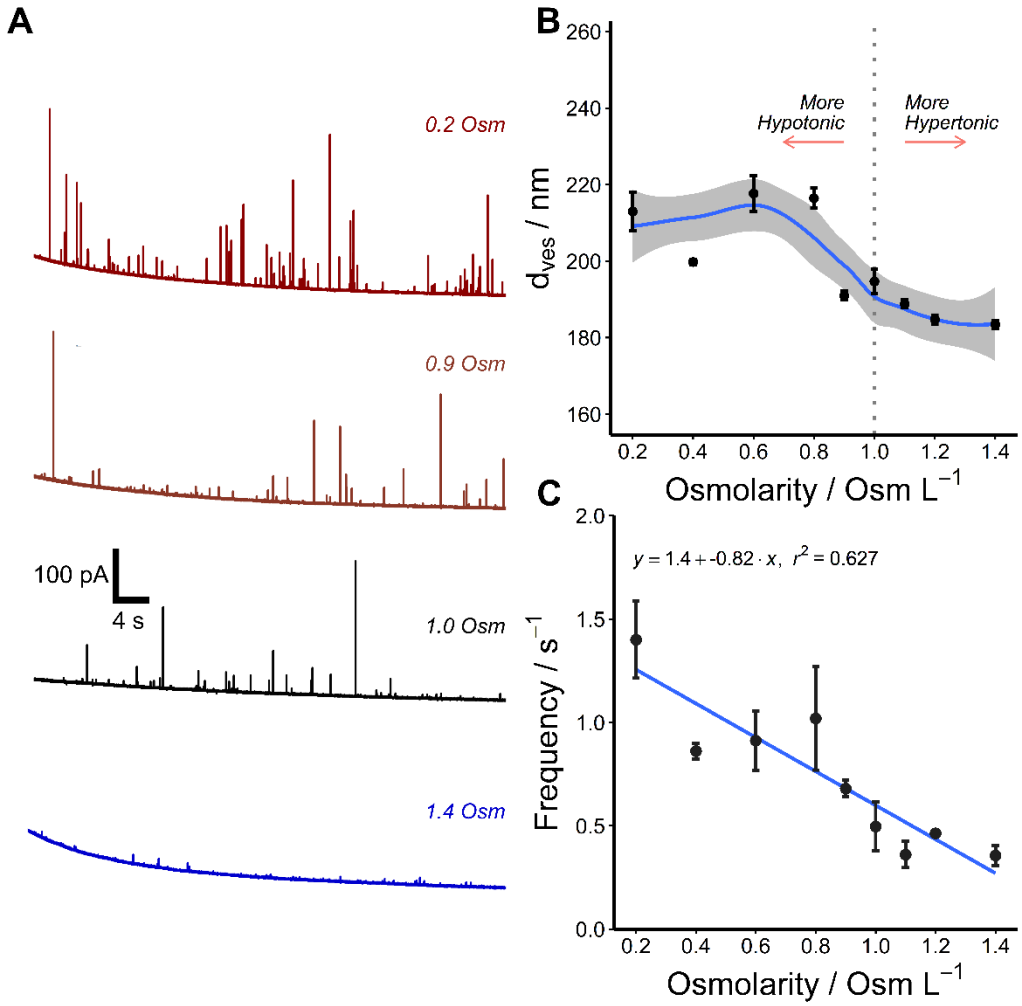

Figure 5.2. Membrane tension modifies liposome detection. *A)* Example amperometric traces for liposomes suspended in four different osmolarity buffers (E_{app} = +1 V vs. Ag/AgCl). *B)* Using DLS, we determined the average diameter (d_{ves}) of liposomes suspended in different osmolarity buffers. The blue curve is a local regression line (grey shading is SEM) to guide the eye. $p = 2.4 \times 10^{-7}$, ANOVA. *C)* Amperometric detection frequency depended strongly on the osmolarity of the buffer. A linear fit is used to guide the eye. Liposomes were spiked into different osmolarity buffers at a 50× dilution factor. $p = 3.22 \times 10^{-4}$, ANOVA.

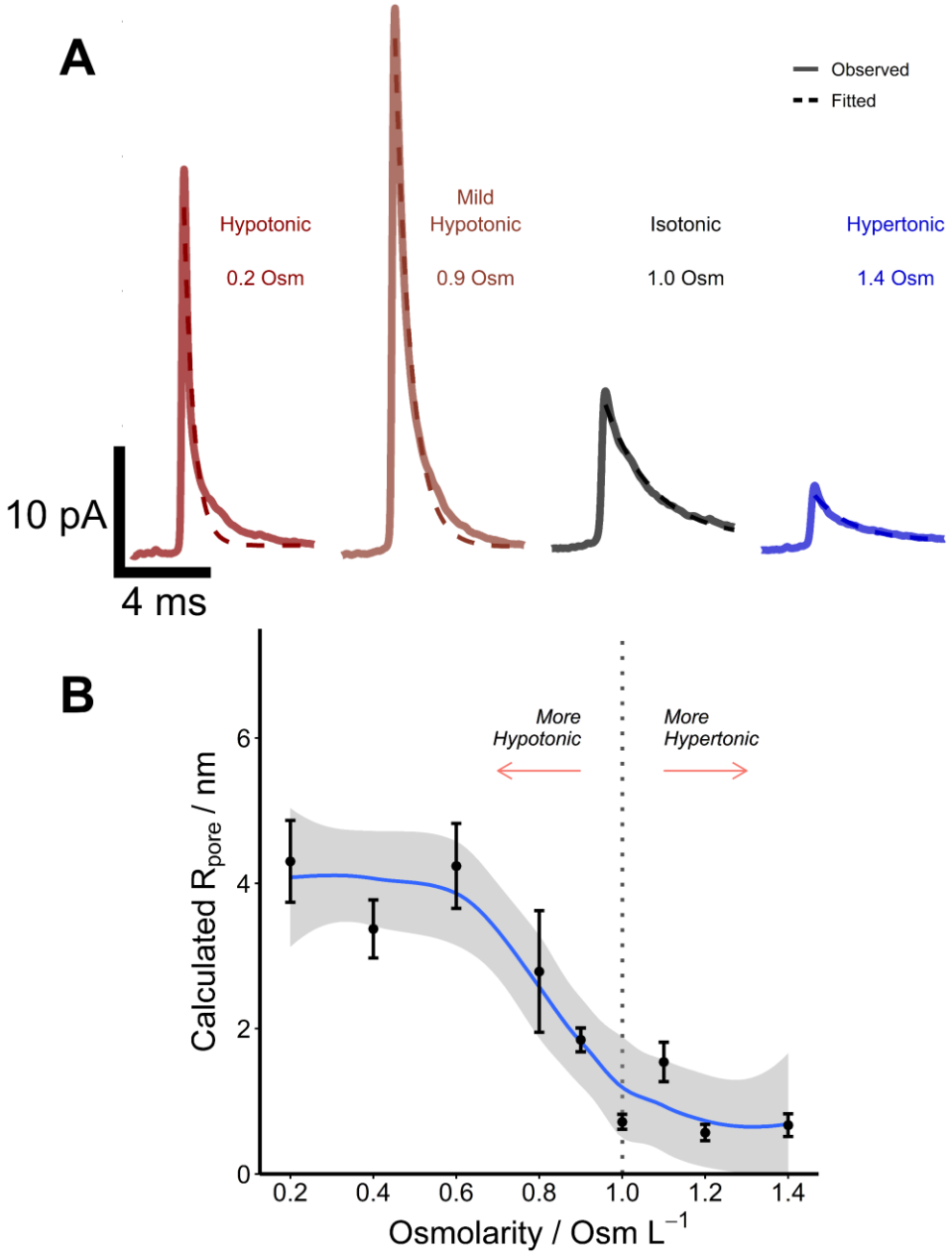

Figure 5.3. Membrane tension controls peak shape, size of the fusion pore. *A)* Average peaks from liposome detections in four different osmolarity buffers (here, Osm is Osm L^{-1}). A single exponential decay fit is overlaid with a dashed line. *B)* From the time constant, τ, of the exponential decay fit, we can calculate the radius of the fusion pore during electroporation, R_{pore} (see text). R_{pore} is the average of three measurements at each osmolarity. The blue curve is a local regression line (grey shading is SEM) to guide the eye. $p = 2.35 \times 10^{-5}$, ANOVA.

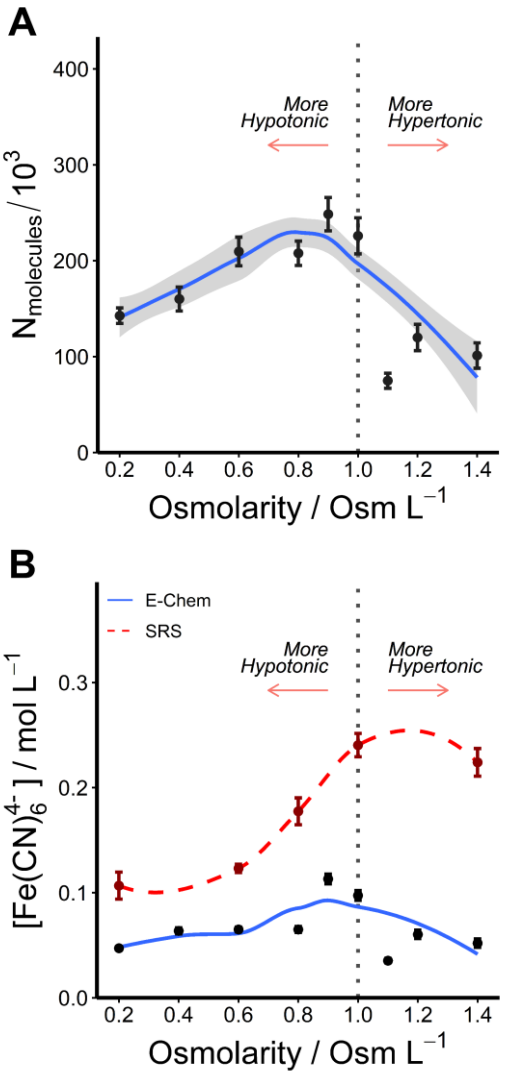

Figure 5.4. Osmolarity controls liposome redox concentration. *A)* Scatter plot of the $N_{molecules}$ detected per amperometric event from liposomes suspended in different osmolarity buffers. The blue curve (grey shading is SEM) is a local regression line which guides the eye to the non-monotonic behavior of $Fe(CN)_6^{4-}$ release. $p = 2.2 \times 10^{-16}$, ANOVA. *B)* Scatter plot of estimated $[Fe(CN)_6^{4-}]$ per liposome based on electrochemical detection (E-Chem) or stimulated Raman scattering (SRS). The blue curve (E-Chem) and dashed red curve are local regression lines (SEM omitted) to guide the eye. For E-Chem, $p = 2.2\times 10^{-16}$, ANOVA. For SRS, $p = 5.8 \times 10^{-15}$, ANOVA.

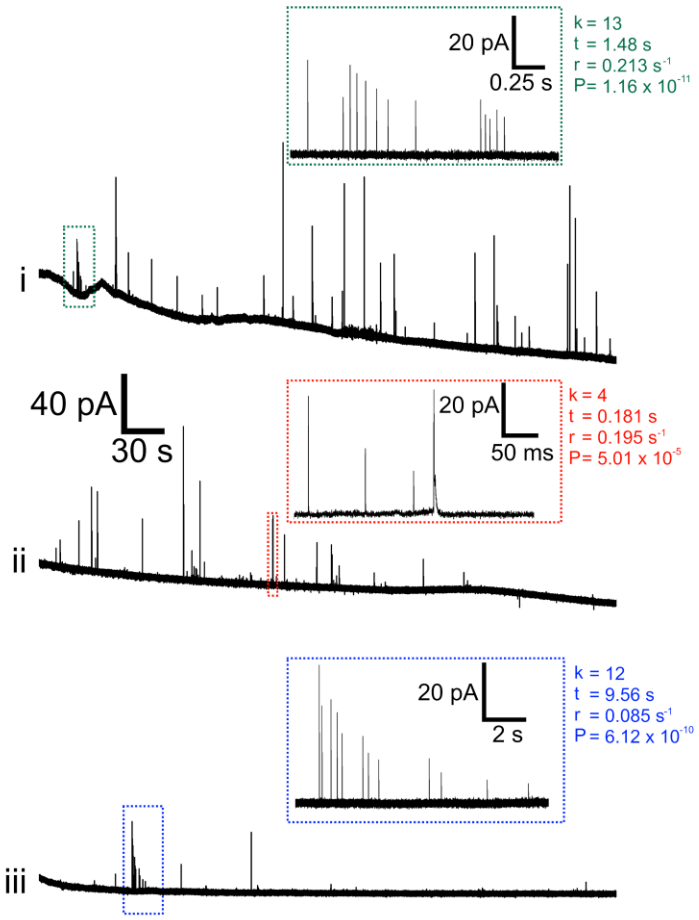

Figure 5.5. Multipeak behavior in redox-filled liposomes. *A)* Amperometric traces showing multipeak behavior. Insets show selected high frequency bursts of events, with corresponding calculations of Poisson probability, *P*. *k* is the number of events, *t* is the time window in the inset, and *r* is the overall frequency of events for the entire trace. Experiment conditions for traces *i*: 0.6 Osm L^{-1}, *ii*: 0.8 Osm L^{-1}, *iii*: 1.0 Osm L^{-1}.

Dilution Factor	[Particles] / (Dilution Factor)$^{-1}$	Frequency (s^{-1})
50x	0.02	0.726 ± 0.195
100x	0.01	0.393 ± 0.037
500x	0.002	0.098 ± 0.022
1000x	0.001	0.044 ± 0.012

Table S5.1. Dependence of amperometric signal frequency on particle concentration. Liposomes were spiked into 0.5 M KCl and amperometric signals were recorded for several minutes (E_{app} = +1 V vs Ag/AgCl). Signal frequency depended strongly on particle concentration, expressed here as the (dilution factor)$^{-1}$.

Osmol L^{-1}	*N_{events}*	*I_{max} (pA)*	*$t_{1/2}$ (ms)*	*t_{rise} (ms)*	*t_{fall} (ms)*
0.2	507	34.7 ± 1.7	0.44 ± 0.02	0.25 ± 0.02	1.19 ± 0.06
0.4	311	42.5 ± 2.9	0.40 ± 0.02	0.24 ± 0.03	1.05 ± 0.07
0.6	320	49.0 ± 3.0	0.47 ± 0.02	0.25 ± 0.03	1.19 ± 0.07
0.8	453	41.6 ± 2.2	0.59 ± 0.03	0.31 ± 0.02	1.42 ± 0.07
0.9	309	51.4 ± 3.2	0.54 ± 0.03	0.28 ± 0.03	1.25 ± 0.08
1.0	264	22.5 ± 1.7	1.06 ± 0.06	0.68 ± 0.07	2.22 ± 0.15
1.1	128	11.5 ± 1.3	0.74 ± 0.07	0.42 ± 0.06	1.59 ± 0.16
1.2	140	9.3 ± 0.9	1.07 ± 0.10	1.01 ± 0.15	2.64 ± 0.28
1.4	135	8.7 ± 1.0	1.01 ± 0.09	0.77 ± 0.07	2.47 ± 0.38
ANOVA (p =)	--	2.2×10^{-16}	2.2×10^{-16}	2.2×10^{-16}	2.2×10^{-16}

Table S5.2. Peak characteristics as a function of osmolarity. Events were analyzed for the maximum amplitude (I_{max}), duration ($t_{1/2}$), rise time (t_{rise}), and fall time (t_{fall}). The number of events collected at each condition are given as N_{events}. Bottom row is one-way ANOVA across the dataset by osmolarity. $p < 0.0001$ is considered very significant statistically.

Osmol L^{-1}	*d_{ves} (nm)*	*R_{pore} (nm)*	*% (R_{pore}/R_{ves})*
0.2	213 ± 5.1	4.3 ± 0.6	4.0 ± 0.5
0.4	200 ± 0.7	3.4 ± 0.4	3.4 ± 0.4
0.6	218 ± 4.7	4.2 ± 0.6	3.9 ± 0.6
0.8	216 ± 2.7	2.8 ± 0.8	2.6 ± 0.8
0.9	191 ± 1.1	1.9 ± 0.2	1.9 ± 0.2
1.0	195 ± 3.2	0.7 ± 0.1	0.7 ± 0.1
1.1	189 ± 1.1	1.5 ± 0.3	1.6 ± 0.3
1.2	185 ± 1.2	0.6 ± 0.1	0.6 ± 0.1
1.4	183 ± 1.0	0.7 ± 0.2	0.7 ± 0.2
ANOVA (p =)	2.4×10^{-7}	2.4×10^{-5}	4.0×10^{-5}

Table S5.3. R_{pore} as a function of osmolarity. From the exponential decay fit from averaged peaks, we extracted R_{pore} by combining the data with the DLS measurement (d_{ves}). R_{pore}/R_{ves} *100% gives the percentage of the vesicle radius that the pore represents. Bottom row is one-way ANOVA across the dataset by osmolarity. $p < 0.0001$ is considered very significant statistically.

Osmol L^{-1}	*$[Fe(CN)_6^{4-}]$ by E-Chem (mmol L^{-1})*	*$[Fe(CN)_6^{4-}]$ by SRS (mmol L^{-1})*	*% (E-Chem/SRS)*
0.2	47.5 ± 1.4	107 ± 12.8	44.6 ± 1.3
0.4	63.9 ± 2.6	-	-
0.6	65.1 ± 2.1	123 ± 3.9	52.8 ± 1.7
0.8	65.7 ± 2.4	177 ± 12.7	37.0 ± 1.3
0.9	112 ± 4.2	-	-
1.0	95.6 ± 3.5	240 ± 11.1	39.8 ± 1.4
1.1	37.8 ± 1.9	-	-
1.2	63.1 ± 3.2	-	-
1.4	54.4 ± 2.8	224 ± 13.2	24.3 ± 1.2
ANOVA (p =)	2.2×10^{-16}	5.8×10^{-15}	2.2×10^{-16}

Table S5.4. Estimated $[Fe(CN)_6^{4-}]$ inside liposomes as a function of osmolarity, as measured by electrochemistry and stimulated Raman scattering (SRS). Bottom row is one-way ANOVA across the dataset by osmolarity.

$p < 0.0001$ is considered very significant statistically.

Osmol L^{-1}	*Frequency (s^{-1})*	*Interspike Interval (s)*	*Expected Multipeaks (%)*	*Observed Multipeaks (%)*
0.2	0.075 ± 0.002	16.7 ± 2.1	0.46	23.3
0.4	0.167 ± 0.004	8.1 ± 0.6	0.65	24.0
0.6	0.148 ± 0.002	7.5 ± 0.6	0.5	26.2
0.8	0.098 ± 0.004	15.1 ± 2.5	0.28	23.6
1.0	0.068 ± 0.002	14.6 ± 1.7	0.61	32.1
ANOVA (p =)	0.0851	3.7×10^{-9}	--	--

Table S5.5. Poisson Analysis. Liposome collisions were carried out by spiking 1000× diluted liposomes into buffers of different osmolarity. The frequency (s^{-1}, overall rate, r), and interspike interval (s) is tabulated as a function of osmolarity, mean ± SEM. By simulating a normal distribution based on the average and standard deviation of the interspike interval at each osmolarity, we simulated the expected Poisson probabilities for each sample. As the bimodal distributions (Figure S5.10) observed for the experimental data had a second population starting near $P(t) = 1 \times 10^{-4}$, we classified events with probabilities lower than this cutoff value as a "Multipeak". After classification, we estimated the percentage of "Expected Multipeaks" (based on the simulated normal distribution of interspike intervals) and "Observed Multipeaks" (based on the experimental data). For a more details, see Supplementary Note 5.1.

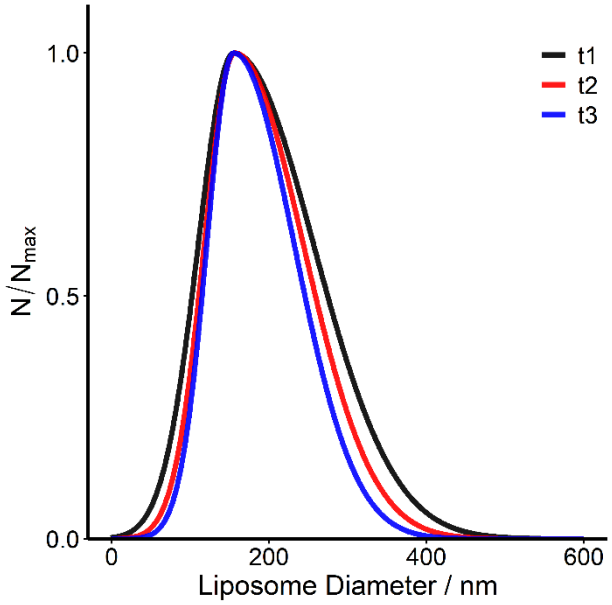

Figure S5.14. Dynamic Light Scattering (DLS) sizing of liposomes. Liposomes were suspended in 500 mM KCl, 10 mM HEPES, pH 7.4 at a concentration of 1000x (dilution factor). Three trials are shown, t1, t2, and t3. The mean liposome diameter, d_{ves}, was 200 nm, 195 nm, and 189.1 nm respectively. The polydispersity index, PDI, was 0.143, 0.111, and 0.092, respectively.

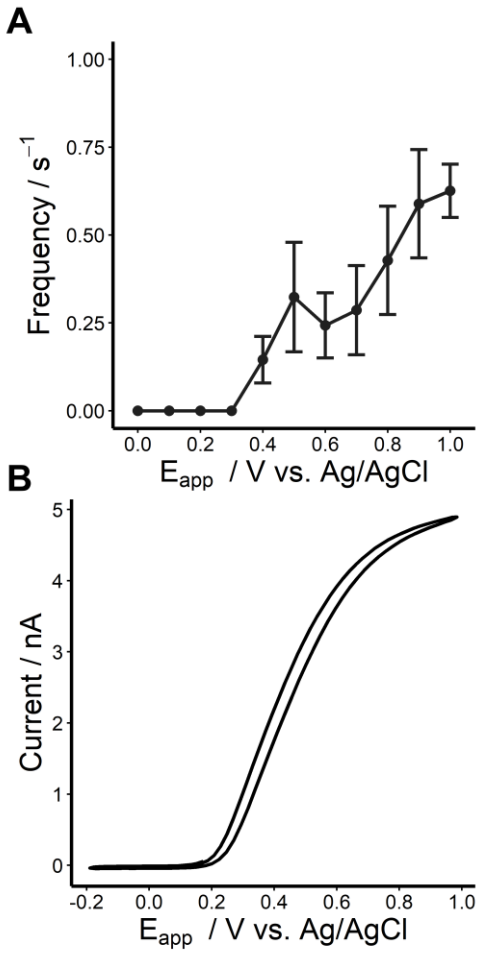

Figure S5.15. Voltage dependence of amperometric signals agrees with CV for 5 mM $Fe(CN)_6^{4-}$. A) Amperometric event frequency depends on applied potential, E_{app}. B) Cyclic voltammogram for a 5 µm carbon-fiber microelectrode (CFE) in 5 mM $K_4Fe(CN)_6$, 100 mM KCl, at 100 mV s^{-1} vs. Ag/AgCl.

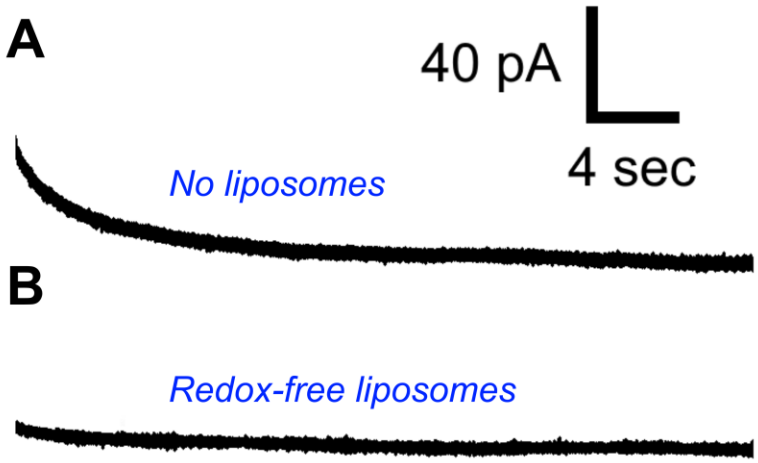

Figure S5.3. Negative controls. A) No amperometric signals are observed in the absence of liposomes. B) No amperometric signals are observed when liposomes are synthesized in the absence of redox molecules.

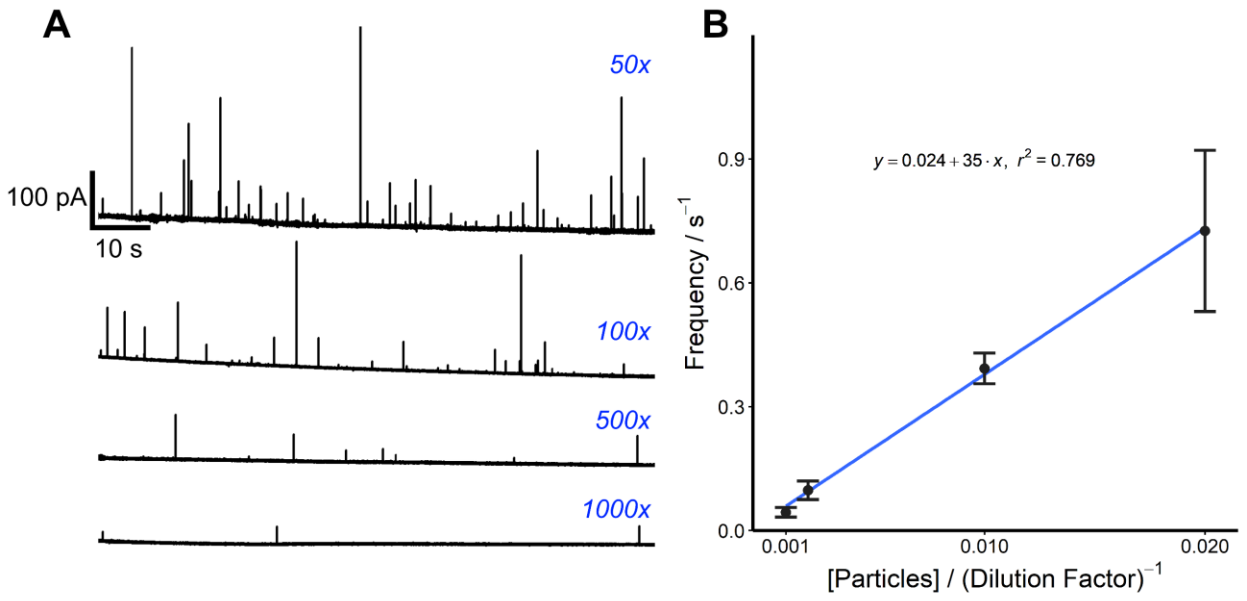

Figure S5.4. Amperometric signal frequency depends on liposome particle concentration. A) Example amperometric traces at 4 different dilution factors, 50, 100, 500, and 1000x (diluted in 0.5 M KCl, 10 mM HEPES, pH 7.4). B) Frequency vs [Particles], where [Particles] is expressed as (dilution factor)$^{-1}$, e.g. 50x = 0.02. Blue line is a linear fit, with indicated equation and R^2 value.

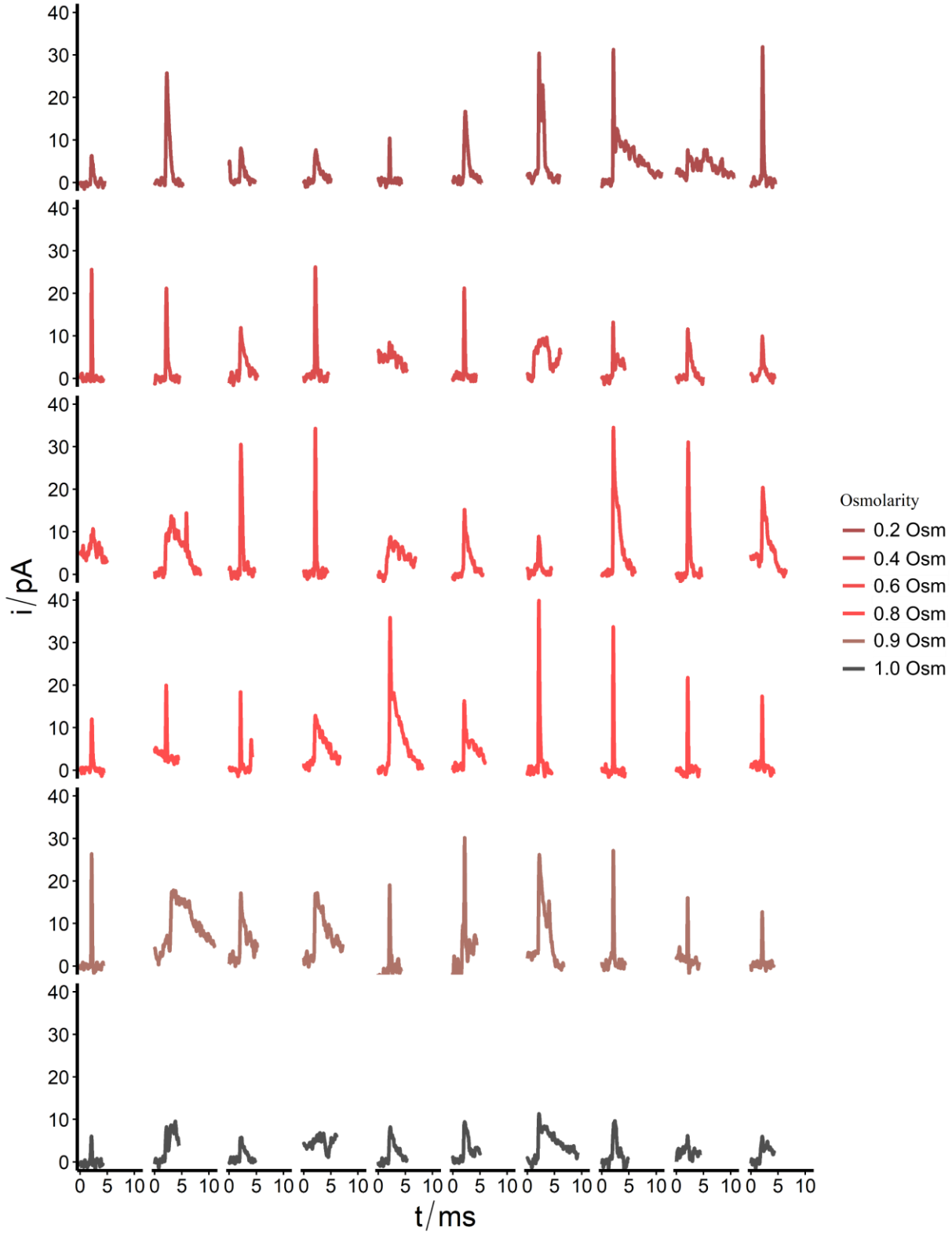

Figure S5.5. Example amperometric signals for osmolarities 0.2 – 1.0 Osm L-1.

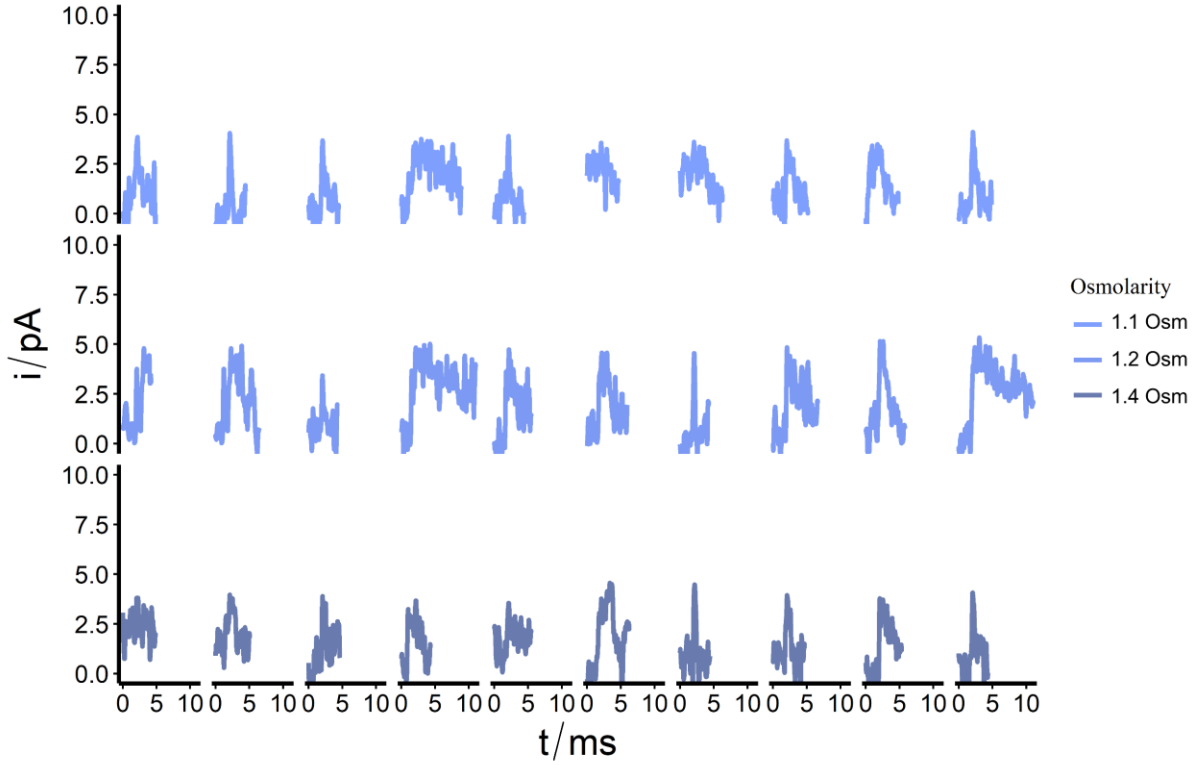

Figure S5.5. (con't) Example amperometric signals for osmolarities 1.1 – 1.4 Osm L-1.

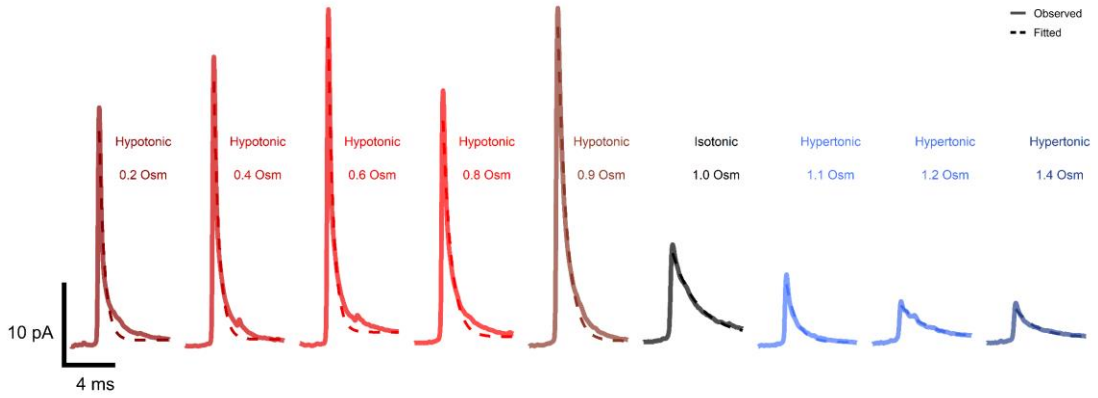

Figure S5.6. Average peaks and exponential decay fits for all osmolarities. Note that the quality of the fit improves with increasing osmolarity.

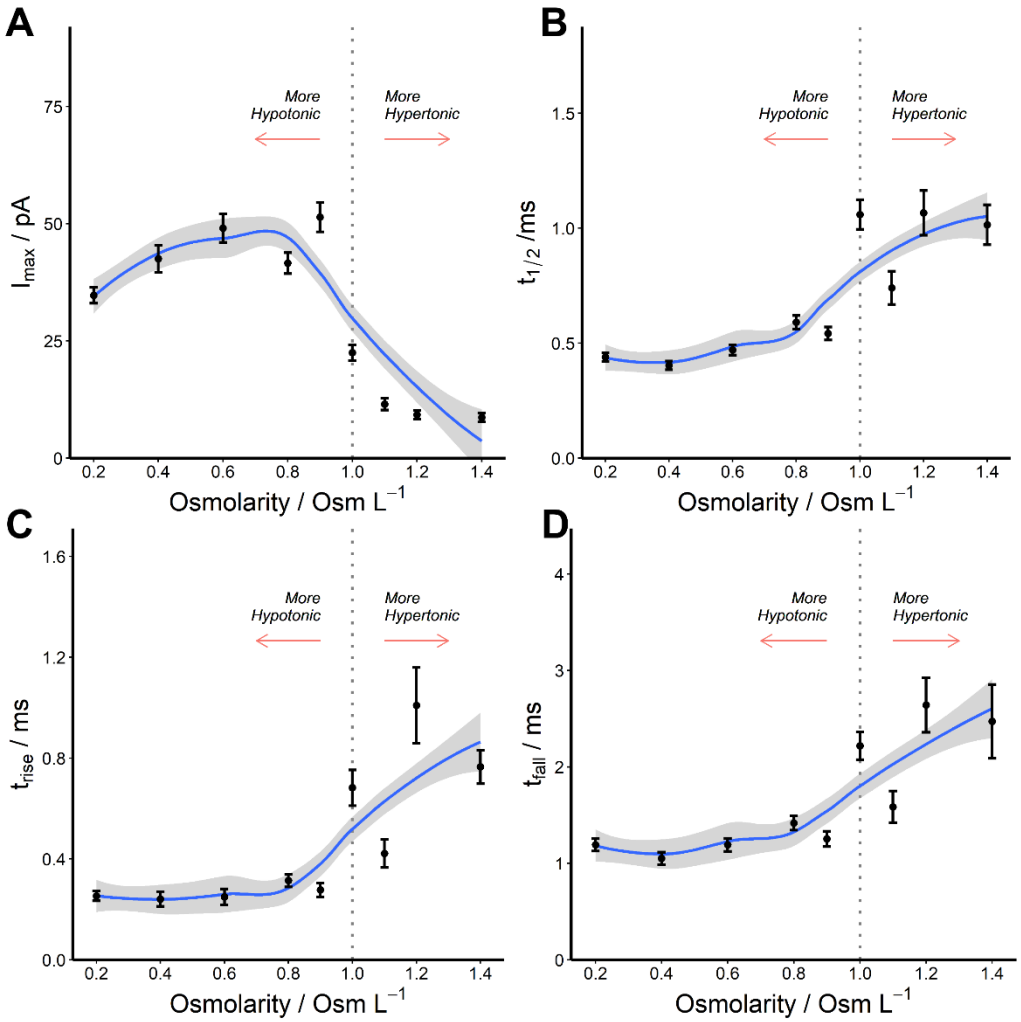

Figure S5.7. Peak characteristics as a function of osmolarity. *A)* Scatter plot of I_{max} vs Osmolarity of the buffer. *B)* Scatter plot of $t_{1/2}$ vs Osmolarity of the buffer. *C)* Scatter plot of t_{rise} vs the Osmolarity of the buffer. *D)* Scatter plot of t_{fall} vs osmolarity of the buffer. For all plots, blue curve is a local regression line to guide the eye to the trend (grey shading is SEM). Taken together, the trends suggest that 1) pores must be larger at lower osmolarity (higher flux of molecules given by I_{max}); and 2) pores take longer to open to their maximum size and stay open longer as osmolarity increases (given by $t_{1/2}$, t_{rise}, and t_{fall}).

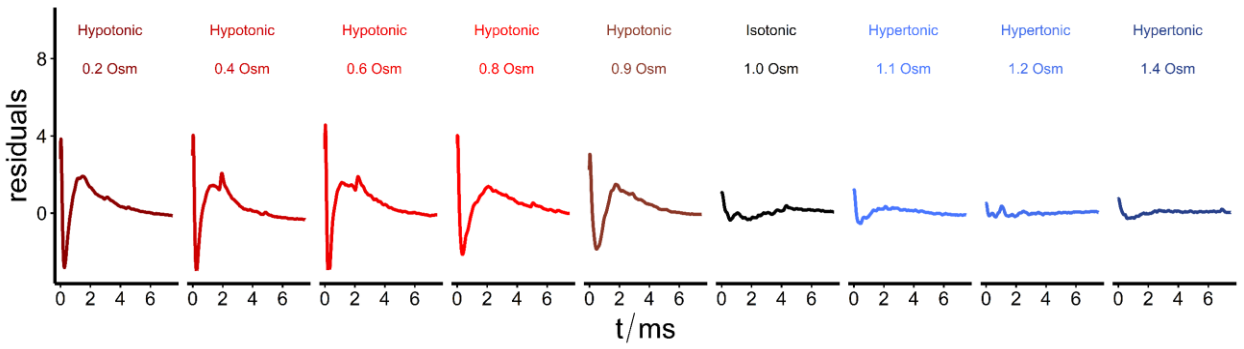

Figure S5.8. Plot of peak residuals vs. time for the average peak fits shows a dependence of goodness-of-fit on osmolarity. The magnitude of the residuals decreased with osmolarity, i.e. the exponential decay function better described the average peaks as osmolarity increased. We concluded that under hypotonic conditions, there may be a secondary process that causes amperometric events to deviate from a pure diffusion case.

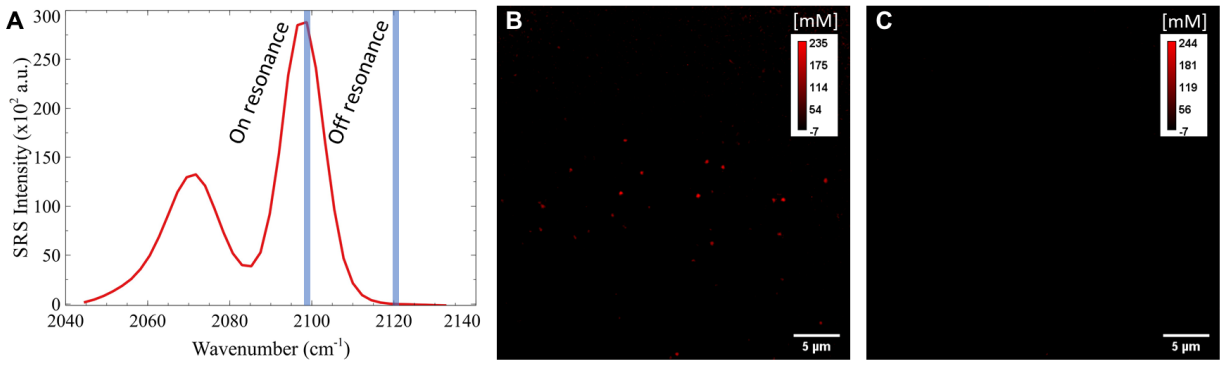

Figure S5.9. Stimulated raman spectroscopy (SRS) of K4Fe(CN)6-loaded liposomes. A) SRS spectrum of 500 mM $K_4Fe(CN)_6$. B) On-resonance (2098 cm^{-1}) and C) off-resonance (2120 cm^{-1}) SRS image of 200 nm, $K_4Fe(CN)_6$-loaded liposomes suspended in a solution of 300 mM KCl.

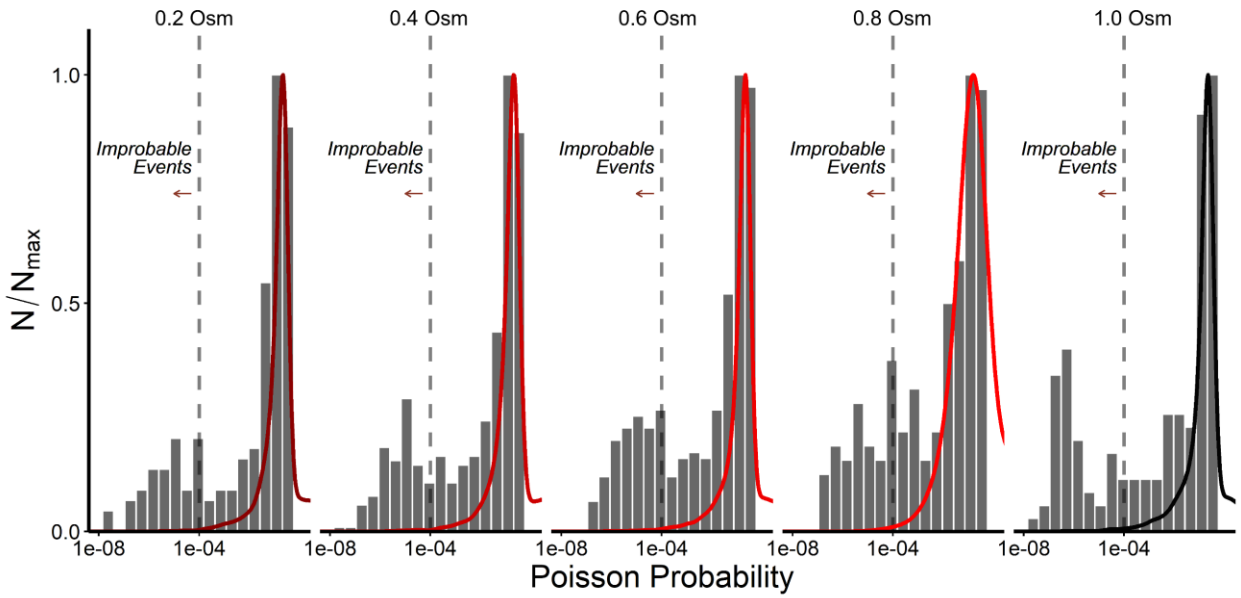

Figure S5.10. Observed and simulated Poisson probabilities for each amperometric event recorded at 5 different osmolarity conditions, liposomes diluted 1000×. The simulated distribution (solid line) is calculated as follows: 1) The observed interspike intervals from each osmolarity are tabulated. 2) The mean and standard deviation for the interspike interval is recorded. These values are used to calculate a normal distribution of simulated interspike intervals (10,000 values). 3) The generated distribution of interspike intervals can then be piped into the Poisson equation, using the observed event frequencies from each osmolarity as the rate, *r*.

By overlaying the simulated Poisson analysis with the observed Poisson analysis, we see a population of low probability events (to the left of $P(t) = 1 \times 10^{-4}$) that occur with unexpected frequency. We classify these events as "Multipeaks" (**Table S5.5**, **Supplementary Note 5.1**).

Supplementary Note 5.1. Here we describe the Poisson analysis presented in **Figure 5.5**, **Table S5.5**, and **Figure S5.10** in the present document.

One can estimate the probability that a number of amperometric events, *k*, are due to independent particle collisions using the equation for Poisson probability, *P(t)*:

$$\boldsymbol{P(t) = \frac{rt^k e^{-rt}}{k!}}$$

where *t* is an arbitrary time interval (s) and *r* is the overall rate of events (s^{-1}). We showed that this formula is functional for manual calculation of P(t) for arbitrary *t* and *k* (Figure 5.5). However, to better understand liposome collision/electroporation behavior at scale, it is desirable to automate this Poisson analysis. To do this, we calculated a parameter called the interspike interval (see the graphic below):

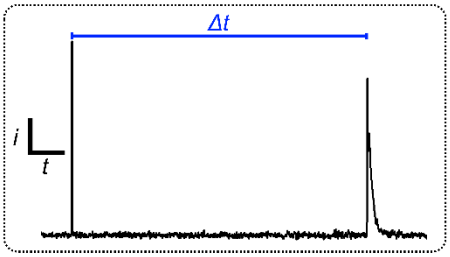

The interspike interval (*Δt*) is simply the time lag between an event and the event that preceded it. Thus, each event (other than the first event in a series) has a *Δt* associated with it. Then, by setting k = 2 (there are two events that occur in every interspike interval, *Δt*) and tabulating the overall event rate, *r*, for each trace, we can calculate the Poisson probability, *P(t)*, for every event in the data set. As one can observe from Figure S5.10, there is a significant population of events with very low Poisson probability ($P < 1 \times 10^{-4}$). To understand whether this population of events

is remarkable, we simulated the expected distribution of Poisson probabilities for each dataset through the following procedure.

1. We calculated a normal distribution of 10,000 Δt based on the observed mean (μ) and standard deviation (σ) of Δt for each osmolarity.
2. We applied our Poisson analysis method to the simulated dataset.
3. We compared the % of events with $P < 1 \times 10^{-4}$ from the Observed vs Simulated distributions (Table S5.5).

Taken together, we concluded that multipeak behavior in liposomes is likely, and may partly explain sub-quantitative detection.

5.6 REFERENCES

(1) Sezgin, E.; Kaiser, H. J.; Baumgart, T.; Schwille, P.; Simons, K.; Levental, I. "Elucidating membrane structure and protein behavior using giant plasma membrane vesicles." *Nat. Protocols*, **2012**, *7*, 1042–1051.

(2) Baumgart, T.; Hammond, A. T.; Sengupta, P.; Hess, S. T.; Holowka, D. A.; Baird, B. A.; Webb, W. W. "Large-scale fluid/fluid phase separation of proteins and lipids in giant plasma membrane vesicles." *Proc. Nat. Acad. Sci.*, **2007**, *104*, 3165–3170.

(3) Cornell, C. E.; McCarthy, N. L. C.; Levental, K. R.; Levental, I.; Brooks, N. J.; Keller, S. L. "n-Alcohol Length Governs Shift in Lo-Ld Mixing Temperatures in Synthetic and Cell-Derived Membranes." *Biophysical Journal*, **2017**, *113*, 1200–1211.

(4) Cornell, C. E.; Skinkle, A. D.; He, S.; Levental, I.; Levental, K. R.; Keller, S. L. "Tuning Length Scales of Small Domains in Cell-Derived Membranes and Synthetic Model Membranes." *Biophys. J.*, **2018**, *115*, 690–701.

(5) Kahya, N.; Scherfeld, D.; Bacia, K.; Schwille, P. "Lipid domain formation and dynamics in giant unilamellar vesicles explored by fluorescence correlation spectroscopy." *J. Struct. Biol.*, **2004**, *147*, 77–89.

(6) Lingwood, D. & Simons, K. "Lipid rafts as a membrane-organizing principle." *Science*, **2010**, *327*, 46–50.

(7) Dimova, R.; Riske, K. A.; Aranda, S.; Bezlyepkina, N.; Knorr, R. L.; Lipowsky, R. "Giant vesicles in electric fields." *Soft Matter*, **2007**, *3*, 817–827.

(8) Dimova, R.; Bezlyepkina, N.; Jordö, M. D.; Knorr, R. L., Riske, K. A.; Staykova, M.; Vlahovska, P. M.; Yamamoto, T.; Yang, P.; Lipowsky, R. "Vesicles in electric fields: Some novel aspects of membrane behavior." *Soft Matter*, **2009**, *5*, 3201–3212.

(9) Riske, K. A. & Dimova, R. "Electro-deformation and poration of giant vesicles viewed with high temporal resolution." *Biophys. J.*, **2005**, *88*, 1143–1155.

(10) Jahn, R.; Lang, T.; Südhof, T. C. "Membrane fusion." *Cell*, **2003**, *112*, 519–533.

(11) Kliesch, T. T.; Dietz, J.; Turco, L.; Halder, P.; Polo, E.; Tarantola, M.; Jahn, R.; Janshoff, A. "Membrane tension increases fusion efficiency of model membranes in the presence of SNAREs." *Sci. Rep.*, **2017**, *7*, 1–13.

(12) Witkowska, A., & Jahn, R. "Rapid SNARE-Mediated Fusion of Liposomes and Chromaffin Granules with Giant Unilamellar Vesicles." *Biophys. J.*, **2017**, *113*, 1251–1259.

(13) Mühlenbrock, P.; Herwig, K.; Vuong, L.; Mey, I.; Steinem, C. "Fusion Pore Formation Observed during SNARE-Mediated Vesicle Fusion with Pore-Spanning Membranes." *Biophys. J.*, **2020**, *119*, 151–161.

(14) Mosharov, E. V. & Sulzer, D. "Analysis of single-vesicle exocytotic events recorded by amperometry." *Nat. Methods*, **2008**, *2*, 651–658.

(15) Hellberg, D.; Scholz, F.; Schauer, F.; Weitschies, W. “Bursting and spreading of liposomes on the surface of a static mercury drop electrode.” *Electrochem. Comm.* **2002**, *4*, 305–309.

(16) Hellberg, D.; Scholz, F.; Schubert, F.; Lovrić, M.; Omanović, D.; Hernández, V. A.; Thede, R. “Kinetics of liposome adhesion on a mercury electrode.” *J. Phys. Chem. B*, **2005**, *109*, 14715–14726.

(17) Liu, Y.; Xu, C.; Yu, P.; Chen, X.; Wang, J.; Mao, L. “Counting and Sizing of Single Vesicles/Liposomes by Electrochemical Events.” *ChemElectroChem*, **2018**, *5*, 2954–2962.

(18) Plant, A. L.; Gueguetchkeri, M.; Yap, W. “Supported phospholipid/alkanethiol biomimetic membranes: insulating properties.” *Biophys. J.*, **1994**, *67*, 1126–1133.

(19) Wilburn, J. P.; Wright, D. W.; Cliffel, D. E. “Imaging of voltage-gated alamethicin pores in a reconstituted bilayer lipid membrane via scanning electrochemical microscopy.” *Analyst*, **2006**, *131*, 311–316.

(20) Campos, R. & Kataky, R. “Electron transport in supported and tethered lipid bilayers modified with bioelectroactive molecules.” *J. Phys. Chem. B*, **2012**, *116*, 3909–3917.

(21) Schmallegger, M.; Barbon, A.; Bortolus, M.; Chemelli, A.; Bilkis, I.; Gescheidt, G.; Weiner, L. “Systematic Quantification of Electron Transfer in a Bare Phospholipid Membrane Using Nitroxide-Labeled Stearic Acids: Distance Dependence, Kinetics, and Activation Parameters.” *Langmuir*, **2020**, *36*, 10429–10437.

(22) Lebègue, E.; Anderson, C. M.; Dick, J. E.; Webb, L. J.; Bard, A. J. “Electrochemical Detection of Single Phospholipid Vesicle Collisions at a Pt Ultramicroelectrode.” *Langmuir*, **2015**, *31*, 11734–11739.

(23) Lebègue, E.; Barrière, F.; Bard, A. J. “Lipid Membrane Permeability of Synthetic Redox DMPC Liposomes Investigated by Single Electrochemical Collisions.” *Anal. Chem.*, **2020**, *92*, 2401–2408.

(24) Cheng, W. & Compton, R. G. “Investigation of single-drug-encapsulating liposomes using the nano-impact method.” *Angew. Chem. Int. Ed.*, **2014**, *53*, 13928–13930.

(25) Lovrić, J.; Najafinobar, N.; Dunevall, J.; Majdi, S.; Svir, I.; Oleinick, A.; Amatore, C.; Ewing, A. G. “On the mechanism of electrochemical vesicle cytometry: chromaffin cell vesicles and liposomes.” *Faraday Discussions*, **2016**, *193*, 65–79.

(26) Barlow, S. T. & Zhang, B. “Fast Detection of Single Liposomes Using a Combined Nanopore Microelectrode Sensor.” *Anal. Chem.*, **2020**, *92*, 11318–11324.

(27) Pan, R.; Hu, K.; Jiang, D.; Samuni, U.; Mirkin, M. V. “Electrochemical Resistive-Pulse Sensing.” *J. Am. Chem. Soc.*, **2020**, *141*, 19555–19559.

(28) Chabanon, M., Ho, J. C. S., Liedberg, B., Parikh, A. N., & Rangamani, P. “Pulsatile Lipid Vesicles under Osmotic Stress.” *Biophys. J.*, **2017**, *112*, 1682–1691.

(29) Li, X.; Majdi, S.; Dunevall, J.; Fathali, H.; Ewing, A. G. “Quantitative Measurements of Transmitters in Vesicles One at a Time in Single Cell Cytoplasm with Nano-tip Electrodes.” *Angew. Chem. Int. Ed.*, **2015**, *54*, 11978–11982.

(30) Dunevall, J.; Fathali, H.; Najafinobar, N.; Lovric, J.; Wigström, J.; Cans, A. S.; Ewing, A. G. “Characterizing the Catecholamine Content of Single Mammalian Vesicles by Collision-Adsorption Events at an Electrode.” *J. Am. Chem. Soc.*, **2015**, *137*, 4344–4346.

(31) Dunevall, J.; Majdi, S.; Larsson, A.; Ewing, A. G. “Vesicle impact electrochemical cytometry compared to amperometric exocytosis measurements.” *Curr. Opin. Electrochem.*, **2017**, *5*, 85–91.

(32) Li, X.; Ren, L.; Dunevall, J.; Ye, D.; White, H. S.; Edwards, M. A.; Ewing, A. G. “Nanopore Opening at Flat and Nanotip Conical Electrodes during Vesicle Impact Electrochemical Cytometry.” *ACS Nano*, **2018**, *12*, 3010–3019.

(33) Zhang, X. W.; Hatamie, A.; Ewing, A. G. “Simultaneous Quantification of Vesicle Size and Catecholamine Content by Resistive Pulses in Nanopores and Vesicle Impact Electrochemical Cytometry.” *J. Am. Chem. Soc.*, **2020**, *142*, 4093–4097.

(34) Bard, A. J.; Faulkner, L. R. *Electrochemical Methods: Fundamentals and Applications*; John Wiley & Sons, 2000.

(35) Hoffmann, E. K.; Lambert, I. H.; Pedersen, S. F. Physiology of cell volume regulation in vertebrates. *Physiol. Rev.*, **2009**, *89*, 193–277.

(36) Oleinick, A.; Lemaître, F.; Collignon, M. G.; Svir, I.; Amatore, C. “Vesicular release of neurotransmitters: Converting amperometric measurements into size, dynamics and energetics of initial fusion pores.” *Faraday Discussions*, **2013**, *164*, 33–55.

(37) Konopka, S. J.; McDuffie, B. “Diffusion Coefficients of Ferri- and Ferrocyanide Ions in Aqueous Media, Using Twin-Electrode Thin-Layer Electrochemistry.” *Anal. Chem.*, **1970**, *42*, 1741–1746.

(38) Oja, S. M.; Robinson, D. A.; Vitti, N. J.; Edwards, M. A.; Liu, Y.; White, H. S.; Zhang, B. “Observation of multipeak collision behavior during the electro-oxidation of single ag nanoparticles.” *J. Am. Chem. Soc.*, **2017**, *139*, 708–718.

(39) Bruns, D.; Riedel, D.; Klingauf, J.; Jahn, R. “Quantal release of serotonin.” *Neuron*, **2000**, *28*, 205–220.

(40) Scott, H. L.; Skinkle, A.; Kelley, E. G.; Waxham, M. N.; Levental, I.; Heberle, F. A. “On the Mechanism of Bilayer Separation by Extrusion, or Why Your LUVs Are Not Really Unilamellar.” *Biophys. J.*, **2019**, *117*, 1381–1386.

(41) Freudiger, C. W. et al. Label-free biomedical imaging with high sensitivity by stimulated Raman scattering microscopy. *Science* **2008**, *322*, 1857–1861.

(42) J. Tipping, W., Lee, M., Serrels, A., G. Brunton, V. & N. Hulme, A. Stimulated Raman scattering microscopy: an emerging tool for drug discovery. *Chemical Society Reviews* **2016**, *45*, 2075–2089.